ENHANCING EARTHQUAKE PERFORMANCE OF CIVIL STRUCTURES VIA STRUCTURAL CONTROL

A Thesis Submitted to
the Graduate School of
İzmir Institute of Technology
in Partial Fulfillment of the Requirements for the Degree of

DOCTOR OF PHILOSOPHY

in Civil Engineering

by
Vedat ŞENOL

October 2021
İZMİR

ACKNOWLEDGMENTS

First and foremost, I would like to express my innermost gratitude and send my special thanks to my supervisor, Dr. Gürsoy Turan, for his excellent supervision and for allowing me to study this multidisciplinary topic. He encouraged me to find out and study what intrigues me. Further, the guidance he provided throughout my dissertation made me continue even from a long distance. This thesis would not exist without his never-ending support. I will always remain grateful to him.

I would like to give my special thanks to my doctoral committee members: Dr. Engin Aktaş, Dr. Özgür Özçelik, who have always been willing to help during the critical periods of my research. I am thankful to Dr. Ali Bozer for contributing as my defense committee member. I wish thank to Dr. Enver Tatlıcıoğlu, who also heartened me to study control theory and its applications. Also, my sincere thanks go to all Civil Engineering faculty for their lecturing and supports.

I would like to thank Dr. Anders Helmerson for his support on the subject of robust multi-variable controllers and his kindness. I wish to express my warmest thanks to my thoughtful friend, Vortechz Andersson, who have made my time in Sweden more delightful with discussions on any real or fictitious problem one can think of and the contributions to the subjects of the systems and control.

I would like to acknowledge the support of Halil, Sinan, Amin, Oğulcan, Faruk, Nastran, Giovanni, Çağlayan, Hasan, Baturay, Egemen, Ema, Marcus, Kamil, Deniz Ş., Kenan, Deniz M. and many others throughout tough times. Without your supports and friendship, I can not even imagine how this journey could have been.

I want to thank my dear aunties: Leyla, Mukaddes, and Songül, who I always considered like my big sisters, and my lovely grandmother: Makbule, who is precious to me and all my family, for their support and love.

I am incredibly grateful to my parents, Nurcan and Şener, for their love, support, care, and patience in listening to my endless complains. I wish to express my sincere thanks to my ”sweet” twin: Sedat, my beloved younger brothers: Emircan and Erdoğan, who made me laugh all the tough times, and Özge’s family, that is my complementary family:İsmet, Hanife, and Özden.

Last but not least, I send my heartfelt thanks to my love, Özgecan, who is a life companion to me during this period; your unconditional love and support keep me moving. It is certain that I would not complete this study without you.

ABSTRACT

ENHANCING EARTHQUAKE PERFORMANCE OF CIVIL STRUCTURES VIA STRUCTURAL CONTROL

In this study, two different benchmark buildings (3 and 20-story) are employed to attenuate structural responses under seismic disturbances. As control devices, active (actuators), semi-active (Magneto-rheological dampers), passive (Tuned mass dampers and Friction Pendulum Bearings), and hybrid controllers are utilized.

The 3-story structure is modeled linearly and employed to apply to different control strategies. Some control algorithms: LQR, PDD-state-feedback, pole-placement, H_∞, H_2, are used with active and semi-active control devices. As passive devices, TMDs and FPBSs are utilized on the nominal-linear model. Thereafter, hybrid controllers are employed: one composed of a TMD and actuator/MRD and one composed of an FPBS and actuator/MRD.

A robust controller, μ-synthesis, is employed to control the same linear structure having uncertainties in mass, stiffness, and damping matrices within reasonable ranges.

A nonlinearly-modeled 20-story benchmark structure is employed to implement passive and hybrid control strategies. As passive devices, STMD and MTMD setups are employed. Further, a robust control algorithm is used through an actuator serially connected to the STMD. Subsequently, variations caused by nonlinearities are determined. These variations are regarded as uncertainties, and the μ-synthesis is utilized in the design of a robust controller on a truncated linear model. Then, the designed robust control is employed to control the 20-story benchmark structure modeled nonlinearly. The structural responses in both frequency and time domains are discussed. Matlab, Python, and OpenSees framework (Tcl/Tk) were employed to realize all linear and nonlinear simulations throughout the study.

ÖZET

YAPISAL KONTROL İLE İNŞAAT YAPILARININ DEPREM PERFORMANSININ ARTIRILMASI

Bu çalışmada, sismik yükler altında yapısal tepkileri hafifletmek için iki farklı tipte kıyaslama binası (3 ve 20 katlı) kullanılmıştır. Kontrol aygıtı olarak aktif (aktüatör), yarı aktif (manyeto-reolojik damper), pasif (ayarlanmış kütle sönümleyicisi ve sürtünmeli sarkaç yatağı) ve hibrit kontrolörler kullanılmaktadır.

Farklı kontrol stratejilerini uygulama amacıyla, 3 katlı yapı doğrusal modellenmiştir. Aktif ve yarı aktif kontrol cihazları kullanılırken, LQR, PDD durum geri bildirimli, kutup-yerleştirme, H_∞, H_2 kontrol algoritmaları uygulanmıştır. Pasif cihazlar olarak, nominal-doğrusal modelde TMD'ler ve FPBS'ler kullanılmıştır. Kullanılan kontrolörlere ek olarak, hibrit kontrolörler: Bir TMD + aktüatör/MRD'den oluşan, ve bir FPBS + aktüatör/MRD'den oluşan iki farklı model kullanılmıştır.

Makul aralıklar içinde kütle, rijitlik ve sönümleme matrislerinde belirsizliklere sahip aynı doğrusal yapının deprem performansını arttırmak için gürbüz bir kontrolör olan μ-sentez kullanılmıştır.

Tezin son kısmında, pasif ve hibrit kontrol stratejilerini uygulamak için doğrusal olmayan 20 katlı bir kıyaslama yapısı modellenmiştir. STMD ve MTMD pasif kontrölör konfigurasyonları kullanılmıştır. Ayrıca, STMD'ye seri olarak bağlanmış bir aktüatör aracılığıyla gürbüz bir kontrol algoritması kullanılır. Bunun için, doğrusal olmama durumlarının neden olduğu varyasyonlar kestirilmiş ve bu varyasyonlar belirsizlik aralığının tespitinde kullanılmıştır. Elde edilen belirsizlikleri içeren 20 katlı doğrusal yapı için denetleyici tasarımında bir $\mu-$ sentezinden faydalanılmıştır. Daha sonra, doğrusal olmayan şekilde modellenen 20 katlı kıyaslama yapısını kontrol etmek için tasarlanan gürbüz kontrolör kullanılır. Sonuç olarak, doğrusal olmayan temelli belirsizlikler için gürbüz bir kontrol elde edilir. Son olarak, hem frekans hem de zaman alanlarındaki yapısal tepkiler tartışılır. Çalışma boyunca, tüm doğrusal ve doğrusal olmayan simülasyonları gerçekleştirmek için Matlab, Python ve OpenSees (Tcl/Tk) kullanılmıştır.

TABLE OF CONTENTS

LIST OF FIGURES

Figure **Page**

Figure **Page**

Figure **Page**

LIST OF TABLES

Table **Page**

LIST OF ABBREVIATIONS

ARE : Algebraic Riccati Equation

ATMD : Actively Controlled Tuned Mass Damper

AWGN : Additive White Gaussian Noise

DOF : Degrees of Freedom

EQ : Earthquake

FFT : Fast Fourier Transform

FPBS : Friction Pendulum Bearing System

LFT : Linear Fractional Transformation

LQE : Linear Quadratic Estimator

LQG : Linear Quadratic Gaussian

LQR : Linear Quadratic Regulator

MRD : Magneto-Rheological Damper

MTMD : Multiple Tuned Mass Damper

PDD : Proportional Double Derivative State Feedback Control

PP : Pole-Placement Controller

STMD : Single Tuned Mass Damper

TMD : Tuned Mass Damper

VOD : Variable Orifice Damper

CHAPTER 1

INTRODUCTION

Construction has been an ongoing need since the existence of humanity. In the formation of these constructions, human needs and environmental conditions are the main factors. Human beings who want to raise their standards move to more complex and larger dimensions e.g., skyscrapers. Growing dimensions and complexity have led to higher costs (Burj Khalifa, 1,2 billion USD). As a result, constructions have been made more durable and sustainable. As the structures rose, wind loads and earthquake loads were statistically applied, and the cross-sections had been enlarged. Despite all considered precautions, there is no guarantee that constructions can be safe against possible failure mechanisms.

The concept of *structural control* for civil engineering was proposed by Yao (1972) to meet seismic disturbance-related demands. The structural control strategies can be classified into three major groups: passive, active, and semi-active control. In this aspect, many studies have been done on structural vibration attenuation. Structural control is a field that has been studied over the past 30 years and is constantly developing. The seminal studies in this area were conducted by Ahmadi (1995) for passive control, and Roffel and Narasimhan (2014) for active control. Thereafter, hybrid control strategies composing of two different control devices were put forward.

The notion of passive control origin can go more than 100 years back to an engineering professor John Milne in Japan. He installed ball bearings under a small house that he built. He aimed to exhibit that a building can be protected from seismic excitation. Many scholars in different configurations have widely used it.

Semi-active controllers can be considered as a class of active control systems. On the contrary of the active controllers i.e., actuators, the required external energy is smaller in magnitude. A semi-active control mechanism does not introduce power-driven energy to the structure. Hence bounded-input bounded-output (BIBO) stability is assured. These mechanisms are often regarded as controllable passive tools. In the literature, the primary work that proposed the so-called 'semi-active structural control' belongs to Kobori (1991). He indicated that an applied semi-active controller should diminish the kinetic energy in the employed structure.

It is noteworthy that these control strategies are compared by predefined performance indices to see which controller is more beneficial for the corresponding structure. The control of structures requires a fundamental structural model to start with. The mathematical model expressions, however, do not generally match the physical systems. These modeling differences can be classified as uncertainties and they should be taken into account. On the contrary, if controllers are modeled based on nominal models only, uncertainties may result in mal-performing controllers since the control systems work in a different frequency region than the planned one. For this reason, a robust control concept should be employed.

One problem related to the robust controller design may be the definition of the uncertainty ranges. For linearly modeled structures, these ranges can be estimated according to the model parameters reliability. For nonlinear structural behaviors, however, the decision on the uncertainty ranges is not straightforward. As an example, the stiffness of a yielding structural element may reduce to 10 percent of its initial value. Therefore, the nonlinear structural control design needs well-determined strategies to account for the uncertainty ranges.

1.1. Overview and the Organization of the Thesis

In the current dissertation, a method is employed to find proper control strategies for structures with increasing complexity: from a linear system to a nonlinear-uncertain system. This direct method is applied as summarized in the following lines.

In Chapter 2, the employed earthquake data, performance criteria to compare results, and the control devices are introduced. The comparison of these control devices is established by implementing performance indices as well as maximum response graphs.

In Chapter 3, an existing 3-story mock-up structure and an observer design are introduced. The structure's seismic performance is increased by active/semi-active and passive controllers. As active/semi-active controllers, an magneto-rheological damper (MRD) and an actuator are employed. For the passive controller strategies, a friction pendulum bearing system (FPBS) and a tuned mass damper (TMD) devices are utilized. Subsequently, five different control algorithms are employed: LQR, State-Space PDD, Pole Placement, H_2, and H_∞ controllers. The results are compared and discussed. Two different hybrid systems namely combinations of a base-isolation and an MRD/actuator (MRD/actuator+FPBS); and a TMD and MRD/actuator (MRD/actuator+TMD) were employed to benefit from both strategies' advantages. The installment of the base isolator

filters the lower frequencies of the earthquake excitation. Hence, the first mode of the superstructure is not excited. The superiority of the hybrid application of the two control systems is revealed. The effectiveness comparisons of both the control algorithms and the configurations are established by implementing performance indices.

In Chapter 4, the possible differences between a mathematical model and a real structure simulation results are investigated. This issue is a common problem that appears during the dynamic motion of the structure, which might be modeled as parametric variations in the stiffness, damping, and mass matrices. These variations in parameters need to be estimated, and the mathematical model needs to be updated to obtain higher robustness and control performances. In this part of the study, a linear fractional transformation (LFT) is employed for uncertainty modeling. Further, a general H_∞ control design of an MRD for vibration reduction in a building with mass, damping, and stiffness uncertainties is presented.

In Chapter 5, a robust control design scheme is proposed to mitigate nonlinear vibrations of a benchmark building. The method is presented in the following order: I. The effectiveness of single tuned mass damper (STMD), and distributed-multi-tuned mass dampers (MTMD), for a nonlinearly modeled benchmark structure is investigated by comparing their dynamic responses. II. A hybrid controller device, composed of a passive STMD and an active controller, is designed. In the control design procedure, both the nonlinear building model and the discrepancy among the mathematical model and the physical structural response is considered. As a novelty, differences between the linear and nonlinear benchmark building responses are regarded as uncertainties. Accordingly, these uncertainties are considered as perturbations existing in the linear 20-storey benchmark building, and μ-synthesis robust controller is designed depending on this linearly-modeled structure. Then, the designed robust controller is utilized on the nonlinearly-modeled structure to control during nonlinear simulations. This type of model setup becomes convenient, especially when changes in model parameters are expected during the structure's motion.

CHAPTER 2

PERFORMANCE COMPARISON SETUP AND CONTROL STRATEGIES

During this study, several controller algorithms are utilized via different types of control devices. The comparison of these control devices is established by implementing performance indices as well as maximum response graphs. Hence, in this chapter, the employed earthquake data, performance criteria to compare results, and the control devices are introduced.

2.1. Selected Earthquakes

To evaluate the employed structures' seismic performance, having a controller and without a controller, they are subjected to four real earthquakes: El Centro, Hachinohe, Kobe, and Northridge. The earthquake time records are given below in Fig. 2.1.

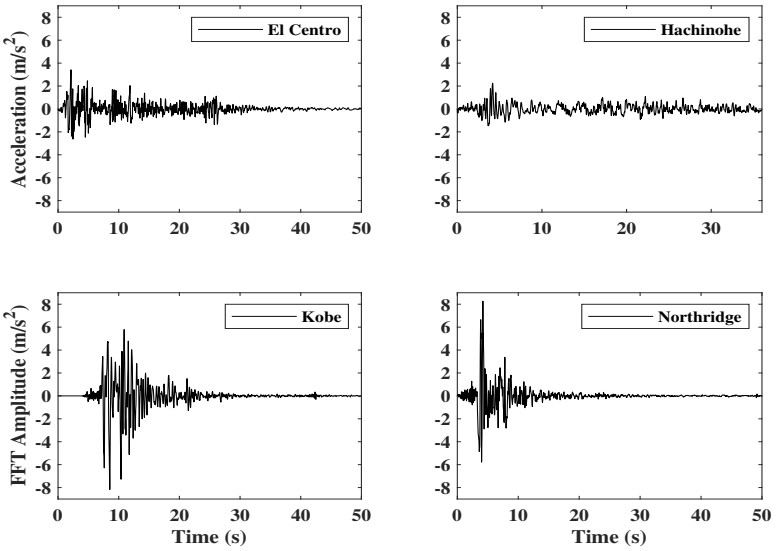

Figure 2.1. Earthquakes data applied on the benchmark model

The Fast Fourier Transform (FFT) on the earthquake records is utilized in Fig. 2.2 to see their frequency contents. Two different structures are employed under the scope of the current study. The small structure (3-storey) is subjected to only the El Centro EQ, and its first mode of natural frequency, 2 Hz, is depicted with the red line Fig. 2.2. All EQs are applied on the second structure (20-storey), and its first five modal frequencies are between 0.26 Hz and 2.40 Hz, depicted with black dotted lines. Here, it is seen that applied earthquake contents cover the first five modes dominating the total response of the second structure. In the literature, frequency comparisons are made via spectral displacement diagrams, where the structure is nominal. In this dissertation, however, nonlinearity issues are covered, and for this reason, the FFT responses are favored to spectral response figures.

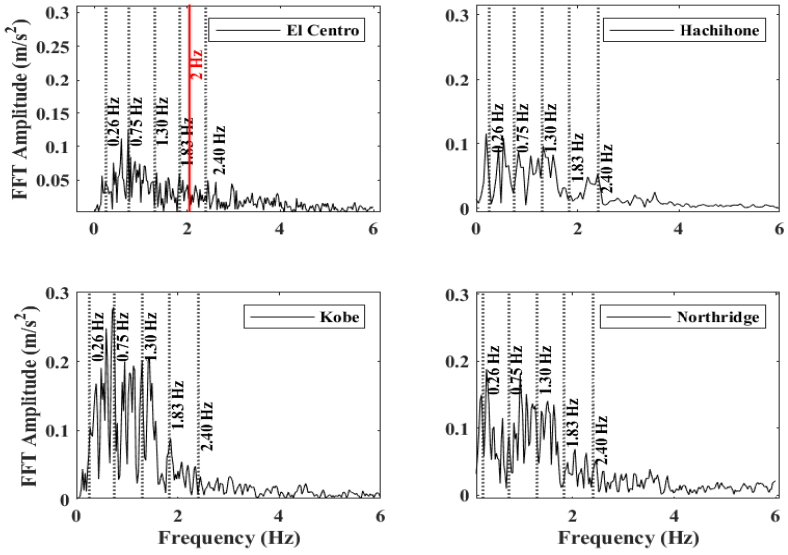

Figure 2.2. Frequency characteristics of the earthquakes data

2.2. Performance Criteria

In this section, non-dimensional performance criteria are outlined. The controlled structural responses are proportioned with respect to the uncontrolled structure responses. Therefore, the lower performance indices are desired, indicating a better control strategy. Eight performance indices are selected from the work of Christenson (2001) in which 16 performance indices were introduced. Indices which are larger than 1 imply that the applied control strategy worsens the structural responses.

The first comparison criterion is the normalized floor displacement relative to the ground which is defined as

$$J_1 = \max_{EQs} \left\{ \frac{\max_{\substack{t \\ i\in\eta}} |x_i(t)|}{x^{\max}} \right\}, \tag{2.1}$$

where $x_i(t)$ is the ith floor's displacement response, η is the set of DOFs which are of lateral directions, $x^{\max}$ is the maximum uncontrolled displacement, EQs is the set of earthquakes (El Centro, Hachinohe, Kobe, Northridge), and |.| indicates absolute value. The maximum drifts are normalized with respect to the corresponding earthquakes. The second criterion is, therefore, given as below

$$J_2 = \max_{EQs} \left\{ \frac{\max_{\substack{t \\ i\in\eta}} |\frac{d_i(t)}{h_i}|}{\max \left\{ |\frac{d_{ui}(t)}{h_i}| \right\}} \right\}, \tag{2.2}$$

herein d_i is the inter-story drift of the ith floor above the ground floor, h_i is the height of the associated floor, and $\max \left\{ |\frac{d_{ui}(t)}{h_i}| \right\}$ is the maximum uncontrolled inter-story drift ratio.

The next criterion is the acceleration ratio between the controlled and uncontrolled structures as follows

$$J_3 = \max_{EQs} \left\{ \frac{\max_{\substack{t \\ i\in\eta}} |\ddot{x}_{ai}(t)|}{\ddot{x}_a^{\max}} \right\}, \tag{2.3}$$

where the $|\ddot{x}_{ai}(t)|$ is the maximum absolute value of the controlled structures ith floor acceleration to the corresponding applied earthquake, and $\ddot{x}_a^{\max}$ is the maximum absolute value of the acceleration of the uncontrolled structure. The normalized and non-dimensionalized base shear force is given as the fourth comparison criterion as follows

$$J_4 = \max_{EQs} \left\{ \frac{\max_{t} |\sum_{i=1}^{n_s} m_i \ddot{x}_{a\eta i}(t)|}{F_b^{\max}} \right\}, \tag{2.4}$$

where m_i are the masses of the above-ground floors, $\ddot{x}_{a\eta i}(t)$ are the floor accelerations, n_s is the number of stories, and $F_b^{\max}$ is the maximum uncontrolled base shear for each employed earthquake.

To have better insight into the performance of the structure having a controller, the comparison of the maximum responses may not be enough. The amount of energy that enters the structure may also be detrimental criteria which have led to the formulation of the last four performance indices. These criteria are based on 2-norm (L_2) formulations.

The first criterion of the four of them is a normalized value of the maximum lateral displacement relative to the ground level which can be given as follows

$$J_5 = \max_{EQs} \left\{ \frac{\max_{i\in\eta} \|x_i(t)\|}{\|x^{\max}\|} \right\}, \tag{2.5}$$

herein $\|x_i(t)\| = \sqrt{\int_0^{t_f} x_i(t)^2 dt}$ where t_f is a time which is required to allow the response of the structure to dissipate to less than 0.1% of its maximum value, and $\|x^{\max}\|$ is the maximum uncontrolled displacement norm among the stories.

The sixth criterion is a normed measure of maximum drift ratios which follows as

$$J_6 = \max_{EQs} \left\{ \frac{\max_{\mathrm{t,i}} \|\frac{d_i(t)}{h_i}\|}{\|d_n{}^{\max}\|} \right\}, \tag{2.6}$$

where $d_n{}^{\max} = \max_{i\in\eta} \|\frac{d_{ui}(t)}{h_i}\|$ provides the maximum normed inter-story drift ratio of the uncontrolled structure.

The next criterion is a measure of the normed floor accelerations,

$$J_7 = \max_{EQs} \left\{ \frac{\max_{\mathrm{i}\in\eta} \|\ddot{X}_{ai}(t)\|}{\|\ddot{X}_a{}^{\max}\|} \right\}, \tag{2.7}$$

where $\|\ddot{X}_a{}^{\max}\|$ is the maximum normed absolute acceleration of the uncontrolled structure disturbed by the corresponding earthquake.

The last criterion is a normed base-shear measure.

$$J_8 = \max_{EQs} \left\{ \frac{\max \|\sum_{i=1}^{n_s} m_i \ddot{X}_{a\eta i}(t)\|}{\|F_b^{\max}\|} \right\} \tag{2.8}$$

All aforementioned indices will be used in the comparison of the structures with different control strategies.

2.3. Control Strategies and Devices

Structural control devices are utilized to reduce the structure's response, such as structural displacements and/or internal forces. These devices primarily aim to regulate the lateral motions of the structures caused by earthquakes and wind because internal forces are generally related to structural deformations. These devices can be categorized into four main groups; active, semi-active, passive, and hybrid controllers according to their operating mechanism.

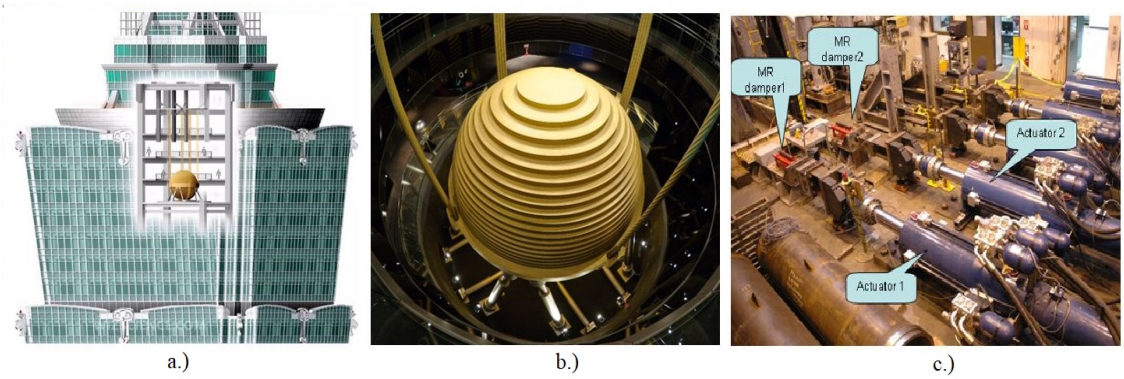

Figure 2.3. a-b) Taipei building's TMD, c) Active/semi-active devices (Source: Lehigh's Resource Center and civil.engg.world.blogspot.nl)

Fig. 2.3.c) shows actuators and MR dampers that can be utilized in structural control applications. The Taipei building is a good example of a passive control application. Here, a heavy hanging mass is utilized as a pendulum, which acts as a passive control device.

2.3.1. Passive Control Devices

Passive control devices aim to damp, redistribute or reduce the input energy that enters the structure through seismic motion. In general, passive controllers can be categorized into two main groups; seismic isolators and energy dissipation devices. A detailed comparison study, including a state-of-the-art study, was already done by Saaed et al. (2015).

2.3.1.1. Seismic Isolators

The main concept of the base isolation systems is to decouple the structure from the horizontal ground motion. The coupled system's first modal response is generally designed with a low frequency. As a result, the deformation of the first dynamic mode happens in the base isolation system while the structure above behaves typically as a rigid block. The deformation due to the higher modes occurs in the structure. These higher modes generally participate with low ratios in the total motion. As a result, the high energy transfer of the ground motion to the structure is limited. The base isolation system does not dissipate the energy, but it is stored as potential energy, which will be converted to kinetic energy. The role of dampers in parallel with base isolation systems is to absorb a part of this energy. Further, the presence of dampers is also vital to suppress resonance at the isolation frequency. Among the many base isolator sub-classes such as lead-rubber bearings, elastomeric bearings, combined elastomeric and sliding bearing, friction pendulum bearing systems (FPBS), the FPBS is chosen in the current dissertation.

- **FPBSs**

The FPBS has turned out a broadly accepted mechanism for new buildings and industrial facilities in seismic isolation. This device's superiority bases on the simplicity of the principles that form its behavior. In addition, the built-in self-centering action due to the concavity of the sliding surface increases its utility (Fig. 2.4). During a seismic action, the slider moves on the spherical surface lifting the structure. It dissipates the energy loaded by the seismic activity through friction between the rounded surface and the slider while moving. Commonly, the slider is placed on a vertical stud with a spherical hollowed end, enabling free rotation of the slider and ideal contact with the sliding surface at all times. To retain frictional forces relatively low, the friction coefficient, μ, is aimed at around 5-10 percent. A resistant teflon layer usually coats the slider that is preferably stainless steel. Most of the experimental and theoretical research grown so far with the FPBS has been settled on the small-deformation constitutive laws of the device (Zayas et al. (1989)). The large-deformation and the related $P - \Delta$ effects may become an issue in the isolator design since there are several recent earthquakes where large deformations were observed: Northridge (1994), Kobe (1995), and Taiwan (1999). As a result, the coupling between the lateral and vertical motions needs further evaluation because it is not

considered in the small-deformation theory and the current structural analysis software (Tsopelas et al. (2005)).

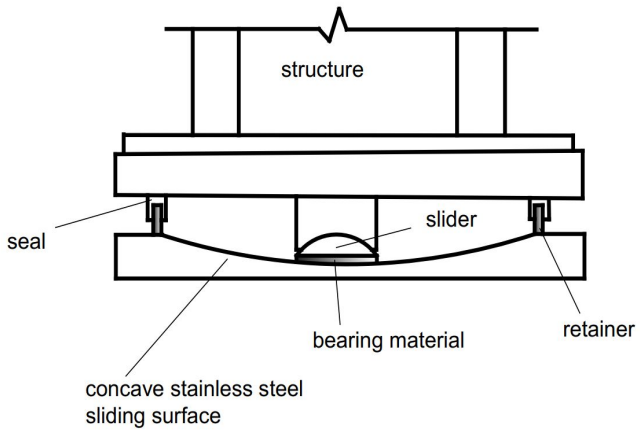

Figure 2.4. Friction Pendulum Bearing System (FPBS) 2-D Configuration
(Source: Almazán et al. (1998))

A study by Mokha et al. (1991) showed that their investigated isolated structure could sustain a larger excitation without yielding. For this purpose, the El Centro earthquake record was increasingly scaled until the uncontrolled and base-isolated structure started yielding. The latter scaling factor was found to be six times larger than the former.

2.3.1.2. Energy dissipation devices

The energy dissipation devices' primary role is to absorb or divert the input energy that enters the structure, loaded by seismic disturbances. On the contrary to the base isolators, these devices can be installed easily after the structures were built. Hence, they are preferable for structures already built and do not meet the lateral resistance requirements updated by newly developed regulations. There are many types of energy dissipation devices with respect to their energy damping mechanism: hysteretic devices, visco-elastic devices, re-centering devices (Spencer Jr and Nagarajaiah (2003)). In this study, tuned mass dampers (TMDs), a dynamic vibration absorber, are employed.

- **TMDs**

TMDs are passive control devices that are comparatively easy to mount in new buildings and in retrofitting the existing ones. They can be easily connected to the top-floor diaphragm, as seen in Fig. 2.5.

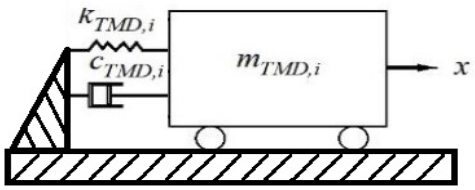

Figure 2.5. 2-D Configuration of TMD

An external power source is not needed by these devices to operate. Further, TMDs can be coupled with active and semi-active control devices to work as a hybrid system in which the TMD serves as a backup in the case of failure of the active device. The following considerations are notable:

1. For buildings with low damping ratios, TMDs with small mass ratios can reduce the response.

2. For buildings with high damping ratios, TMDs with large mass ratios decrease the response effectively.

Fig. 2.6 shows the effect of both the TMD installment and the damping ratio including the optimum(opt damping) of the TMD. Accordingly, the damping ratio optimization plays an essential role in the implementation of a TMD.

Pall et al. (1993) reported that the total cost (65 million dollars) of the Concordia University library building was decreased by 1.5 % due to the enforcement of the friction damper device (FDD). Notwithstanding, other researchers (Connor (2003); Lee et al. (2008); Tse et al. (2012) and Wang et al. (2015)) reported that TMD reduces the total cost by about 2% to 2.5%. In addition, TMD maintenance is relatively easier and cost-effective than other passive controllers such as friction pendulum systems (FPBS), passive base isolators. One maintenance check would be to identify the natural frequency

of the device. For TMDs, this check can be easily conducted, whereas, for the devices under the structures, this check may require a bigger effort. Therefore, many researchers: Sadek et al. (1997); Kareem and Kline (1995); Nagarajaiah and Sonmez (2007); Roffel and Narasimhan (2014); and Elias and Matsagar (2015), recommend the implementation of the TMD for the earthquake response control of the benchmark building.

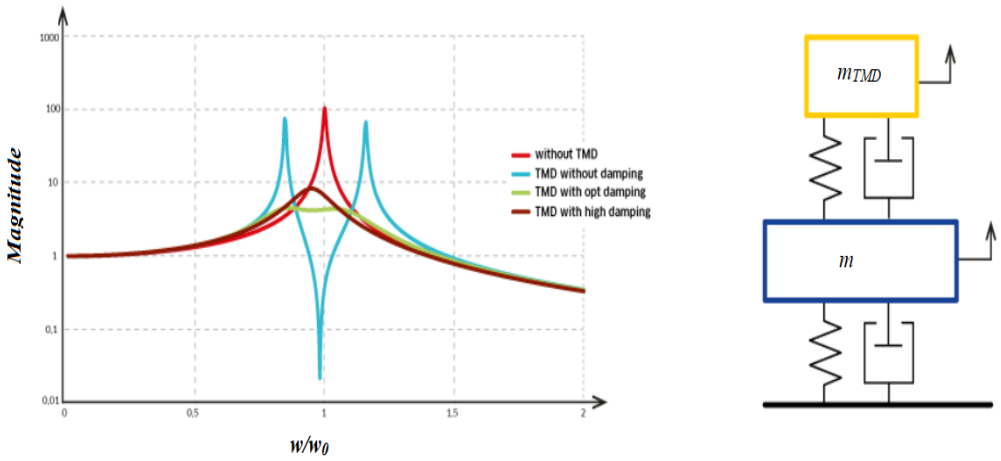

Figure 2.6. A Tuned Mass Damper (TMD) installed structures frequency responses (Source: www.esm-gmbh.de)

2.3.2. Active and Semi-active Control Devices

This part summarizes active actuators and semi-active control devices such as variable orifice dampers and magneto-rheological dampers.

2.3.2.1. Active Control Devices: Actuators

Actuators are devices producing the required forces via a power supply. They can apply forces with high-switching frequencies; thus, they are quick in response.

These devices are mainly used on small scales objects. It is relatively hard to come up with an actuator to stabilize a structure. In the current study, two different scale actuators are employed. The small one has the capacity of 5000 N while the large-scale actuators' capacity is 2000 KN with a 750mm stroke length shown in Fig. 2.7

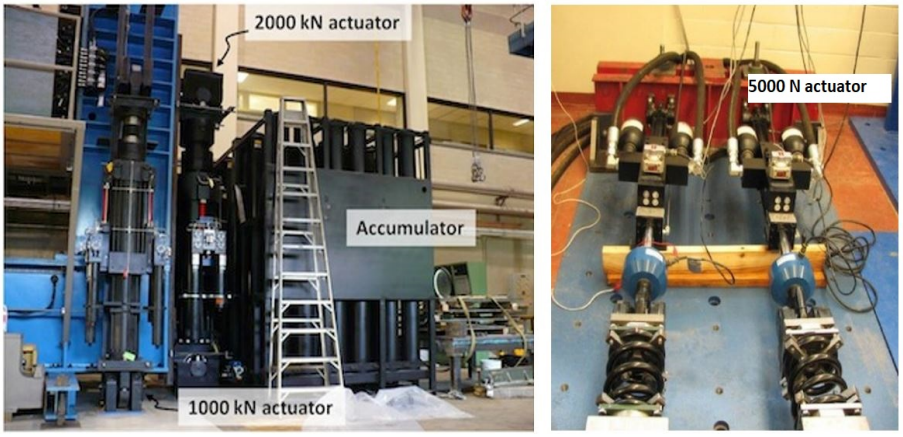

Figure 2.7. Structural testing facility - Department of Civil & Mineral Engineering (Source: *utoronto.ca*)

2.3.2.2. Semi-active Control Devices: VODs, MRDs

Figure 2.8. RD 1005-3 MRD (Produced by LORD Corp.) and the long-stroke MRD (Source: Zemp et al. (2016))

Semi-active control devices are considered by some researchers as extensions of passive devices. Such a device requires a small power supply such as batteries, which is essential during an earthquake. On the contrary, if the main power supply fails, an active-controlled structure may become unstable. For semi-active control applications, the damping value is adjustable. To this extent, it works as an actuator except for housing higher nonlinearity. Generally, the required control force happens to be in phase with the

relative velocity of the device. Therefore, they can be conveniently used in place of the active controllers. There are many different types of semi-active controller devices based on their working principles, such as variable orifice dampers (VODs), (Kınay (2013)), magneto-rheological dampers (MRDs). Two different scale MR dampers: one large-scale and one small-scale, are given below in Fig. 2.8, and the small one is employed in the current dissertation.

2.3.3. Hybrid Control Devices

The ”hybrid control” term commonly denotes a combined usage of active/semi-active and passive control systems. For instance, a structure installed with several distributed TMDs and MRDs can enhance the structure's seismic performance. There are many advantages in the utility of a hybrid controller, such as consuming less energy and dealing with a broader frequency bandwidth (Soong and Reinhorn (1993)). Besides, having such a controller can increase the structural system's robustness degree (Ali and Ramaswamy (2009)).

- **FPBS + Actuator/MRD**

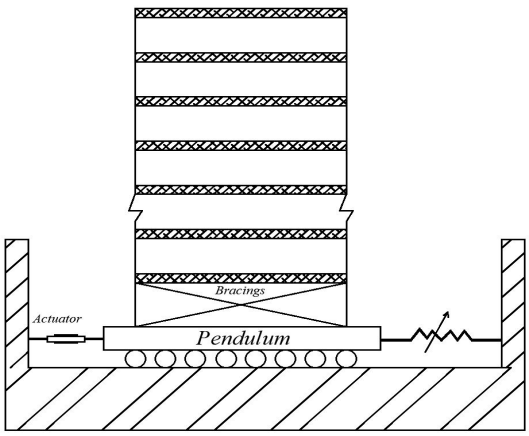

Figure 2.9. Hybrid control setup of Soong and Reinhorn

A hybrid controller setup consisting of a friction pendulum bearing system and an actuator was proposed by Soong and Reinhorn (1993). Their idea was that a base isola-

tor would not transfer a certain amount of earthquake energy to the structure, especially frequencies that are lower than the isolator's natural frequency.

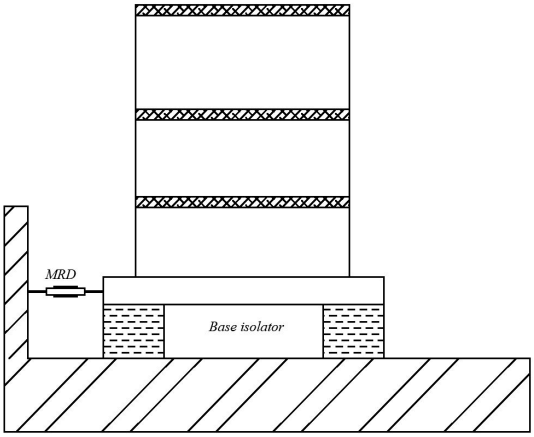

Figure 2.10. Hybrid control setup used by Ali and Ramaswamy

The isolator systems are designed not to let the lower frequencies pass to the upper structure. In addition, the actuator will minimize the rest of the disturbance energy by producing active forces. In 2009, Ali and Ramaswamy (2009) came up with a hybrid controller model that consists of an MR Damper and a passive base isolator. As seen in Fig. 2.10, the MR Damper is connected in parallel to the passive isolator.

- **TMD + Actuator/MRD**

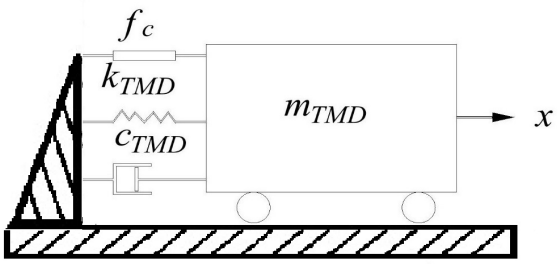

Figure 2.11. An active+passive hybrid controller setup

Many scholars have studied the advantages and efficiency of TMDs. It is known that TMDs are very sensitive to tuning frequency ratio, even if they are optimally de-

signed. A hybrid control strategy composed of the TMD and active/semi-active controller can overcome this handicap of the TMD. Fig. 2.11 shows the proposed hybrid control setup. The TMD can work as a passive damper in a specific frequency region, whereas the MRD can tune the TMD to its effective bandwidth.

CHAPTER 3

LINEAR SYSTEM CONTROLLERS

In this chapter, an employed mock-up structure and a designed observer are introduced. Thereafter, controller strategies to be applied are given in theory. The comparison of these control strategies is established by implementing performance indices. The experiences from this part of the study will be made use of in the implementation of larger size in chapter 4 and chapter 5.

3.1. Structural Model and Control Setup

There are two different structures employed during this study. The small one is a 3-story mock-up model and manufactured by Turan (2014) at the Izmir Institute of Technology Structural Lab.

Figure 3.1. The mock-up structure of Turan (2014)

The net floor height is 80 cm, and four high-strength steel columns, $100 \times 10mm$, provide the lateral stiffness. The floor beams were made of $90 \times 90 \times 4mm$ profiles. The

structural fundamental period is aimed at 0.5 seconds, which is reached by the adding steel plates to the floors. At the end, each floor is $200kg$ in mass.

The first three periods of the model building are 0.498, 0.177, and 0.122 seconds, respectively. Assuming no rotation at the node points, the bending stiffness of the first-story ply columns is calculated as follows,

$$\begin{aligned} k &= 4\left(\frac{12EI}{L^3}\right), \\ &= 156250N/m, \end{aligned} \tag{3.1}$$

where E is the modulus of elasticity ($E = 2e11N/m^2$), I is the moment of inertia of the column in the direction of motion ($I = 8.33e-9m^4$), and L is the clear span distance of the column ($L = 0.80m$). Since each story has four columns, the column rigidity is multiplied by four. Eq. 3.2 is used to calculate the shear force between the simulator and the building.

$$V_b(t) = k_{st}y_1(t), \tag{3.2}$$

where $V_b(t)$ is the base shear force in the excitation direction, and $y_1(t)$ is the displacement of first story. The stiffness, K_s, damping, C_s, and mass, M_s, matrices of the 3-story building model are shown below.

$$K_s = \begin{bmatrix} 2k & -k & 0 \\ -k & 2k & -k \\ 0 & -k & k \end{bmatrix}, \qquad C_s = \begin{bmatrix} 2c & -c & 0 \\ -c & 2c & -c \\ 0 & -c & c \end{bmatrix}, \qquad M_s = \begin{bmatrix} m & 0 & 0 \\ 0 & m & 0 \\ 0 & 0 & m \end{bmatrix}. \tag{3.3}$$

$$k = k_{st} = 156250N/m, \qquad c = 42.25Ns/m, \qquad m = 200kg.$$

The beam stiffness is much larger than the column stiffness and therefore, the degrees of freedom of rotation are reduced by using the static condensation method. As a result, a three degree of freedom (DOF) system model emerged. n_s, the number of DOFs, numerical analyzes were made at the initial stages of the project, the damping ratio corresponding to the first two modes of construction is assumed to be 2% and accordingly the damping matrix is evaluated as Rayleigh damping.

3.1.1. Mathematical Representation of the Structural Model

The structural system is modeled according to known geometry, material properties, and boundary conditions. This model will constitute the nominal model of the structure.

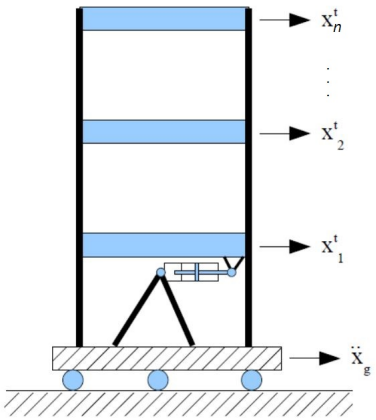

Figure 3.2. Shear building model with n_s floors

A sketch for the mock-up structure with a control device at the first story is illustrated in Fig. 3.2. The equation of motion for the given configuration can be formulated as

$$K_s x(t) + C_s \dot{x}(t) + M_s \ddot{x}(t) = \Gamma_u f_c(t) - M_s \Gamma_d \ddot{x}_g(t), \tag{3.4}$$

where $x(t)$ is the 3×1 displacement vector of the structure relative to the ground, $\Gamma_d = [1\ 1\ 1]^T$, $\ddot{x}_g(t)$ is the ground acceleration, $f_c(t)$ is the control force applied to the structure, and $\Gamma_u = [1\ 0\ 0]^T$ is the 3×1 control input location vector.

$$\begin{aligned} \dot{q} &= Aq + B_1 w + B_2 u \\ y_n &= Cq + D_1 w + D_2 u + n. \end{aligned} \tag{3.5}$$

Eq. 3.4 is transformed into state-space representation, with $q = \begin{bmatrix} x \\ \dot{x} \end{bmatrix}$ being the state vector. Further, measurements of the structural system, y_n, is modeled by using the system states and exogenous input: noise (AWGN), n, disturbance and control input.

A is the system matrix that holds relation between the states and the derivation of the states. By means of matrix A, the second-order linear differential equation (Eq. 3.4) is transformed into a first-order differential equation (Eq. 3.5). As a result, 3 unknowns in the Eq. 3.4 are transformed into 6 unknowns in the Eq. 3.5.

$$A = \begin{bmatrix} 0_{3\times3} & I_{3\times3} \\ -M_s^{-1}K_s & -M_s^{-1}C_s \end{bmatrix} \tag{3.6}$$

B_1 and B_2 are disturbance and control input weighting vectors, respectively.

$$B_1 = \begin{bmatrix} 0_{3\times1} \\ -\Gamma_d \end{bmatrix}, \qquad B_2 = \begin{bmatrix} 0_{3\times1} \\ M_s^{-1}\Gamma_u \end{bmatrix} \tag{3.7}$$

The C, D_1 and D_2 are weighting matrices which are formed based on the desired output variable, y. In this case, the outputs are inter-story drifts. As a result, these matrices will be formed as follows,

$$C = \begin{bmatrix} 1 & 0 & 0 & 0 & 0 & 0 \\ -1 & 1 & 0 & 0 & 0 & 0 \\ 0 & -1 & 1 & 0 & 0 & 0 \end{bmatrix} \tag{3.8}$$

$$D_1 = \begin{bmatrix} 0 \\ 0 \\ 0 \end{bmatrix}, \qquad D_2 = \begin{bmatrix} 0 \\ 0 \\ 0 \end{bmatrix}. \tag{3.9}$$

The matrix D_1 weights the disturbance, w, in our case $\ddot{x}_g(t)$. Similarly, D_2 indicates the weight of the control input to the measurements. The structural system is formed as both controllable and observable.

3.1.2. Observer Design

In controlling the systems, the state knowledge is needed for some controller designs. Further, measured responses generally include noise which may have detrimental effects on the control force output. As a remedy, observers can be used to predict the states of the system and outputs with filtering noise. If the observer estimates all state vectors, q, it is called a full-order observer.

The fundamental design principle for an observer is the measure of the closeness of the observed responses to the simulated responses. Another design criterion is how fast its modes are compared to the modes of the original system. In the literature, it is suggested that an observer's modes should be faster than those of the system (Kınay (2013)). Extremely fast observer modes are not acceptable because of stability constraints.

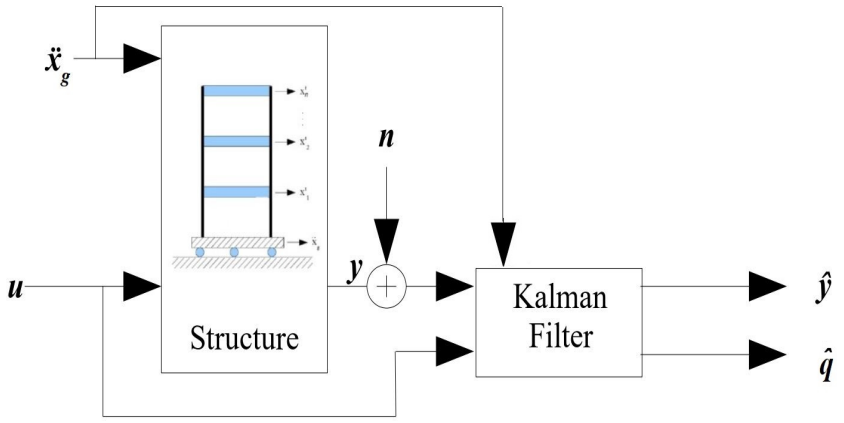

Figure 3.3. Kalman filter assembly

Fig. 3.3 depicts how Kalman filter is utilized in the current simulation method. The simulation commences with the entrance of the inputs to the structure. At that moment, potentiometers-based sensors gauge the current displacements. The noise-added measurements and the current input signals: the earthquake excitation and the control

force, are the inputs to the Kalman filter. Subsequently, the system states are acquired to calculate the required control force.

In order to estimate structure story velocities, the conventional Kalman Observer (Kalman (1960); Franklin et al. (1998); Lewis (1986); Deshpande (2017)) algorithm is used to develop the desired estimator. Given the continuous structure model in Fig. 3.3, the state-space equations are the same with the Eq. 3.5.

Additionally, with known inputs: the control force u, and the earthquake disturbance w, and the measurement noise n, expected values are given as follows

$$\begin{aligned} \mathrm{E}(w) = E(n) &= 0, \\ \mathrm{E}(ww^T) &= Q, \\ \mathrm{E}(nn^T) &= R, \\ \mathrm{E}(wn^T) &= N, \end{aligned} \tag{3.10}$$

where n stands for additive white Gaussian measurement noise ($AWGN$), and E() is the expected value of the corresponding variable. Apart from these, all estimates have a mean error of zero.

Meanwhile, a state estimate $\hat{q}$ that minimizes the steady-state error covariance is constructed:

$$P = \lim_{t \to \infty} E\left\{(\hat{q} - q)(\hat{q} - q)^T\right\}, \tag{3.11}$$

where t denotes the time. Consequently, the optimal solution is the Kalman filter with differential equations:

$$\dot{\hat{q}} = A\hat{q} + B_1 w + B_2 u + L(y_n - C\hat{q} - D_2 u), \tag{3.12}$$

where L is the observer gain determined by the Algebraic Riccati Equation (ARE) as follows:

$$L = (PC^T + \bar{N}) + R^{-1}, \tag{3.13}$$

where

$$\bar{R} = R + D_1 N + N^T D_1^T + D_1 Q D_1^T,$$
$$\bar{N} = B_1(QD_1^T + N), \tag{3.14}$$

and P solves the corresponding ARE.

At last, the Kalman observer/estimator uses the known inputs u, w and the measurements y to generate the output and state estimates $\hat{y}$ and $\hat{q}$. It is noteworthy that $\hat{y}$ estimates the true plant output given as follows,

$$\hat{y} = C\hat{q} + D_1 w + D_2 u. \tag{3.15}$$

It is necessary to underline that the current study simulations are carried out in the discrete-time domain. Thus, all the governed equations should be converted from the continuous-time to the discrete-time with a Δt time-step. By using the Euler method, the states can be evaluated as follows:

$$q[t_{i+1}] = q[t_i] + \Delta t\,(Aq[t_i] + B_1 w[t_i] + B_2 u[t_i]),$$
$$y_n[t_i] = Cq[t_i] + D_1 w[t_i] + D_2 u[t_i] + n[t_i], \tag{3.16}$$

along with the noise covariance data,

$$\mathrm{E}(w) = E(n[t_i]) = 0,$$
$$\mathrm{E}(w[t_i]w[t_i]^T) = Q,$$
$$\mathrm{E}(n[t_i]n[t_i]^T) = R,$$
$$\mathrm{E}(w[t_i]n[t_i]^T) = N. \tag{3.17}$$

The solution for the Kalman observer can be represented as follows (The Euler method):

$$\hat{q}[t_i|t_{i-1}] = \hat{q}[t_{i-1}] + \Delta t\, \hat{q}[t_{i-1}]. \tag{3.18}$$

The estimator/observer brings about the current output estimates $\hat{y}[t_i|t_i]$ and state estimates $\hat{q}[t_i|t_i]$ employing all accessible measurements extending to $y[t_i]$. The notation of $\hat{q}[t_i|t_i]$ denotes that the estimate (or prediction) of $\hat{q}[t_i]$ is made using measurements available at time t_i. The output equation is given as:

$$\begin{bmatrix} \hat{y}[t_i|t_i] \\ \hat{q}[t_i|t_i] \end{bmatrix} = \begin{bmatrix} (I - M_y)C \\ I - M_qC \end{bmatrix} \hat{q}[t_i|t_{i-1}] + \begin{bmatrix} (I - M_y)D & M_y \\ I - M_qD & M_q \end{bmatrix} \begin{bmatrix} u[t_i] \\ y_n[t_i] \end{bmatrix}, \tag{3.19}$$

where M_q and M_y, the innovation gains (Deshpande (2017)), are defined as:

$$\begin{aligned} M_q &= PC^T(CPC^T + \bar{R})^{-1} \\ M_y &= (CPC^T + D_1QD_1^T + D_1N)(CPC^T + \bar{R})^{-1}. \end{aligned} \tag{3.20}$$

Employing the new measurement $y[t_i]$, M_q updates the prediction of $\hat{q}[t_i|t_{i-1}]$ as follows:

$$\hat{q}[t_i|t_i] = \hat{q}[t_i|t_{i-1}] + M_q(y_n[t_i] - C\hat{q}[t_i|t_{i-1}] - D_1u[t_i]). \tag{3.21}$$

Fig. 3.4 illustrates a setup with inputs and outputs that we employed in the formulation of the Kalman filter. The structural true output is denoted by y, y_n corresponds to the sensor output of the measurement with noise, and $\hat{y}$ is the estimated output.

The Kalman filter is based on an optimization whose performance can be regulated by adjusting the scales between the input and output. The adjusting matrix, Q, is chosen as equally weighted among the input variables. The relative scale between input and output, N, signals is decided by the magnitude of these weighting matrices.

$$Q = 1e1 \begin{bmatrix} 1 & 0 & 0 \\ 0 & 1 & 0 \\ 0 & 0 & 1 \end{bmatrix}, \qquad R = 1e5, \qquad N = \begin{bmatrix} 0 & 0 & 0 & 0 & 0 & 0 \\ 0 & 0 & 0 & 0 & 0 & 0 \\ 0 & 0 & 0 & 0 & 0 & 0 \end{bmatrix}. \tag{3.22}$$

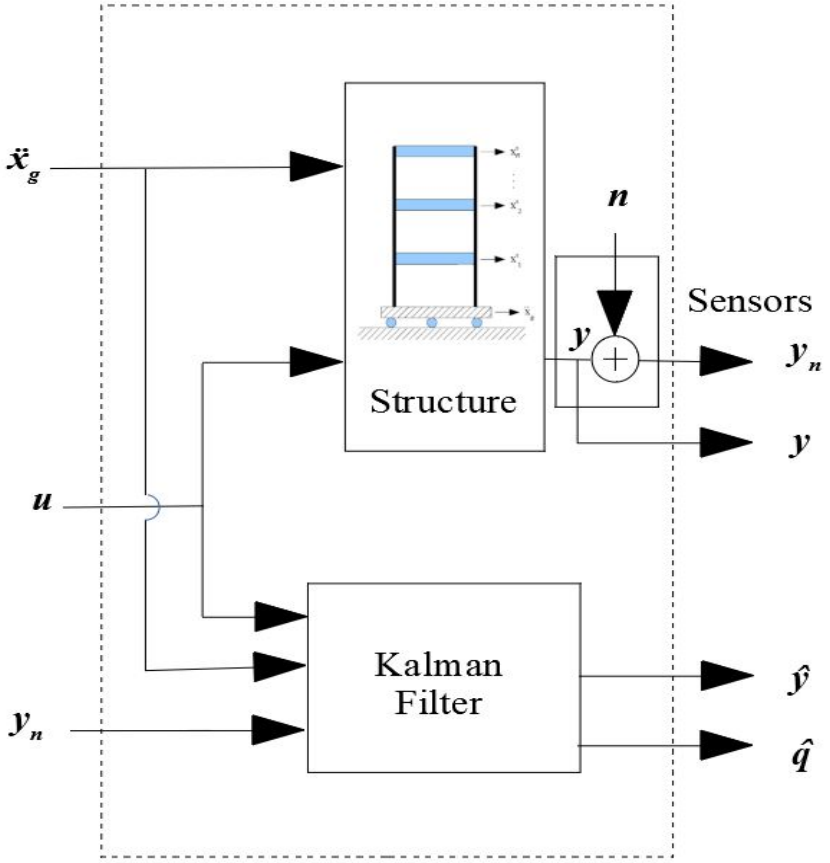

Figure 3.4. Kalman estimator- Structure parallel assembly

The simulations were carried out in discrete-time, and the time increment (Δt) was taken as 0.02 sec. In addition, white noise was added to the simulated displacement responses as sensor noise with a magnitude of 5% of their maximum displacement. Thus, the observer gain matrix, L, and the innovation matrix, M_q are obtained as follows:

$$L = \begin{bmatrix} -0.217 & 0.091 & 0 \\ -0.122 & -0.213 & 0.091 \\ -0.121 & -0.121 & -0.213 \\ -781.19 & 781.20 & 0.0093 \\ 0.0138 & -781.18 & 781.20 \\ 0.0213 & 0.0118 & -781.20 \end{bmatrix}, \quad M_q = \begin{bmatrix} 1 & 0 & 0 \\ 1 & 1 & 0 \\ 1 & 1 & 1 \\ -0.217 & 0.091 & 0 \\ -0.122 & -0.213 & 0.091 \\ -0.121 & -0.121 & -0.213 \end{bmatrix}. \quad (3.23)$$

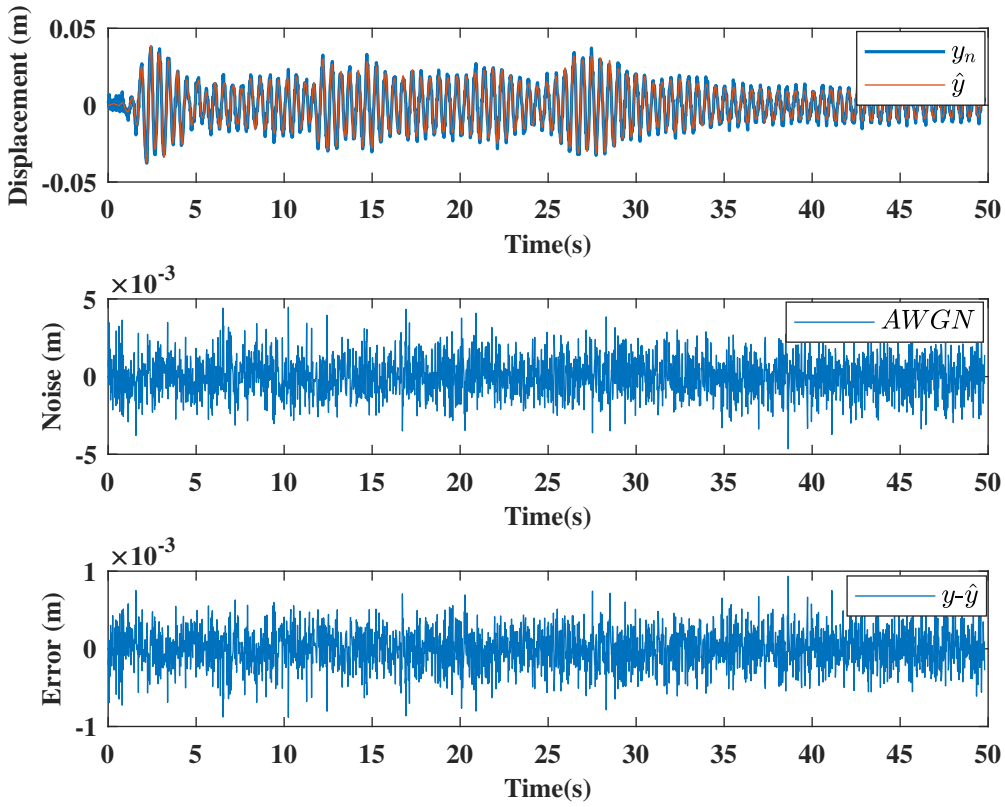

Figure 3.5. The performance of the designed Kalman estimator

Fig. 3.5 shows the estimator performance where both the estimated output and measured output are given for the first-floor displacement. The error, differences between measured and estimated outputs, is also illustrated, and it is around 1 percent and smaller than the assumed noise, which is 5 percent. In other words, the error difference is diminished by 80 percent, which makes the Kalman observer satisfactory.

3.2. Active and Semi-active Controllers

In this section, the employed active and semi-active controller algorithms will be introduced. These algorithms are applied to the structure through an actuator and an MRD. Thereafter, the introduced controller performances will be given for comparison.

Herein, it is beneficial to present the control algorithm-setup and the MRD dynamics so as to have a brief perception about how the simulations are undertaken.

3.2.1. MRD Dynamics

In the literature, the primary work that proposed the so-called 'semi-active structural control' belongs to Kobori (1991). He indicated that an applied semi-active controller should diminish the driven energy in a structure. As a semi-active control device, an electrohydraulic damper was employed.

Jolly Mark R. and Munoz (1996) modeled MRDs for the first time considering nonlinear effects. This model adds magnetic nonlinearity and saturation by creating a mechanism that distributes the magnetic flux density in the composite material. Experimental data about the viscoelastic behavior and magnetic properties of magnetic hydraulic fluids that model development hypotheses are reasonable. The model was shown as quasi-empirical because it has to conform to the experimental findings by specifying a parameter that identifies unmodified magnetic interactions.

Pan et al. (2000) provided a comprehensive analytical recommendation for an MRD. Jansen and Dyke (2000) used various control algorithms on MRDs. Semi-active control studies are conducted and compared, including the Lyapunov controller (Zinober (1994)), decentralized bang-bang controller, and modulated homogeneous friction algorithm. Ribakov and Reinhorn (2003) used MRD as a control device in the aspect of optimization. An LQR control algorithm was performed on MRDs placed in diagonal directions in a 7-story structure model. Wang and Dyke (2006) compared base isolators: smart dampers and LQG-controlled MRDs in benchmark studies. Yang Jr and BF (2002) proposed the modified Bouc-Wen hysteresis model. This model can estimate the damper response better in the region where the velocity and acceleration are opposite to the sign of planes and the magnitudes are small. The MRD control force is modeled according to the modified Bouc-Wen model. The Bouc-Wen model consists of springs, dash-pots and evolutionary variables to produce MRD behavior.

The MRD force is calculated by using the equilibrium equation for the MRD model in Fig. 3.6 as

$$f_{MRD}(t) = c_1\dot{y}(t) + k_1(x(t) - x_0). \tag{3.24}$$

If this force is written for the upper part of the Modified Bouc-Wen model,

$$f_{MRD} = \alpha z_{MRD} + c_0(\dot{x} - \dot{y}) + k_0(x - y) + k_1(x - x_0), \tag{3.25}$$

Then, the internal parameter, $\dot{y}$, can be obtained as follows,

$$\dot{y} = \frac{1}{c_0 + c_1}[\alpha z + c_0\dot{x} + k_0(x - y)]. \tag{3.26}$$

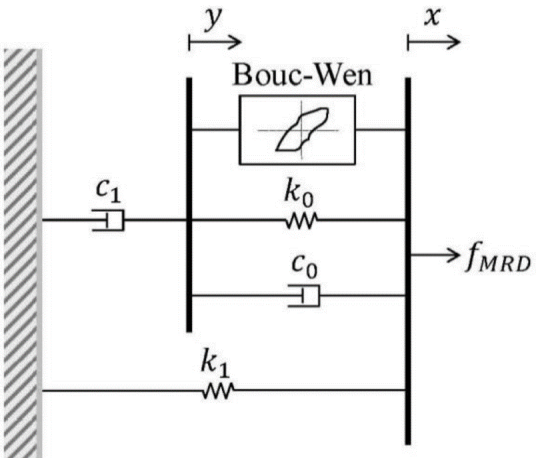

Figure 3.6. The modified Bouc-Wen model

The evolutionary variable of the Bouc-Wen model, z_{MRD}, is governed by

$$\dot{z_{MRD}} = \gamma|\dot{x} - \dot{y}||z_{MRD}|^{p-1} - \beta(\dot{x} - \dot{y})|z_{MRD}|^{p} + A_{MRD}(\dot{x} - \dot{y}), \tag{3.27}$$

where k_1 is the stiffness of accumulator within the damper casing, x_0 is the initial displacement of the piston. There are two damper models for low and high speeds, which are represented as c_0 and c_1, respectively. The shaping parameter of the hysteresis is represented with p. The linearity characteristics of the hysteresis are adjusted by A_{MRD}, γ and β.

$$\begin{aligned} \alpha(V_a) &= \alpha_a + \alpha_b V_a, \\ c_0(V_a) &= c_0 a + c_0 b V_a, \\ c_1(V_a) &= c_1 a + c_1 b V_a. \end{aligned} \tag{3.28}$$

where V_a is the armature voltage that cannot be measured. For this reason, the MR fluid dynamics reaching equilibrium are modeled by a first order low-pass filter presented by

$$\dot{V}_a = -\nu_{MRD}(V_a - v), \tag{3.29}$$

where v is the input voltage, and ν_{MRD} is the cut-off frequency. As an MRD, the $RD-1005$, produced by Lord Co., is employed. The mechanical model parameters for the employed MRD were given in Table. 3.1.

Table 3.1. Parameters for the modified Bouc-Wen model
(Source: Spencer Jr et al. (1997))

Parameter	**Value**	**Parameter**	**Value**
c_{0a}	2100 Ns/m	α_a	140000 N/m
c_{0b}	350 Ns/mV	α_b	69500 NV/m
c_{1a}	28300 Ns/m	γ	3630000 m^{-2}
c_{1b}	295 Ns/mV	β	3630000 m^{-2}
k_0	4690 N/m	A_{MRD}	301
k_1	500 N/m	p	2
x_0	0.143 m	ν_{MRD}	190 Hz

Numerical results of this individual MRD excited by sinusoidal displacement are presented for 1 Hz excitation frequencies and $1cm$ displacement amplitude in Fig. 3.7. The excitation magnitude is constant, and four different constant voltage levels are applied ($0V$, $1V$, $2V$, and $3V$).

According to the MRD force-displacement relationship in Fig. 3.7, the damper force increases proportionally to the increasing applied voltage. The zero voltage application results in a damper force based on the explicit damper characteristics, such as friction force caused by the moving piston. The relation between velocity and the MRD force is linear after a certain velocity limit.

During the simulation, the time step increment value is a critical issue for the MRD response calculations. Larger time steps cause wrong results, while smaller ones result in extreme calculation time. Spencer Jr et al. (1997) showed that the MRD responses were similar to the experimental ones when the simulations were run with a maximum time increment of 10^{-4} seconds. Accordingly, time step values smaller than this value give responses similar to the experimental ones, yet they unnecessarily increase the computational time. If the time step had been chosen larger than 10^{-4} seconds, the responses became unstable due to numerical issues. It is noteworthy that the time step for structural simulations may be larger than the MRD time step. In such a case, the MRD needs to be simulated in a loop to reach the time step of the structure.

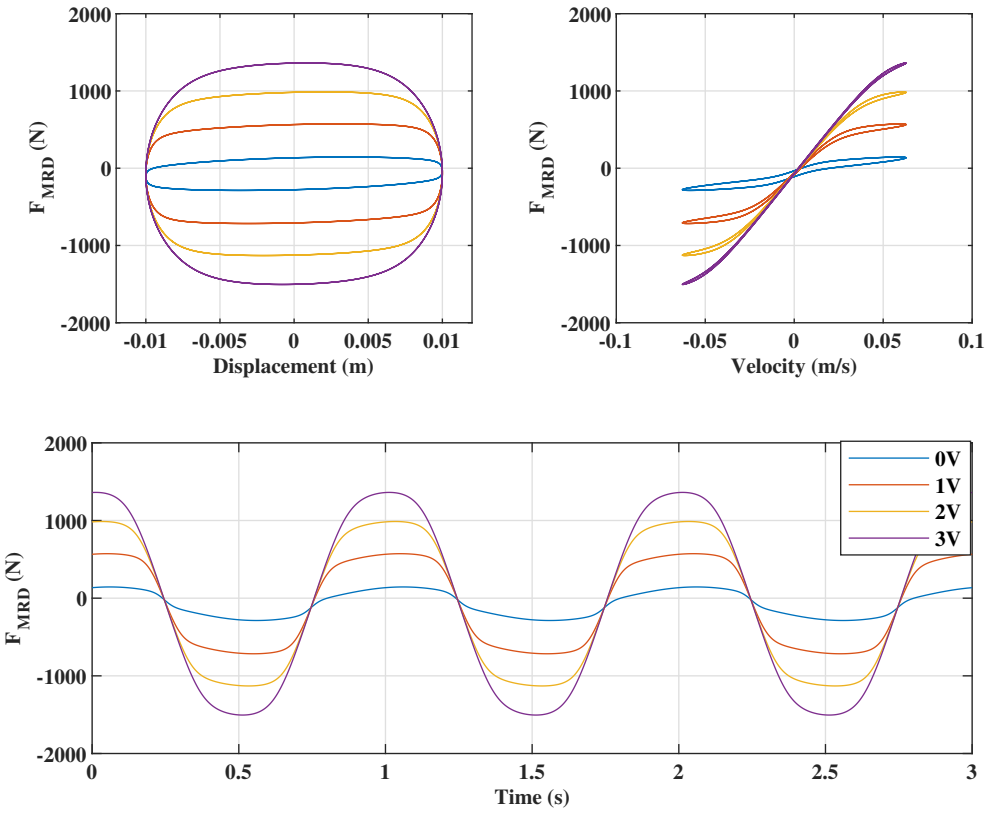

Figure 3.7. MRD responses under 1 Hz excitation

The applied voltage of $3V$ acquires the maximum absolute values of the MRD force. Hence, it was chosen as the maximum voltage level in this chapter of the study. Besides, the MRD will be limited by $3000N$ to keep the system working during further simulations.

3.2.2. MRD Control Algorithm Setup

Different control strategies can be utilized to find the control forces required for enhanced structural behavior. In optimal control algorithms, control signals that make the system satisfy some physical constraints and simultaneously maximize or minimize a chosen cost function are achieved. The controller consists of two stages in the present study: a linear optimal control and a modified clipped algorithm part. The optimal controller calculates the required control force u. Subsequently, the modified clipped algorithm determines the voltage to be applied by comparing the required control force u and the damper force at the previous time step. The block diagram representation of the system is presented in Fig. 3.8.

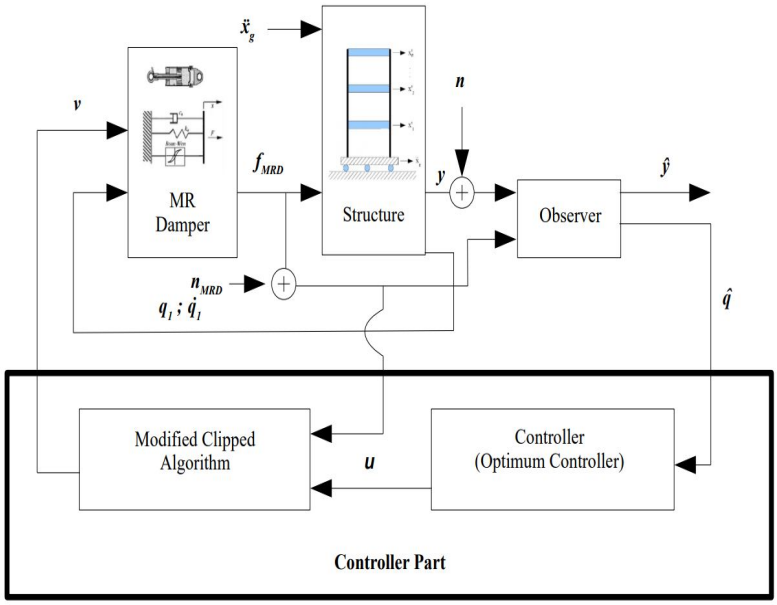

Figure 3.8. MRD setup

The damper's magnetic field is set to produce damping forces equal to those obtained by the optimal active control. The modified clipped control algorithm performs this part and determines the feedback block's output. Accordingly, the MRD generates the required control. If the MRD force is smaller than the required control force and has the same sign, a voltage level computed by interpolation is sent to the MRD.

The modified clipped control algorithm is graphically presented in Fig. 3.9.

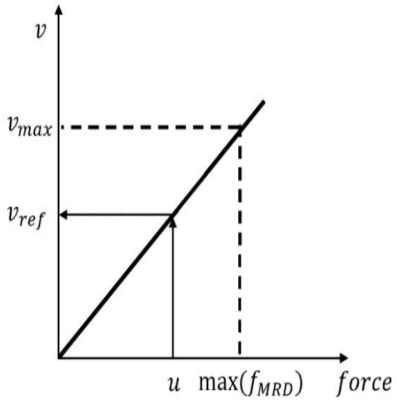

Figure 3.9. Graphical representation of modified clipped control algorithm
(Source: Dyke et al. (1996))

The required voltage level, v, is calculated according to the given equation below,

$$v = v_{ref} H\{(u - f_{MRD});\ \ f_{MRD}\}, \tag{3.30}$$

where v_{ref} is the reference voltage, and $H\{\}$ is the Heaviside step function. The modified clipped algorithm is stated as follows

$$v_{ref} = \begin{Bmatrix} \frac{u}{max(f_{MRD}))} v_{max} & for \quad |u| \leq max(f_{MRD})) \\ v_{max} & for \quad |u| > max(f_{MRD})) \end{Bmatrix}, \tag{3.31}$$

where u is the desired control force, and $max(f_{MRD})$ is the maximum force capacity of the MRD. The simulation of the system is undertaken in hybrid manner. It starts with the MRD control force calculation. This calculated MRD force, the noise and the earthquake excitation are the exogenous inputs to the structure. Accordingly, a linear simulation (lsim) is performed to acquire the structural outputs. These outputs including the noise and the inputs enter the Kalman filter to estimate the current states. Through these states, the required active control force is computed, and it is filtered by a saturation function. Herein, it gets limited for safety concerns so that the actual MRD force is below the maximum limit. This hybrid simulation is designed in the following pseudo-code Algorithm.1.

Algorithm 1 Control Application Algorithm

loop:
MRD current force:
$F_{mrd}(i) = -MR\ Damper\ function(dt, x_1(i-1), \dot{x}_1(i-1), V(i-1))$
Control & EQ input:
$W_{fmrd} = [F_{mrd}((i-1):i), w((i-1):i)]$
Controlled System Inter-story Drifts:
$[y(i-1:i,:),\ , q(i-1:i,:)] = lsim(P_{strct}, W_{fmrd}, t, x(i-1,:))$
Kalman Filter:
$y_n(i-1:i,:) = y(i-1:i,:) + n(i-1:i,:)\ Noisy \quad measurements$
$W_{kalm} = [F_{mrd}((i-1):i),\ \ddot{x}_g((i-1):i),\ y_v((i-1):i)]$
$[y_k(i-1:i,:),\ q_k(i-1:i,:)] = lsim(P_{kalmn},\ W_{kalm},\ t,\ q_k(i-1,:))$
Observer outputs given to the controller:
$F_{Act}(i) = -K_c * q_k(i,:)'$
If $F_{Act}(i) >= F_{max}$
$F_{Act} = F_{max}$
If $F_{Act}(i) <= -F_{max}$
$F_{Act}(i) = -F_{max}$
MRD Required Voltage:
$V(i) = MRDVoltage(F_{mrd}(i),\ F_{Act},\ V_{max})$
goto *top*.

3.2.3. Linear Quadratic Regulator (LQR)

It is necessary to decide which behavior should be controlled when establishing the control approach. If this behavior is expressed in terms of q, the Linear Quadratic Regulator (LQR) control design minimizes integral of a quadratic function of q and u. This process corresponds to optimization in terms of the energy concept. The purpose is to minimize the value of the integration,

$$J = \int_0^\infty q(t)^T Q q(t) + u(t)^T R u(t)\, dt, \tag{3.32}$$

where J denotes the Jacobi- Bellman cost function. Q and R are weighting matrices that scale the input and output. Subsequently, these matrices determine the level of both the control force and output to be controlled. They must be both positive semi-definite.

The employed structure model is represented from Eq. 3.6 to Eq. 3.9. In this study, the outputs are the inter-story drifts, y. Hence the expression to be minimized is given as follows;

$$J = \int_0^\infty y(t)^T y(t) + u(t)^T u(t) dt = \|y\|_2^2 + \|u\|_2^2 \,. \tag{3.33}$$

If the Riccati-equation is given:

$$A^T S + S A - S B B^T S + C^T C = 0, \tag{3.34}$$

where S is solution of the Riccati-equation.

The Lyapunov stability analysis, (Zinober (1994)), procedure gives us a definite result about the model stability. Thus, here it will be applied. Introduce the Lyapunov function as follows,

$$V(q) = q^T S\, q, \tag{3.35}$$

Derivative of $V(q)$ yields as,

$$\begin{aligned}
\dot{V}(q) &= \dot{q}^T S\, q + q^T S\, \dot{q}, \\
\dot{V}(q) &= q^T A^T S\, q + u^T B^T S\, q + q^T S\, Aq + q^T S\, Bu \\
\dot{V}(q) &= u^T B^T S\, q + q^T S\, Bu + q^T S\, BB^T S\, q - q^T C^T Cq \\
\dot{V}(q) &= (u + B^T S\, q)^T (u + B^T S\, q) - y^T y - u^T u
\end{aligned} \tag{3.36}$$

Integrate $\dot{V}(q)$,

$$\begin{aligned}
\int_0^\infty \dot{V}(q)dt &= V(q(\infty)) - V(q(0)), \\
&= -\|y\|_2^2 - \|u\|_2^2 + \left\|u + B^T S\, q\right\|_2^2 .
\end{aligned} \tag{3.37}$$

Thus,

$$\begin{aligned}
\|y\|_2^2 + \|u\|_2^2 &= \left\|u + B^T S\, q\right\|_2^2 - V(q(\infty)) + V(q(0)) \\
V(q(\infty)) &= 0 \; (if\, stable)
\end{aligned} \tag{3.38}$$

with minimum when $u = -B^T S\, q$.

The feedback system is described by $A - BB^T S$. The aim is to obtain stable eigenvalues in the left-hand plane (LHP) of the complex coordinate system.

The Riccati-equation yields as follows,

$$A^T S + SA - S\, BB^T S + C^T C = 0, \tag{3.39}$$

or more generally,

$$A^T X + XA + XRX + Q = 0. \tag{3.40}$$

Eq. 3.40 has $((2n)!/(n!)^2)/2$ solutions (n represents the number of states). A solution matrix (X) can be evaluated for each defined weighting matrix pair, Q and R. Here we have to choose Q and R that make the solution $A + RX$ or $(A - BB^T S)$ stable.

It is desired to design a controller to limit the control input (the MRD force) at 3 KN. To achieve this goal, the weighting matrices, Q and R, are selected as follows,

$$Q = 1e\,0 \begin{bmatrix} 50 & 0 & 0 & 0 & 0 & 0 \\ 0 & 10 & 0 & 0 & 0 & 0 \\ 0 & 0 & 10 & 0 & 0 & 0 \\ 0 & 0 & 0 & 1 & 0 & 0 \\ 0 & 0 & 0 & 0 & 1 & 0 \\ 0 & 0 & 0 & 0 & 0 & 1 \end{bmatrix}, \qquad R = 1e-6. \tag{3.41}$$

According to the uncontrolled structure results, the maximum inter-story displacements are found on the first floor. For this reason, the first element of the Q weighting matrix, matching the first-floor inter-story drift, is chosen larger than the remaining terms. The last three values corresponding to the velocities, which are larger in amplitude, are determined smaller than displacements to get them balanced.

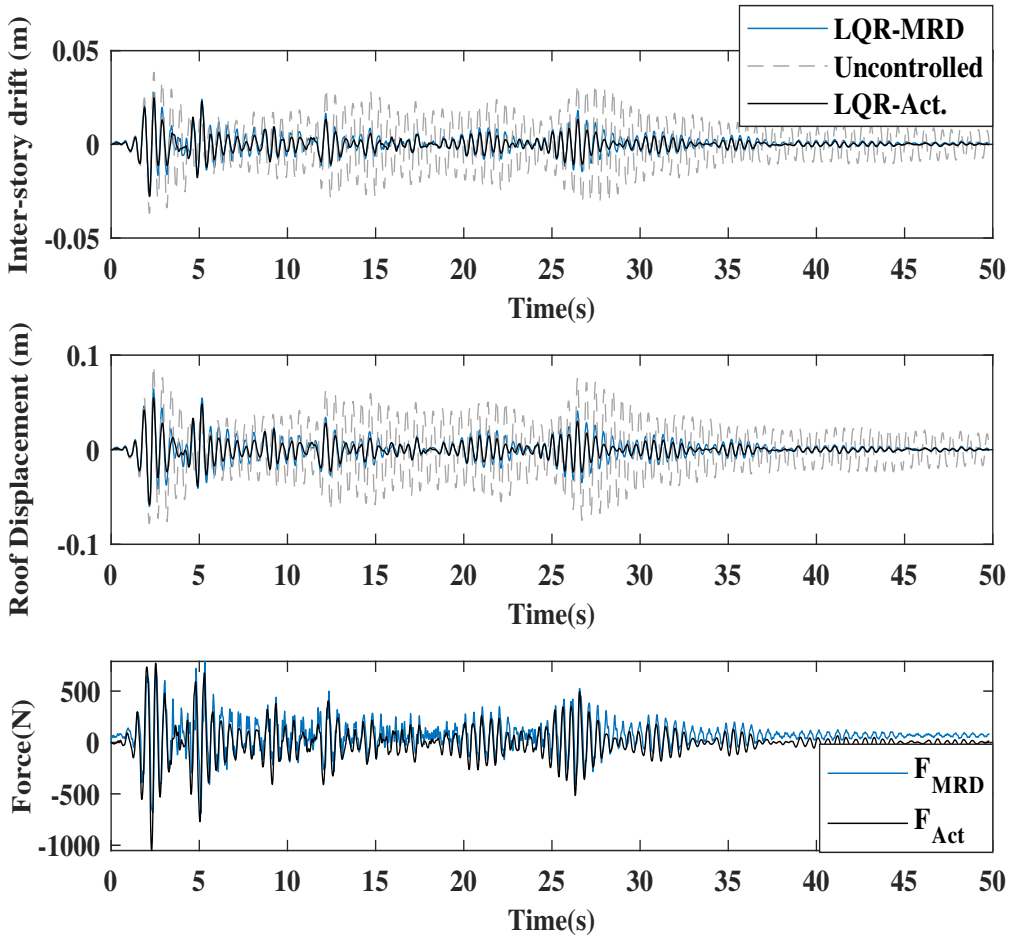

Figure 3.10. LQR-controlled structure responses

The structure with the designed controller was simulated by applying the 1940 El Centro earthquake data as a ground motion. The resulting roof, inter-story drifts, and the control force are given below. Fig.3.10 shows the maximum inter-story drifts, the top story displacements, and the active control force, F_{act}. According to the results, the adopted controller approach in the current model results in quite-promising response. The control effectiveness is higher in reducing the oscillatory behaviors which occur towards the end of the simulations.

Table. 3.2 and Fig.3.10 have demonstrated the time-domain performance comparisons. The frequency-domain characteristics for the LQR-controlled and the uncontrolled structures should be discussed to examine a controller performance appropriately. The Bode diagram for the current controller is given below.

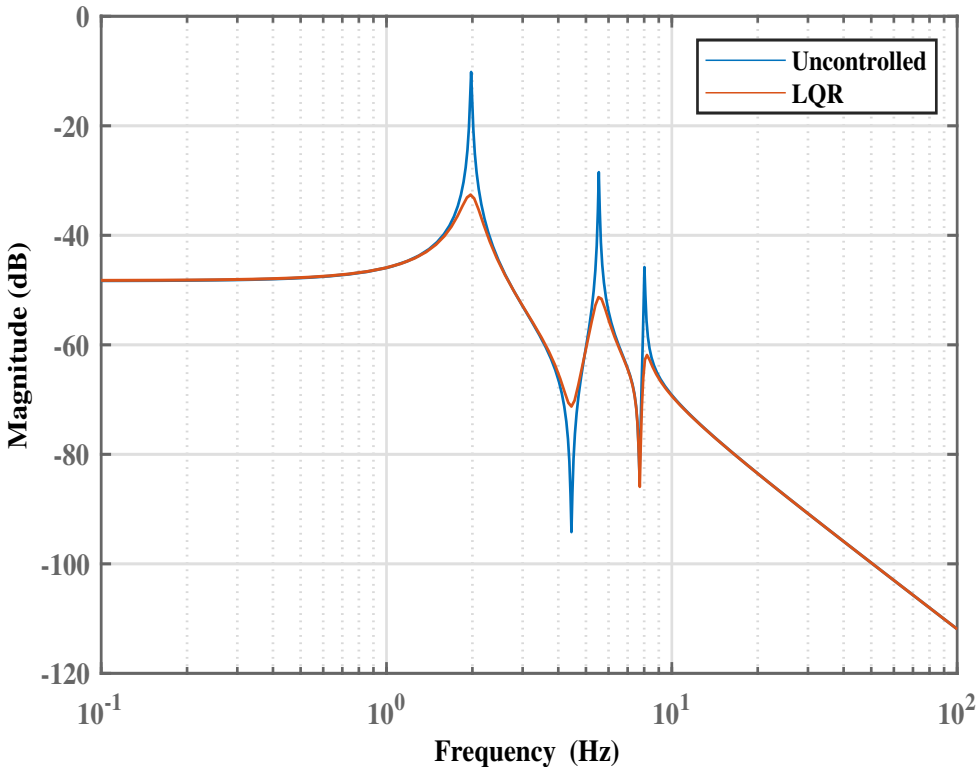

Figure 3.11. The Bode diagram of the LQR-controlled structure

Fig. 3.11 illustrates the relation between the earthquake and the top-floor displacement. For the LQR, there is roughly a $20dB$ decrement, one-tenth of the actual values, at the first mode frequency. Similar decrements exist in the higher modes. On the contrary,

in the time history simulation, there is no such significant top-floor displacement reduction because the excitation frequency content does not equally cover the entire frequency domain. Accordingly, local decrements on the frequency domain do not account for equal decrements on the time domain.

Table 3.2. Performance indices of LQR controller

	J_1	J_2	J_3	J_4	J_5	J_6	J_7	J_8
LQR	0.6606	0.6547	0.6707	0.7905	0.3971	0.3452	0.7594	0.4259

In Table. 3.2, performance indices are computed for the uncontrolled and LQR-MRD controlled structures. Results for the active controller are not shown because it is readily seen in Fig.3.10 that the responses of the MRD and the actuator are almost identical. According to the results given in Table. 3.2, it is confirmed that the structure empowered with an LQR outperforms the uncontrolled structure in J_1 and J_5 indices. These indices are the crucial ones in representing the controller's efficiency since they stand for the maximum inter-story and 2-norm of the displacements, respectively.

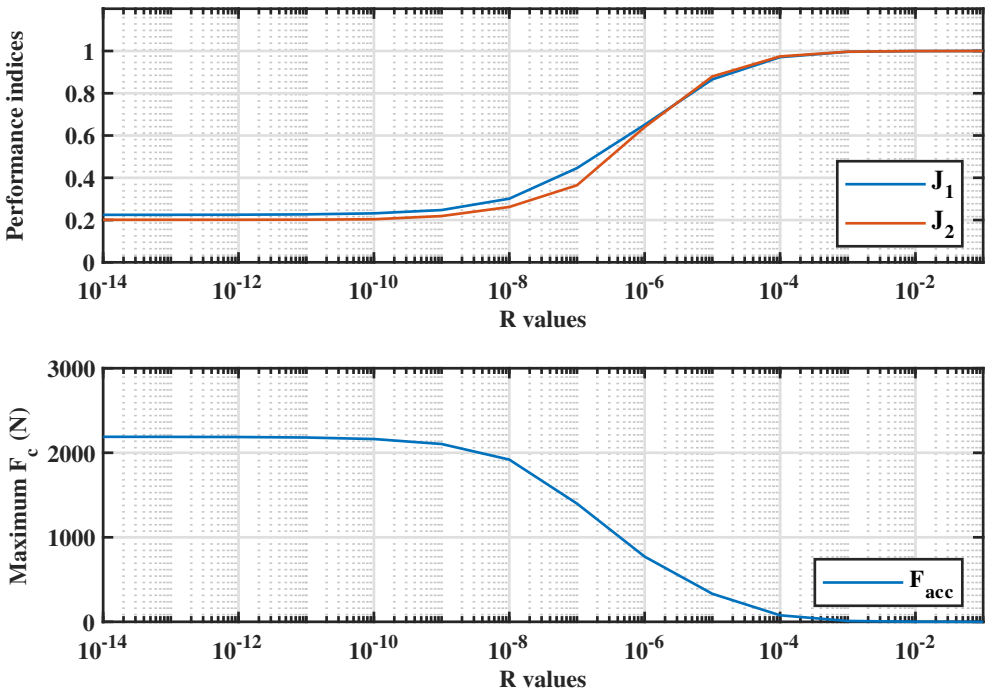

Figure 3.12. LQR weight optimization

In the implementation of the LQR control algorithm, an optimization study for weight selection is undertaken. As implied before, the ratio between the weights determines the level of the control force. To investigate the effect of weight ratio, R values versus the maximum control forces, and the performance indices are plotted in Fig. 3.12.

Table. 3.3 shows the performance indices, and all indices are worse than the LQR controlled structure performances given in Table. 3.2.

Table 3.3. Performance indices of 0V-driven MRD

	J_1	J_2	J_3	J_4	J_5	J_6	J_7	J_8
0V MRD	0.7486	0.7399	0.6539	0.8096	0.4255	0.4051	0.7839	0.4378

As seen in Fig. 3.12, R values smaller than 10e-8 do not affect the level of control values. Similarly, the performance indices, J_1 and J_2, cannot be reduced more than 0.2 for the same R-value range. Thus, R is chosen as $1e-8$ to compute the control gains, and the simulations are carried out.

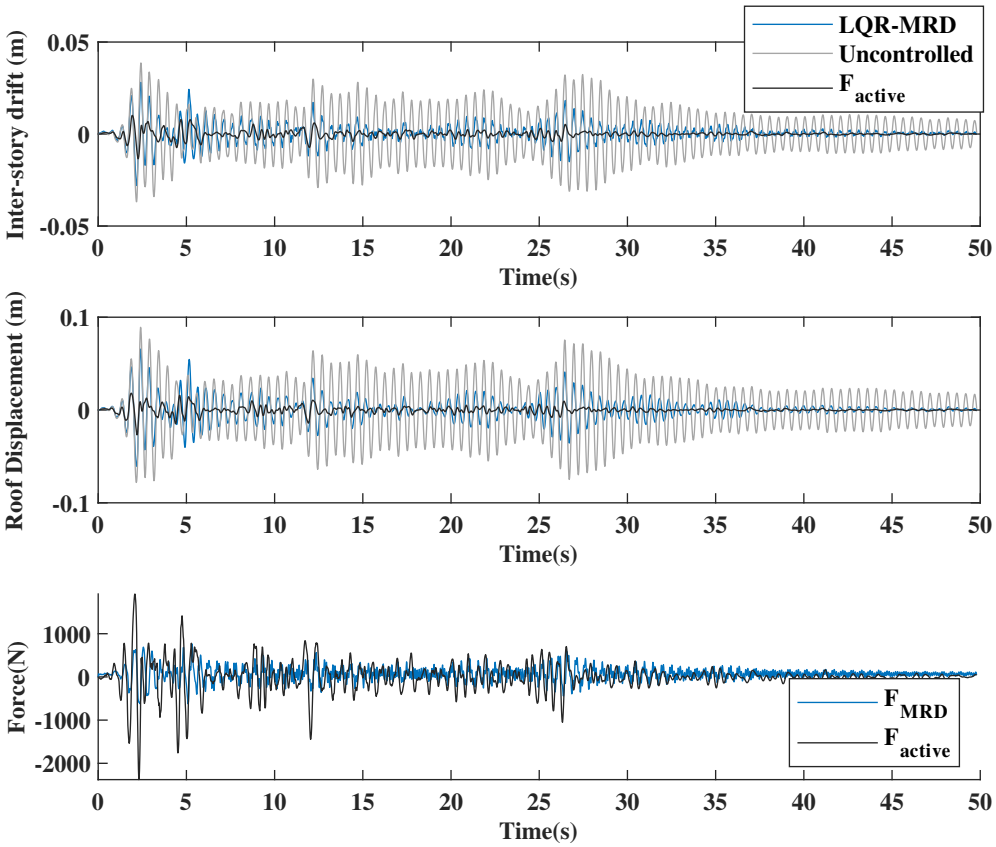

Figure 3.13. LQR-controlled structure responses for $R = 1e-8$

Fig. 3.13 shows the responses of the LQR-controlled structure. In this particular case, the active control algorithm works as expected; however, the MRD cannot follow the actuator. The reason behind this may be the low level of displacements and velocities that form the required control forces. Since the demand is huge, the given voltage level is not able to get the MRD to produce the control force. For this reason, the first applicable R-value is chosen as $1e-6$.

An implemented semi-active control strategy may be substituted for a passive device. For instance, in our case, the employed MRD can be driven by a constant voltage or even without a power supply. Accordingly, a passive device is tested in which there is no need for measurements and a control setup. It should be examined whether the MRD with a constant voltage is better than the actively controlled MRD.

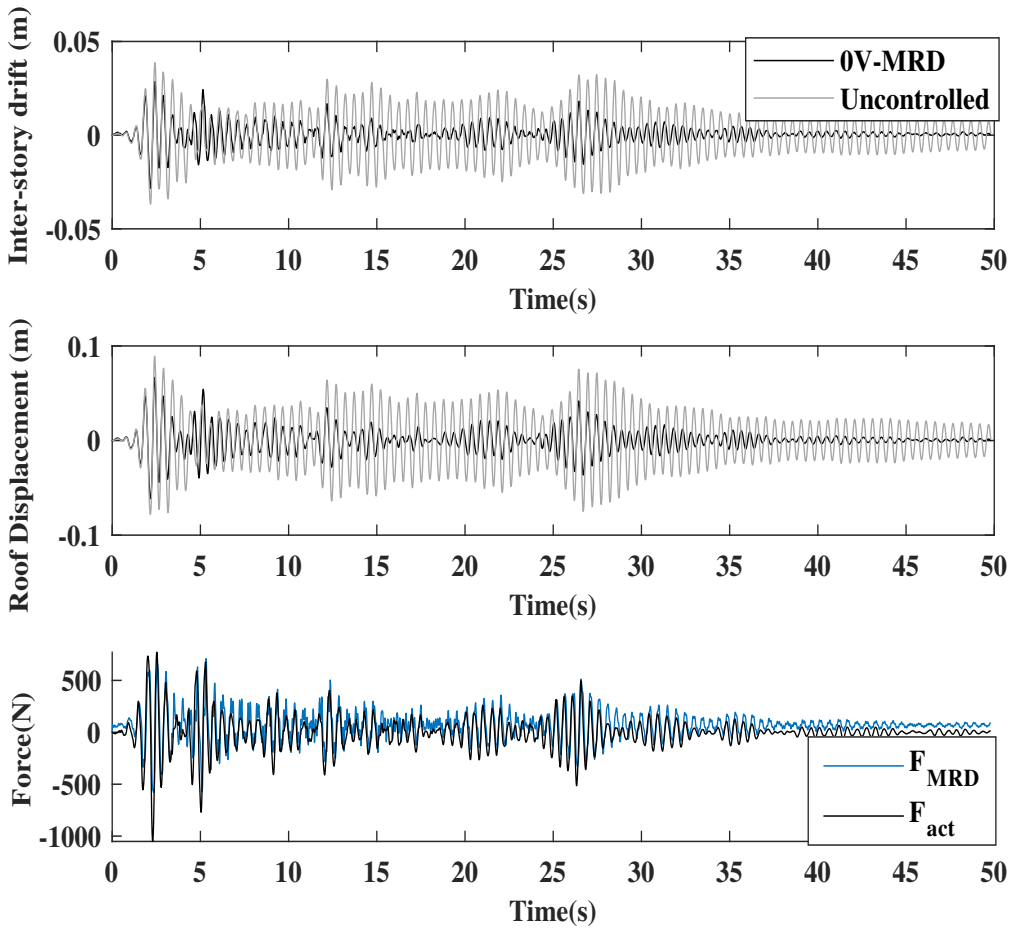

Figure 3.14. Responses of structure with a 0V-driven MRD

Fig. 3.14 shows the response of the structure having an MRD without a power supply. As expected, the MRD cannot produce the required control force, and hence the applied passive controller strategy results in larger displacements. In other words, the actively driven voltage MRD outperforms the MRD utilized as a passive controller.

3.2.4. PDD Controller

A state-space representation can be shown as the following equations. Here, the control input, u, is demonstrated by multiplying the states by the gain vector, K, as depicted in Fig. 3.15.

$$\begin{aligned} \dot{q} &= Aq + B_1 w + B_2 u \\ y &= Cq + D_1 w + D_2 u \\ u &= -Kq \end{aligned} \tag{3.42}$$

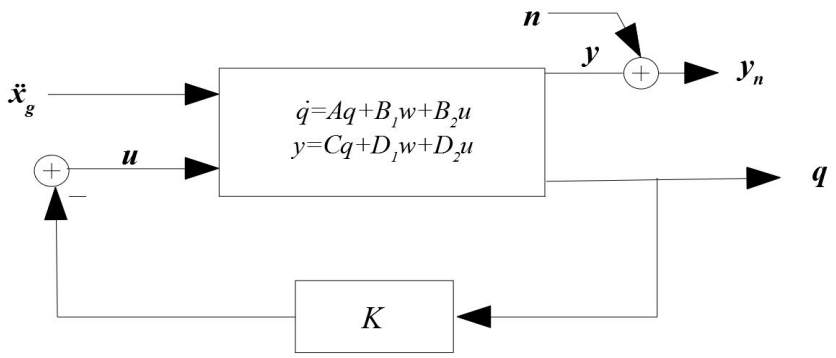

Figure 3.15. State-space feedback proportional control

The proportional gain allows us to control disturbances in terms of error multiples. At first sight, the system state variable, q, consists of the structural displacements and their derivatives, which may appear as if a PD controller exists already. However, it must be considered that the state equations have been derived from a second-order differential equation, and thus, an error correction for the acceleration variables is not proportionally considered. To see the acceleration effect on the control, a PDD controller is employed as shown in Fig. 3.16. Therefore, 3 measurements are required.

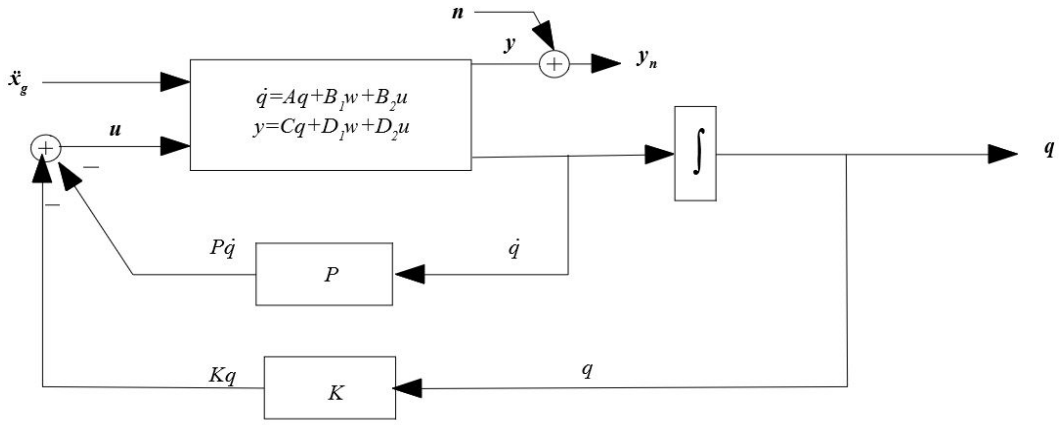

Figure 3.16. State-space feedback proportional-derivative (PD) control

The control input with the proportional, derivative and double derivative of the displacements (PDD) yields,

$$u = -Kq - P\dot{q}. \tag{3.43}$$

The closed loop state space representation becomes as follows;

$$\dot{q} = (I + B_2P)^{-1}(A - B_2K)q + (I + B_2P)^{-1}B_1w, \tag{3.44}$$

where P and K are formed as follows;

$$\begin{aligned} K &= [K_{d1}\ K_{d2}\ K_{d3}\ K_{v1}\ K_{v2}\ K_{v3}], \\ P &= [P_{v1}\ P_{v2}\ P_{v3}\ P_{a1}\ P_{a2}\ P_{a3}], \end{aligned} \tag{3.45}$$

where K_{di} is the proportional gain that corresponds to the i'th floor displacement, $K_{vi} = P_{vi}$ are the gains for velocities, and P_{ai} is the proportional gain for the accelerations. These values are tuned regarding the uncontrolled structure response amplitudes, d_i, v_i and a_i, given in Fig. 3.17 to achieve a classical PD control approach in a heuristic way which was proposed by Ziegler and Nichols (1993).

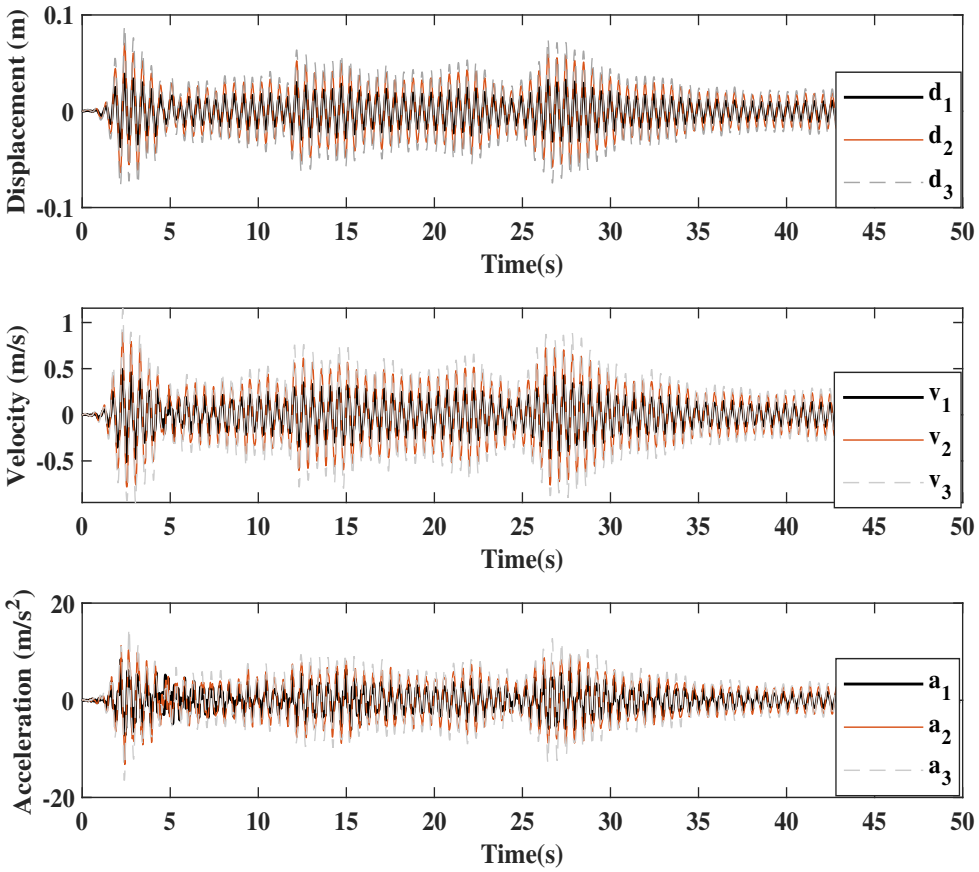

Figure 3.17. The uncontrolled structure responses

After the fine-tuning process, K and P are updated as follows,

$$K = [187500\ 262500\ 375000\ 4425\ 6195\ 8850],$$
$$P = [4425\ 6195\ 8850\ 156.2500\ 218.7500\ 312.5]. \quad (3.46)$$

The structure with the PDD controller was simulated, and the maximum inter-story drifts and the top story displacements are shown in Fig. 3.18. At a glance, the current controller reduces the input energy significantly. Regardless of the control devices; active vs semi-active, results are alike. Besides, the MRD control force tries to mimic the active control force. A bias of 70 N is visible which seems to correspond to the internal unbalanced force of the MRD. It is noteworthy to mention that the LQR control force in Fig. 3.10 is smaller than the PDD force. One of the reasons can be associated to the PDD controller, which does not consider the control force as an optimization criterion.

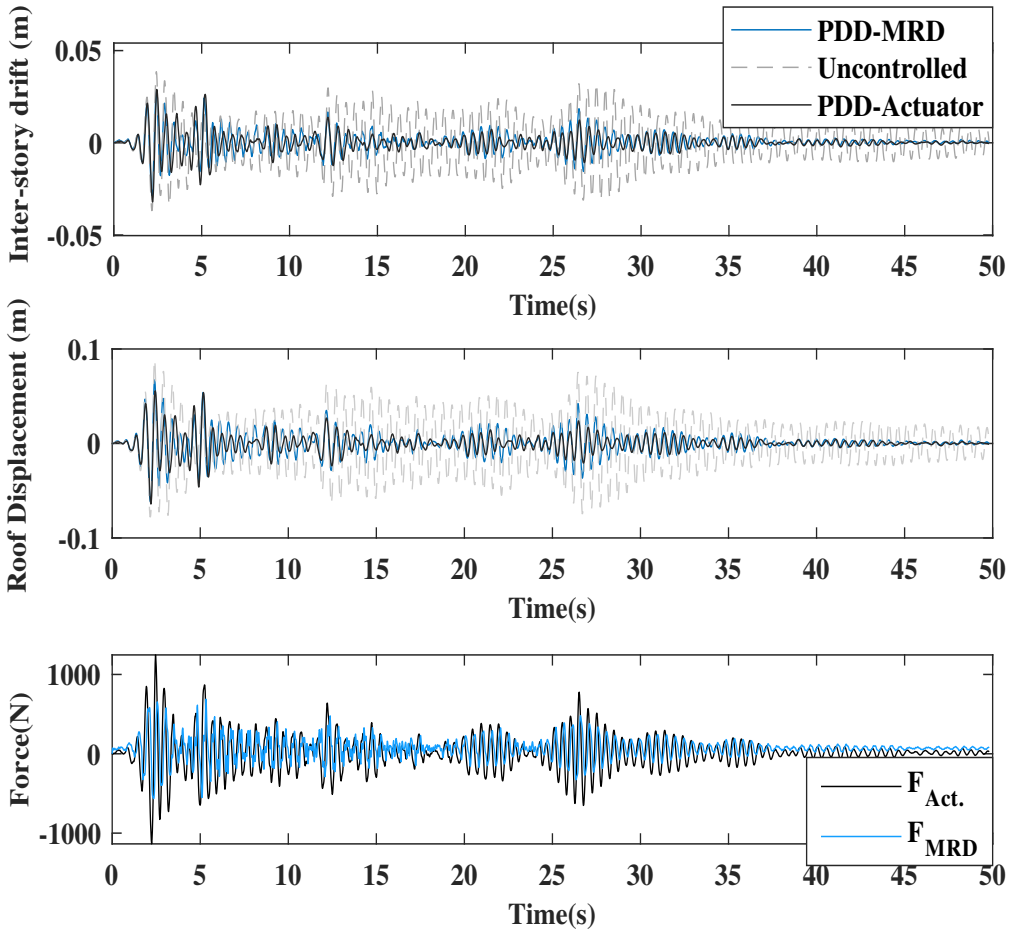

Figure 3.18. The PDD-controlled structure responses

Table 3.4. Performance indices of the PDD controller

	J_1	J_2	J_3	J_4	J_5	J_6	J_7	J_8
PDD cont.	0.7020	0.6584	0.8127	0.8127	0.4226	0.4020	0.7883	0.4417

To inquire the frequency-domain characteristics for both structures; controlled and uncontrolled; the Bode magnitude diagram is given as follows,

Fig. 3.19 illustrates the ratio between the excitation input and the top-floor output. There is more than $20dB$ decrement at the first mode frequency. Besides, a frequency-shift occurs because of the addition of the acceleration errors. This frequency-shift may be why the current controller does not outperform the LQR even if it does not restrict the control input.

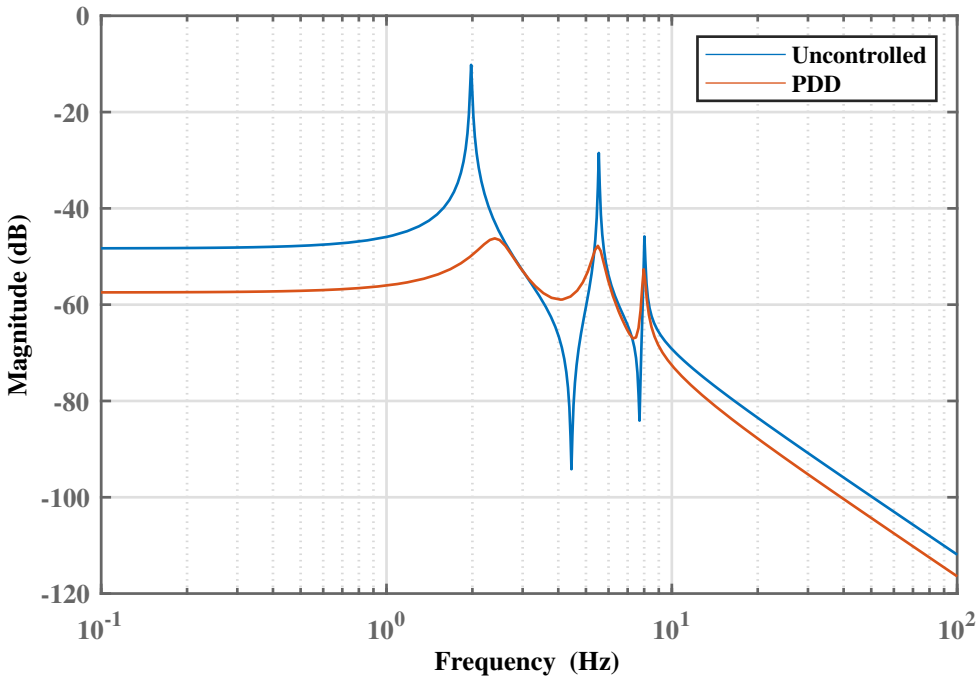

Figure 3.19. The Bode diagram of the PDD-controlled structure

3.2.5. Pole-Placement Controller

The pole-placement controller is one of the conventional control algorithms and a frequency-based control approach. The pole-placement (PP) control, is tested by employing the Ackermann formula (Ackermann (1928)). In this approach,the Ackermann formulation enables the designer to place the poles at any desired locations in theory. The i'th pole that corresponds to the i'th natural frequency of the uncontrolled structure is expressed as follows,

$$p_i = -|\omega_i| * \zeta_i + \omega_i j, \tag{3.47}$$

where the imaginary part is equal to the natural frequency, ω_i, and the reel part consists of the natural frequency multiplied by the damping ratio ζ_i. Accordingly, the poles of the 3-story structure yield,

$$P = \begin{bmatrix} -0.2099 + 50.3653i \\ -0.2099 - 50.3653i \\ -0.1332 + 34.8539i \\ -0.1332 - 34.8539i \\ -0.0706 + 12.4391i \\ -0.0706 - 12.4391i \end{bmatrix}. \tag{3.48}$$

These given poles can be placed such that the structural modal frequency response magnitudes are smaller than the uncontrolled structure. In this particular application, the aim is to modify the damping ratio.

$$\bar{P} = \begin{bmatrix} -f * 0.2099 + 50.3653i \\ -f * 0.2099 - 50.3653i \\ -f * 0.1332 + 34.8539i \\ -f * 0.1332 - 34.8539i \\ -f * 0.0706 + 12.4391i \\ -f * 0.0706 - 12.4391i \end{bmatrix}, \tag{3.49}$$

where f represents the ratio of the decrement for the new poles. In our model, it is aimed to decrease the amplitude of the corresponding natural mode frequencies by $20dB$ ($f = -20dB$). Consequently, to achieve the poles of $\bar{P}$, the Ackermann formula results in the controller gains, K, as follows:

$$K = 1.0e + 03 * \begin{bmatrix} 4.7077 & -7.0639 & 3.3515 & 1.4893 & -0.2613 & 0.6024 \end{bmatrix}.$$

To inquire the frequency-domain characteristics for both structures; the controlled and the uncontrolled; the frequency relation between earthquake input and the roof displacement is given below.

Fig. 3.20 shows that there are $20dB$ decrements at all natural frequencies without effecting pole locations significantly. As in the PDD controller, the control input optimization is not considered in the current controller. During the tuning of the decrement ratio, f, it was increased incrementally and the closed-loop system is simulated. $f = 20dB$ value was chosen because higher values resulted in some upthrusts between the $4Hz$ and $5Hz$ bandwidth. As a result, the structural response worsens since the implemented controller

does not take disturbances into account. To be more precise, there is no disturbance modeling consideration in the control implementation, such as the Kanai-Tajimi spectrum.

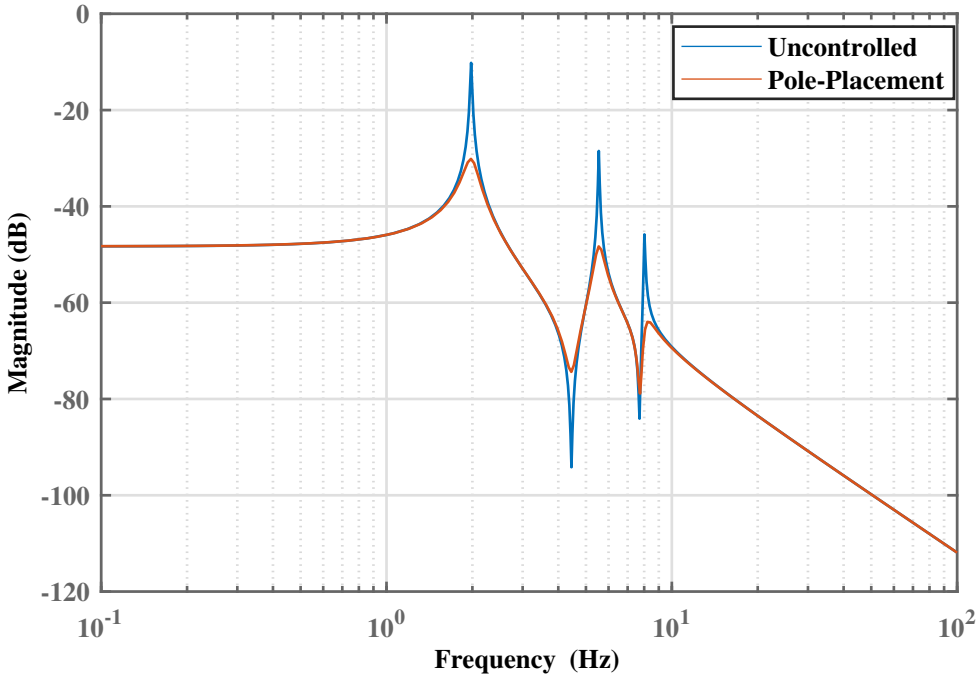

Figure 3.20. The Bode diagram of PP-controlled structure

The structure with the pole-placement controller was simulated. Table. 3.5 confirms that the controlled structure results in better performance than the uncontrolled structure in every index. It is seen that the current control strategy shows better performance than the passively-used MRD (Table. 3.3).

Table 3.5. Performance indices of the pole-placement controller

	J_1	J_2	J_3	J_4	J_5	J_6	J_7	J_8
Pole-pl.	0.6944	0.7053	0.6560	0.8081	0.4162	0.4036	0.7778	0.4226

Fig. 3.21 shows the maximum inter-story drifts, the top story displacements, and the control forces. At first sight, the current controller conduces similar results to the former controllers. The MRD successfully followed up the active control force except for the $70N$ offset.

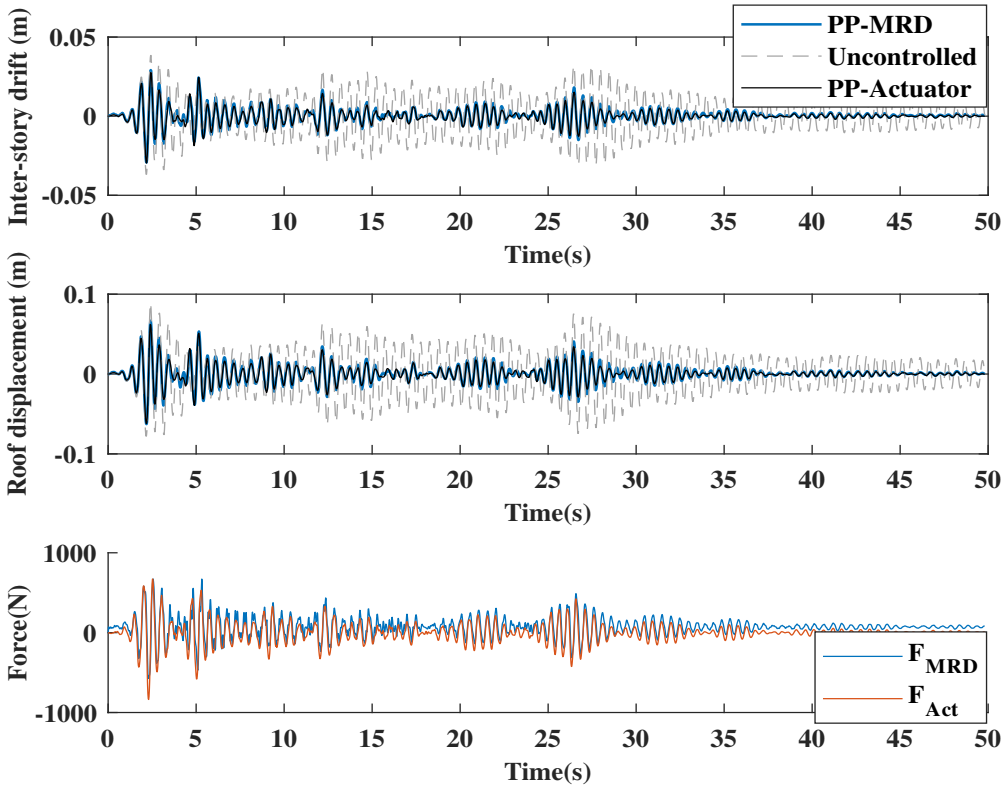

Figure 3.21. Responses of the PP-controlled structure

In Fig. 3.22, the normal stress, σ, for the first floor column is shown. It can be seen that, the stresses are well-below the yielding stress, σ_y , under the El Centro EQ.

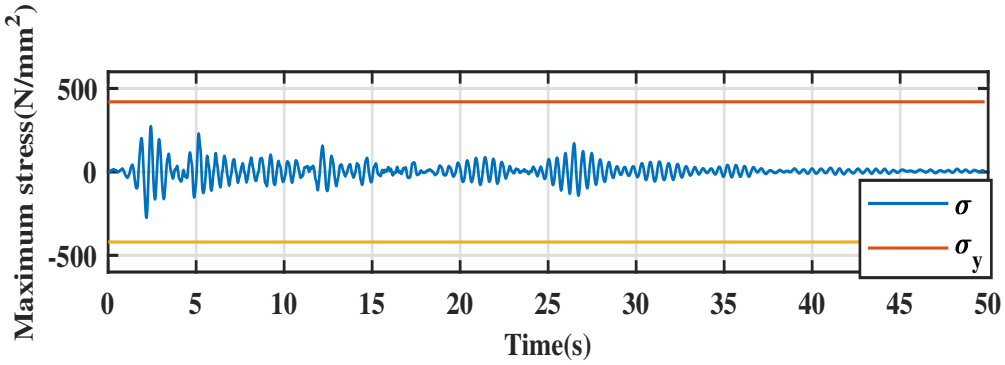

Figure 3.22. Maximum stresses

3.2.6. H_∞ controller

In this section, a design procedure of H_∞ controller for a generalized civil structure plant will be explained. H_∞ methods are utilized in control theory applications to synthesize the required controllers in regulating structural system output. To employ an H_∞ method, the designer puts forward the optimization criteria, and then solves this expression by minimizing the H_∞-norm. H_∞ controllers outperform classical controllers because they can be utilized for MIMO systems including cross-coupling between channels (Glover and Doyle (1988), Doyle et al. (1989), Skogestad and Postlethwaite (2007)). However, it requires a certain level of mathematical knowledge to implement the conditions successfully and to express the model with reasonable assumptions. It is noteworthy that the resulting controller will be the best solution for the current structure with the pre-assumed cost function.

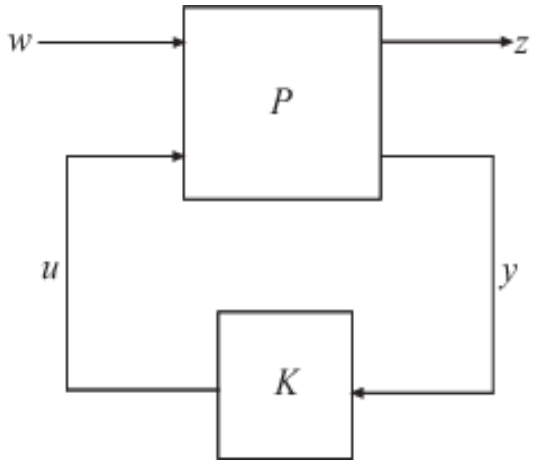

Figure 3.23. H_∞ control problem statement

If the problem formulation is stated, the general structure plant has to be represented according to the standard configuration above in Fig. 3.23.

The structure plant P has two inputs, the exogenous input w including noises and disturbances, and the control force u. There are two outputs, the error signals (exogenous outputs), z, composed of the responses that the designer wants to minimize, and the measurement signals, y. It should be kept in mind that all these inputs and outputs are generally vectors, whereas P and K are system matrices.

$$\begin{bmatrix} z \\ y \end{bmatrix} = \begin{bmatrix} P(s) \end{bmatrix} \begin{bmatrix} w \\ u \end{bmatrix} = \begin{bmatrix} P_{11}(s) & P_{12}(s) \\ P_{21}(s) & P_{22}(s) \end{bmatrix} \begin{bmatrix} w \\ u \end{bmatrix}$$

$$u = K(s)y, \tag{3.50}$$

where s denotes the Laplace domain ($s - domain$). The input-output relation from w to z is called the lower linear fractional transformation (LFT):

$$z = F_L(P, K)\, w \tag{3.51}$$

Here, $F_L(P, K)$ is the lower LFT, which can be derived as follows

$$F_L(P, K) = P_{11} + P_{12}K(I - P_{22}K)^{-1}P_{21}. \tag{3.52}$$

The aim of the H_∞ controller is similar to quadratic-based ones, but it also satisfies to minimize the H_∞ norm with the condition:

$$\|F_L(P, K)\|_\infty = \sup_\omega \bar{\sigma}\left(F_L(P, K)\,(j\omega)\right) \tag{3.53}$$

where $\bar{\sigma}$ is the maximum singular value of the matrix $F_L(P, K)(j\omega)$, and $\sup_\omega$ refers to the maximum value over the frequency domain.

The system plant can be represented by implementing the equation of motion for the structure, the measurement and output dynamics as a state-space representation.

$$\begin{aligned} \dot{x} &= Ax + B_1 w + B_2 u \\ z &= Cx + D_{11} w + D_{12} u \\ y &= Cx + D_{21} w + D_{22} u \end{aligned} \tag{3.54}$$

The closed-loop system's satisfactory H_∞ norm is achieved through the matrix D_{11} in the P's state-space form (A, B_1, B_2, C_1, C_2, D_{11}, D_{12}, D_{21}, D_{22}). To solve this optimization problem, there are three different main approaches:

- Linear matrix inequality (LMI): It requires the fewest number of assumptions (Boyd et al. (1994)).
- Riccati-based equations: Two AREs are needed to be able to solve the problem.
- Youla-Kucera parameterization: It generally results in a high number of states (Kucera and Outrata (1988)).

A block diagram depiction of the civil structure system for the current study is represented in Fig. 3.24. G represents the 3-story structure with force inputs and measurement outputs. The frequency-domain weighting function W_g forms the spectral content of the disturbance, $\ddot{x}_g$, modeling the earthquake excitation.

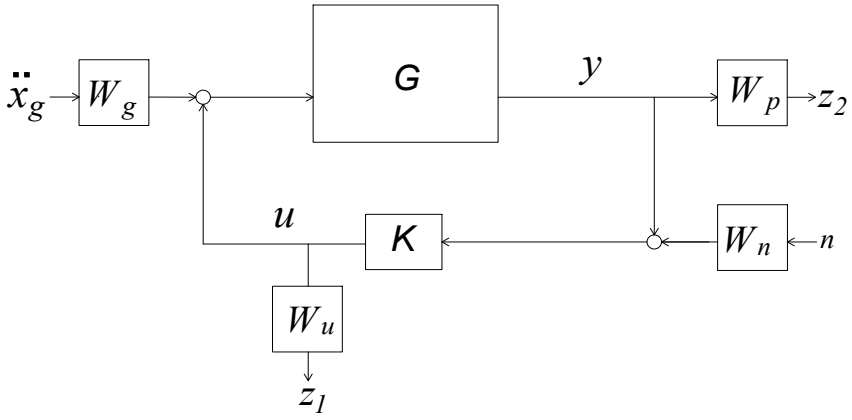

Figure 3.24. The generalized plant for a seismically excited nominal civil structure

The Kanai-Tajimi spectrum is illustrated in Fig. 3.25, Lin and Yong (1987), which is designed according to the implemented earthquakes, given in Chapter 2. A decent fit is obtained by employing the parameters $\zeta_g = 0.25$ and $\omega_g = 8.65 rad/s$ in a second-order model. A higher degree model may be used as well, but this penalizes the controller by a higher number of states.

The matrix W_p is weighting the controlled response, and W_u is weighting the control force signal. W_n is used to weight the measurement noise n. The signal to noise ratio (SNR) and cut-off frequency was set as 10 and $100Hz$, respectively.

The exogenous input signal w consists of the earthquake excitation $\ddot{x}_g$ and the measurement noise n. The exogenous output z consists of the frequency weighted controlled response and the control force input. These signals are weighted by a performance, and a control weight: W_p and W_u, respectively. The aforementioned weights are chosen

after a few trials as, $W_p = diag(\ [\ 500\ 100\ 100\ ]\ )$ and $W_u = 5e-4$. Above all, by these chosen weights, the signal magnitudes are brought to a common ground based on the chosen units. Accordingly, the designer can fine-tune the controller.

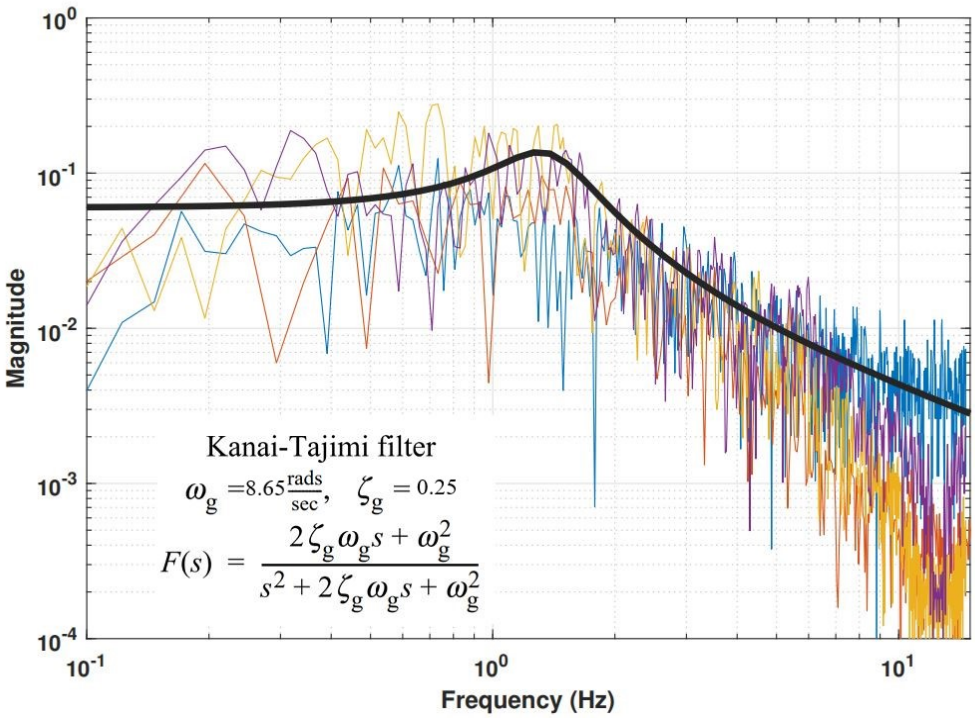

Figure 3.25. The designed Kanai-Tajimi filter

Simulations for the structure with the H_∞ controller were undertaken in the Matlab environment. While constructing the generalized structure plant, the *iconnect* function in the Robust Control Toolbox is made use of. This function helps the designer build large plants, including complex channel relations easily. The satisfactory controller is achieved by employing the 2 AREs. The yielding controller solution for the given problem statement, K_∞, has 11 states, whereas the structure system, G, has only 6 states. The difference comes from the included weighting functions, W_g and W_n, in the generalized structure plant.

Fig. 3.26 shows the maximum inter-story drifts and the top story displacements. Apparently, the H_∞ controller yields better results compared to the previous controllers in the structural responses. Also, the current controller requires higher controller force input.

Table. 3.6 confirms that the H_∞-controlled structure outperforms the any other controller and results in better performance than the uncontrolled structure in every index.

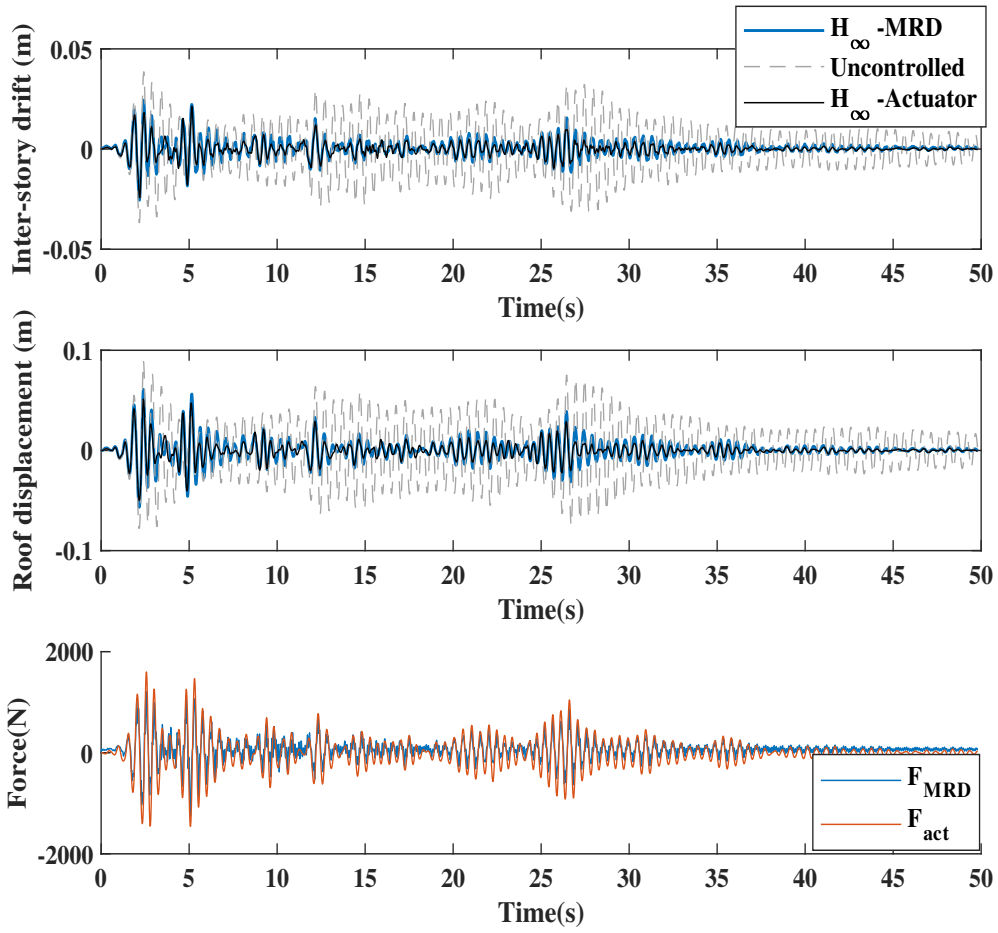

Figure 3.26. The H_∞-controlled structure responses

Even though the control force for this controller is much larger than previous control applications, the performance indices J_3, J_4, J_7 and J_8 do not seem to be affected that much.

Table 3.6. Performance indices of the H_∞ controller

	J_1	J_2	J_3	J_4	J_5	J_6	J_7	J_8
H_∞ **cont.**	0.6447	0.6205	0.7434	0.7550	0.3836	0.3556	0.7407	0.4053

At last, to compare the frequency-domain characteristics for both structures; controlled and uncontrolled; the Bode diagram is given in Fig. 3.27. It is seen that there is more than 30 dB decrement at the dominant modal frequency. Thus, the theory of the H_∞-norm technique can be counted valid, since the first mode corresponds to the supre-

mum of the σ. Moreover, the current controller takes into account the controller input force optimization in the range of the designer's priorities.

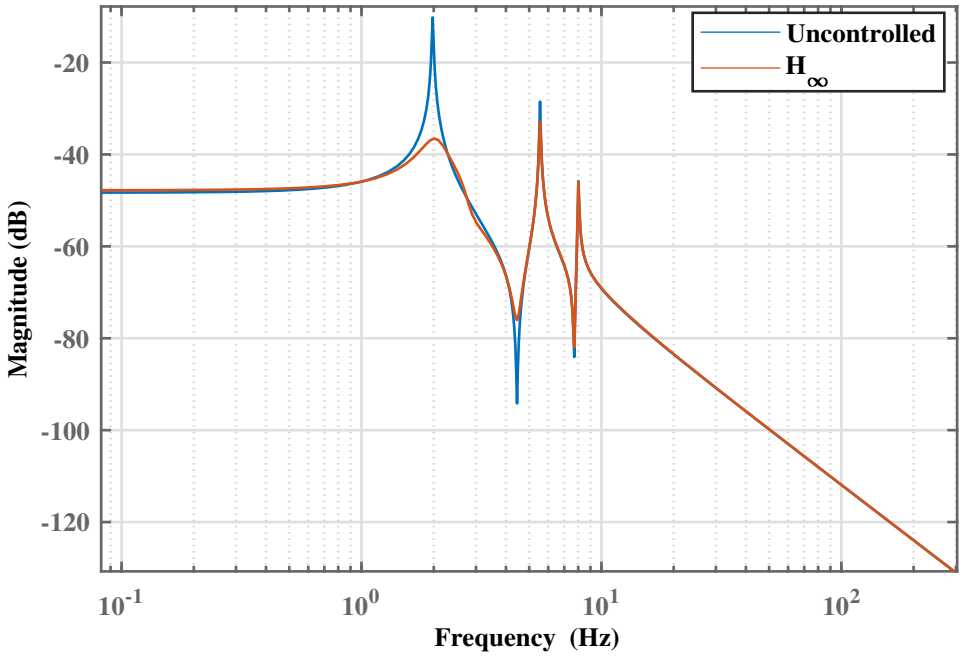

Figure 3.27. The bode diagram of H_∞-controlled structure

3.2.7. H_2 controller

The H_2 control, one of the quadratic control algorithms, is tested in this section. Similar to the H_∞-controller, it takes into account the control input optimization in theory. Also, the same mathematical model, including all the weights, W_p, W_u, W_g, and W_n, are employed to form the H_2 control problem.

The aim of the H_2 controller is similar to the LQR, and it tries to minimize the H_2 norm with the condition of:

$$\|F_L(P,K)\|_2 = \sqrt{\frac{1}{2\pi}\int_{-\infty}^{\infty}\left(F_L(P,K)\left(j\omega\right)\right)\left(F_L(P,K)\left(j\omega\right)\right)^{\dagger}\,d\omega}, \tag{3.55}$$

where † is the Hermitian operator.

An advantage of the H_2-controller over the conventional quadratic controllers is that it does not require all the states data. In other words, as long as it is a controllable

system (Rubio (1971)), the number of outputs achieved is enough, and, thus, no need for an observer design. H_2 controller can be interpreted as a combination of a Linear Quadratic Estimator (LQE), and an (LQR), which are connected serially. The output of the system enter the LQE, and the estimated states proceed to the LQR. Accordingly, the required control input is achieved. In the H_2 controller, all these separate operations are handled at once by a weighted LQE-LQR-like controller.

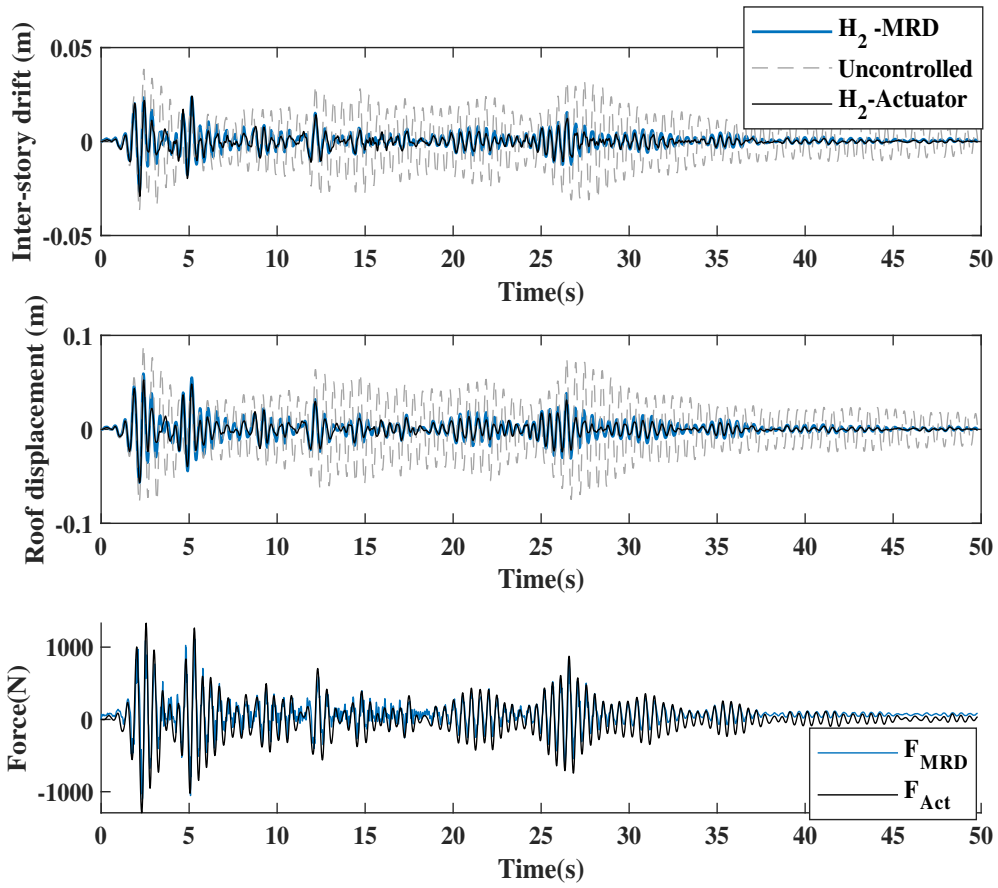

Figure 3.28. Responses of the H_2-controlled structure

The current structure within the given problem definition defined in H_∞ section and the optimization criteria was simulated, and a satisfactory controller, H_2, is achieved. Similarly, H_2 has 11 states as the H_∞-controller has. Fig. 3.28 shows the maximum inter-story drifts, the top story displacements, and the control forces. Results are quite akin to the LQR controller implementation. Even though all the weights are the same with the H_∞ algorithm, the controller force is smaller than the H_∞ in magnitude.

Table 3.7. Performance indices of the H_2 controller

	J_1	J_2	J_3	J_4	J_5	J_6	J_7	J_8
H_2 **controller**	0.6645	0.6404	0.6400	0.7552	0.3796	0.3536	0.7342	0.3953

Table. 3.7 shows that the controlled structure results in as good performance as the H_∞-controlled structure in J_1, J_2, J_5 and J_6 indices by slight differences.

The Bode diagram is given to compare the frequency-domain characteristics for the controlled and the uncontrolled structures.

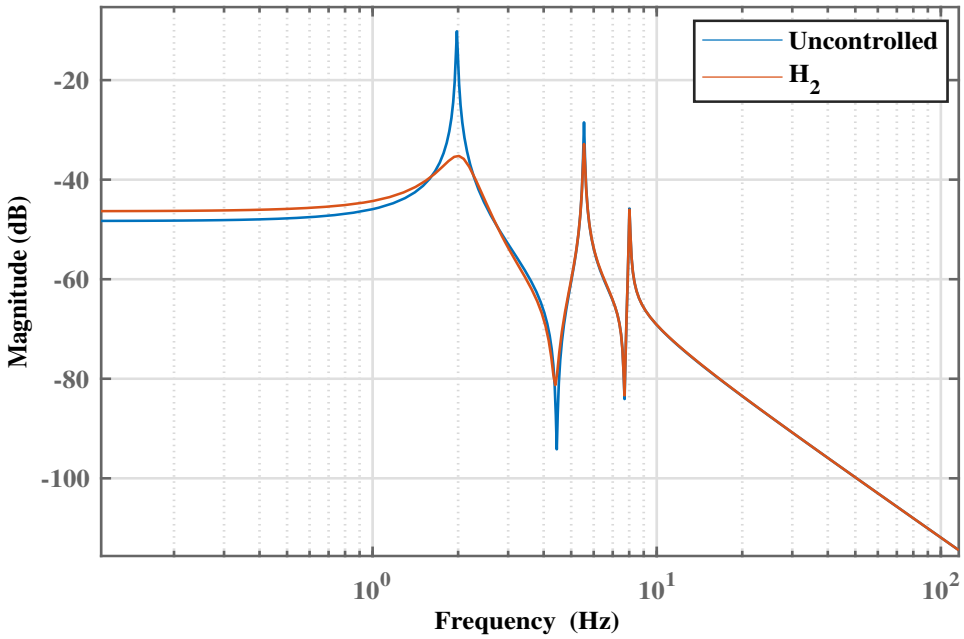

Figure 3.29. The Bode diagram of the H_2-controlled structure

Fig. 3.29 shows that there is more than $20dB$ decrement at the first mode and around $5dB$ at the second mode. Seemingly, it works like the H_∞-controller. However, there are also certain reductions in the following modes, as expressed in the cost function of the H_2-controller. In addition, the current controller upthrusts the frequency response amplitudes before the first mode by $5dB$.

The FFT values of the El Centro earthquake is multiplied by the system frequency response in Fig. 3.30. It is seen that the H_∞-controller shows smaller inter-story drifts than the H_2-controller.

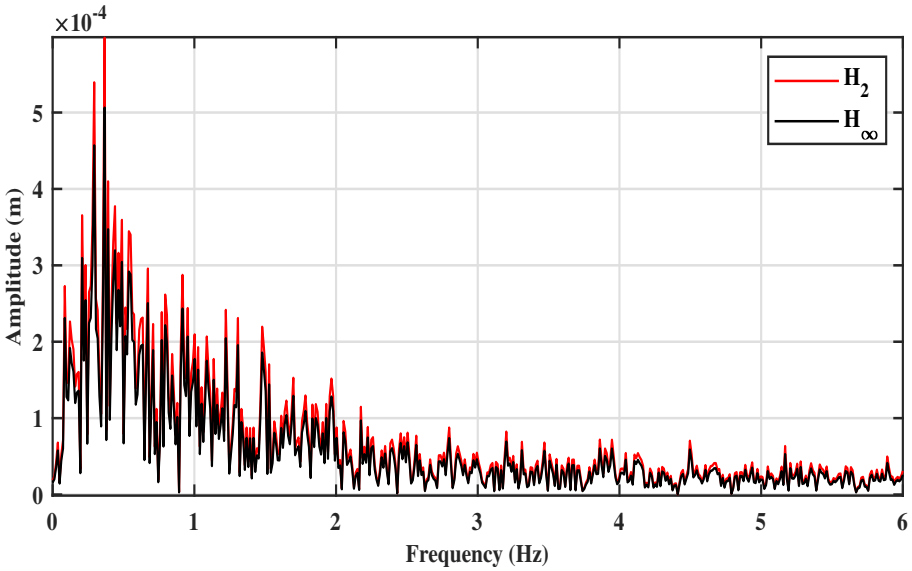

Figure 3.30. H_2 and H_∞-controlled structures response spectra

3.3. Passive Controllers

In this section, the passive controllers: a friction pendulum bearing system and a tuned mass damper, will be implemented on the 3-story structure. Subsequently, the responses of the structure with these passive controllers will be compared to the uncontrolled reference structure.

3.3.1. Friction Pendulum Bearing System (FPBS)

The FPBS acts like a fuse triggered only when the seismic forces get bigger than the static friction. After the motion, the bearing promotes a lateral force equivalent to the summation of the mobilized frictional force and the restoring force. The rise of the structure throughout the rounded surface produces this restoring force. There is a linear relationship between this force and the weight, and this force is inversely proportional to the radius of the rounded surface.

In Fig. 3.31, the 3-story structure equipped with an FPBS is illustrated. A notable aspect in expressing the complete equations of motion of the structure isolated with the FPBS is to define the isolator's force-deformation constitutive relationship. The complexity involved in formulating this relationship is linearly related to the model's certainty.

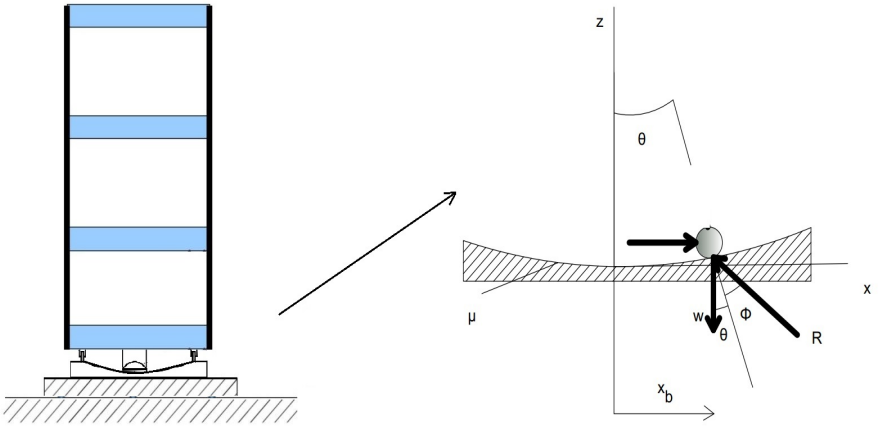

Figure 3.31. The FPBS-installed structure

The matrices that form the equation of motions are updated as follows,

$$K_{FPBS} = \begin{bmatrix} k_b + k & -k & 0 & 0 \\ -k & 2k & -k & 0 \\ 0 & -k & 2k & -k \\ 0 & 0 & -k & k \end{bmatrix}, C_{FPBS} = \begin{bmatrix} c_b + c & -c & 0 & 0 \\ -c & 2c & -c & 0 \\ 0 & -c & 2c & -c \\ 0 & 0 & -c & c \end{bmatrix}, M_{FPBS} = \begin{bmatrix} m_b & 0 & 0 & 0 \\ 0 & m & 0 & 0 \\ 0 & 0 & m & 0 \\ 0 & 0 & 0 & m \end{bmatrix}, \tag{3.56}$$

where $m = m_b = 200kg$, $c_b = 348Ns/m$, and $k_b = 18312N/m$ are the base mass, the FPBS damping, and stiffness, respectively. For a radius of curvature, R_o, the restoring force can be evaluated according to Eq.3.57.

$$f = \frac{W}{R_o} x_b + \mu W sgn(\dot{x}_b), \tag{3.57}$$

where W represents the total weight of the structure moving on the isolator; x_b and $\dot{x}_b$ are the lateral deformation and velocity of the isolator relative to the ground, k is the friction coefficient; $sign(\cdot)$ is the signum function, and f is the horizontal restoring force. The vertical component of ground motion was neglected in our experimental set-up as Zayas et al. (1989) proposed in Eq. 3.57, because taking into account the vertical component

caused a reduction of 1.2 percent of the total ground motion's magnitude. All the approximations made above are valid as long as the vertical component of the ground excitation is overlooked.

The natural period of the FPBS is considered as the most important criterion for the passive control of the structures in terms of feasibility.

$$T_b = 2\pi \sqrt{\frac{R_o}{g}}, \tag{3.58}$$

where T_b is the natural period of the FPBS and g is the gravitational acceleration. According to El Centro earthquake response spectra given in Fig. 3.32, T_b is aimed at 1.4 seconds.

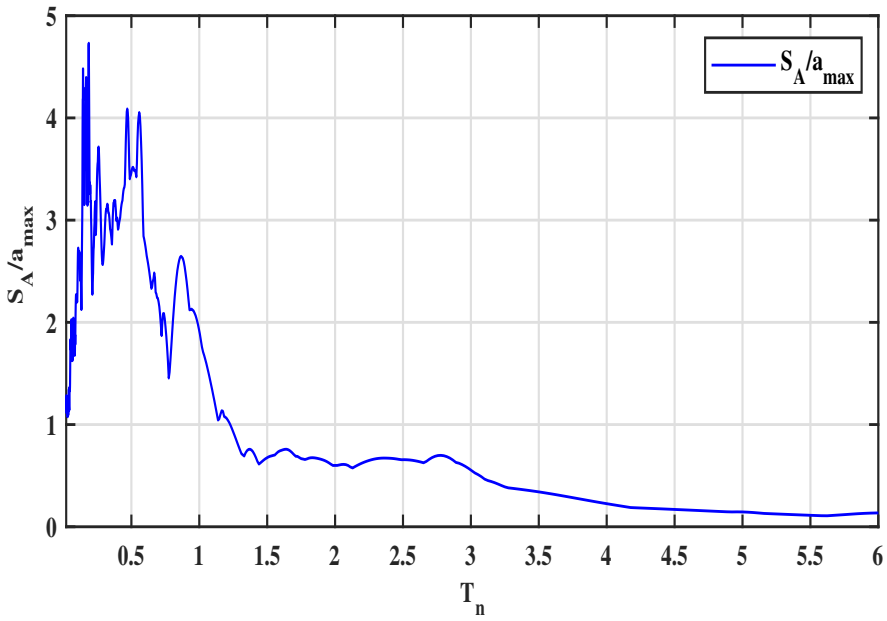

Figure 3.32. The response spectra of the El Centro earthquake

$T_b = 1.4s$ is larger than the structure's first mode period $(0,5sec)$. Accordingly, the FPBS will work as a low-pass filter that isolates the structure from the ground motion. Thus it is feasibly to be used for the 3-story structure.

For the existing structure, $\mu = 0.05$ and $R_o = 0.5m$ were taken. Then, if it is desired to calculate the damping ratio,

$$\xi_b = \frac{2\mu/\pi}{x_{bmax}/R_o + \mu},$$

$$c_b = 2\xi_b \sqrt{m_b k_b}, \tag{3.59}$$

where k_b is the instantaneous base stiffness, which depends on the base displacement.

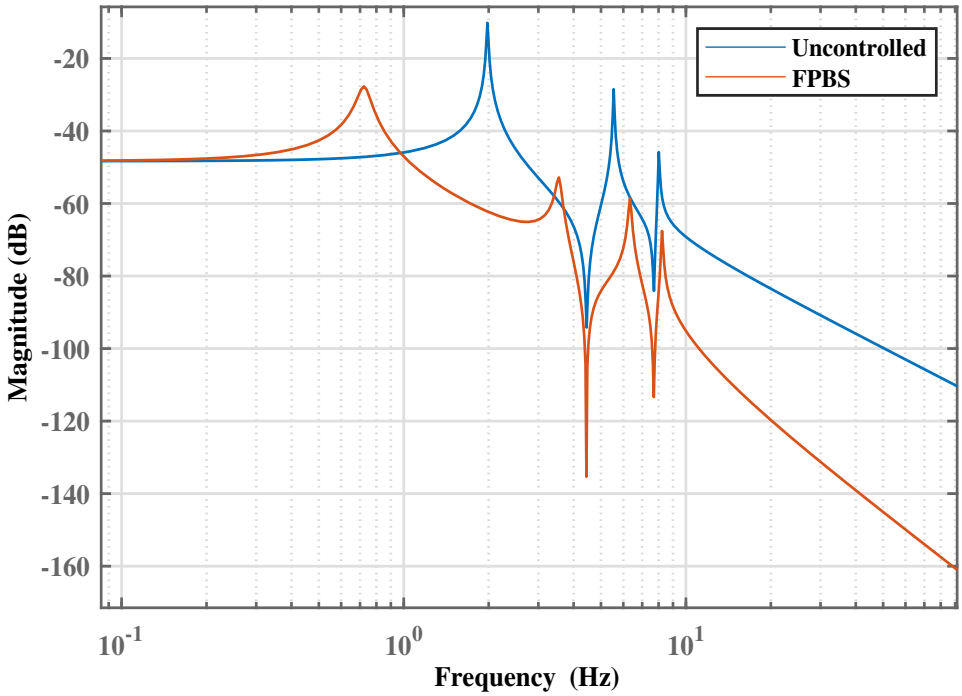

Figure 3.33. The Bode diagram of the FPBS-installed structure

Fig. 3.33 depicts the frequency-domain characteristics (Bode magnitude diagrams) for both controlled and uncontrolled structures. There is more than 10 dB decrement at the first mode frequency corresponding to the FPBS's design frequency, whereas there is more than 20 dB reduction at all modes of the superstructure. As a result, with the condition of not discussing the earthquake frequency content, the FPBS outperformed the previous controllers. Yet, this passive-controller has a disadvantage that it cannot be installed on existing structures.

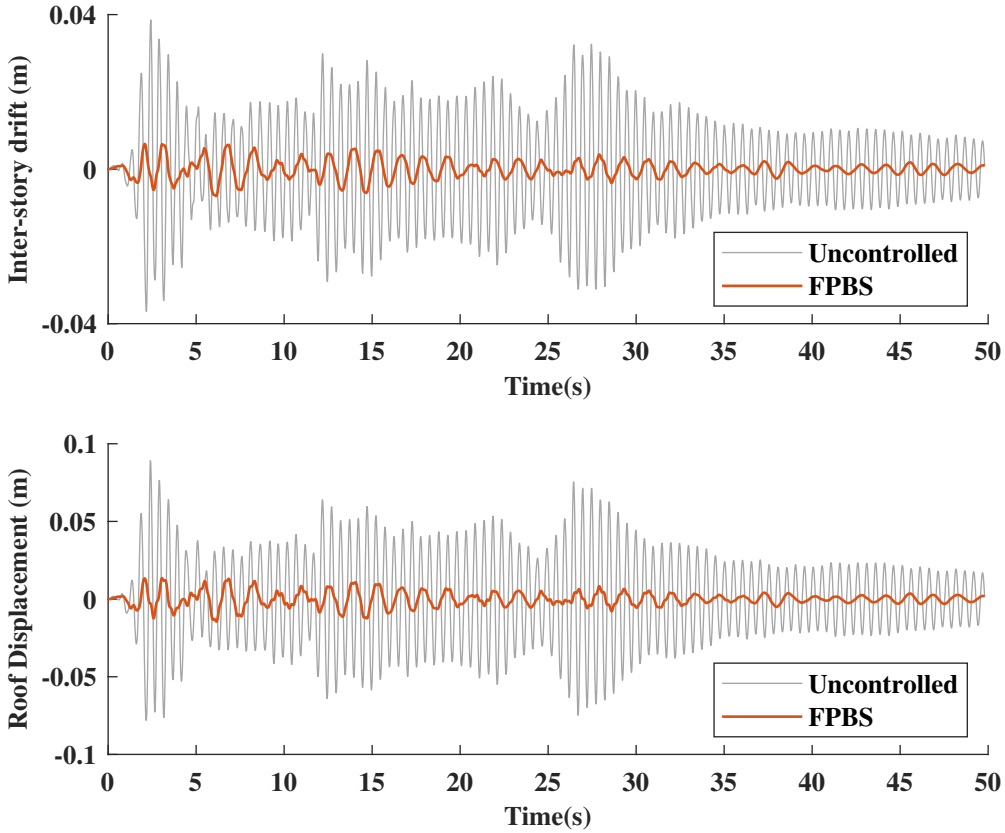

Figure 3.34. Responses of the FPBS-installed structure

The structure with the FPBS was simulated under El Centro earthquake. Fig. 3.34 shows the maximum inter-story drifts and the top story displacements. The current passive control device conduces the best results in the structural responses.

Table 3.8. Performance indices of the FPBS

	J_1	J_2	J_3	J_4	J_5	J_6	J_7	J_8
FPBS	0.1622	0.1688	0.1533	0.1792	0.1593	0.1747	0.1678	0.1750

Table 3.8 confirms that the controlled structure results in better performance than any other scenario in every index, including the J_4 and J_8 indices. The reason behind why the FPBS control strategy is better than the previous controllers is that the structure

equipped with an FPBS is no longer the same in a model characteristic manner. The FPBS causes the structure to have one additional mode. This added mode is slower than the structure fundamental mode and behaves like a low-pass filter. As a result, higher frequencies get attenuated. The structural frequency response is changed by a significant amount, as seen in Fig. 3.33.

3.3.2. Tuned Mass Damper (TMD)

A TMD is employed as a passive-control device for the current structure. In the literature, two common models with the TMD model parameters are employed within this framework. The first one was suggested by Ormondroyd (1928);

$$f = \frac{1}{1+\mu} \quad and \quad \zeta = \sqrt{\frac{3\mu}{8(1+\mu)}}, \tag{3.60}$$

where f represents the frequency ratio between the TMD and the structure, ζ represents the damping ratio of the TMD, and μ is the mass ratio. These equations are valid while the structures damping ratio, β, is zero. In other cases, the parameter values were proposed by Sadek et al. (1997), which were obtained by curve fitting techniques.

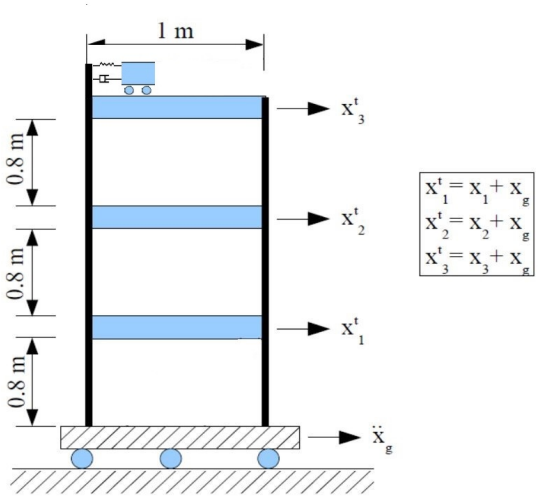

Figure 3.35. The TMD-installed structure

The below two equations are for the single degree of freedom (SDOF) structures. Yet, our models are not SDOF.

$$f = \frac{1}{1+\mu}\left[1 - \beta\sqrt{\frac{\mu}{(1+\mu)}}\right], \quad \zeta = \frac{\beta}{1+\mu} + \sqrt{\frac{\mu}{(1+\mu)}} \tag{3.61}$$

An approach that can be implemented on a multiple degree of freedom (MDOF) structure modeling should be employed. Such an approach was also proposed by Sadek et al. (1997), including the mode shapes, Φ_i.

$$\mu = \frac{m}{{\Phi_i}^T[M]\Phi_i} \quad f = \frac{1}{1+\mu\Phi_{ij}}\left[1 - \beta\sqrt{\frac{\mu\Phi_{ij}}{(1+\mu\Phi_{ij})}}\right] \; and \; \zeta = \Phi_{ij}\left[\frac{\beta}{1+\mu} + \sqrt{\frac{\mu}{(1+\mu)}}\right], \tag{3.62}$$

where Φ_i is generally implemented as the normalized fundamental modal shape (${\Phi_i}^T \cdot \Phi_i = 1$), but it may also be any other modal shape which is desired to be controlled. Φ_{ij} is the amplitude of the corresponding mode of vibration for a unit modal participation factor computed at the location of the TMD. As an alternative, Feng and Mita (1995) proposed an optimum damping ratio formulation. The formulation is given as,

$$\zeta = \frac{1}{2}\sqrt{\frac{\mu(1-\mu/4)}{(1+\mu)(\mu/2)}}, \tag{3.63}$$

and the damping coefficients for all the proposed TMD models above are calculated by

$$c_i = 2\zeta m_i \omega_i. \tag{3.64}$$

The model parameters for the 3-story structure are given as follows,

$$M_s = \begin{bmatrix} 200 & 0 & 0 & 0 \\ 0 & 200 & 0 & 0 \\ 0 & 0 & 200 & 0 \\ 0 & 0 & 0 & 30 \end{bmatrix},$$

$$K_s = 1e5 \begin{bmatrix} 3.1250 & -1.5625 & 0 & 0 \\ -1.5625 & 3.1250 & -1.5625 & 0 \\ 0 & -1.5625 & 1.5816 & -0.0191 \\ 0 & 0 & -0.0191 & 0.0191 \end{bmatrix},$$

$$C_s = \begin{bmatrix} 61.7600 & -18.2000 & 0 & 0 \\ -18.2000 & 61.0200 & -18.2000 & 0 \\ 0 & -18.2000 & 176.3215 & -133.6215 \\ 0 & 0 & -133.6215 & 133.6215 \end{bmatrix}.$$

The structure with the TMD simulation was undertaken. Fig. 3.36 shows the maximum inter-story drifts and the top story displacements. The current passive control device yields better results compared to the uncontrolled structure in the structural responses. On the other hand, its performance is not as promising as the FPBS.

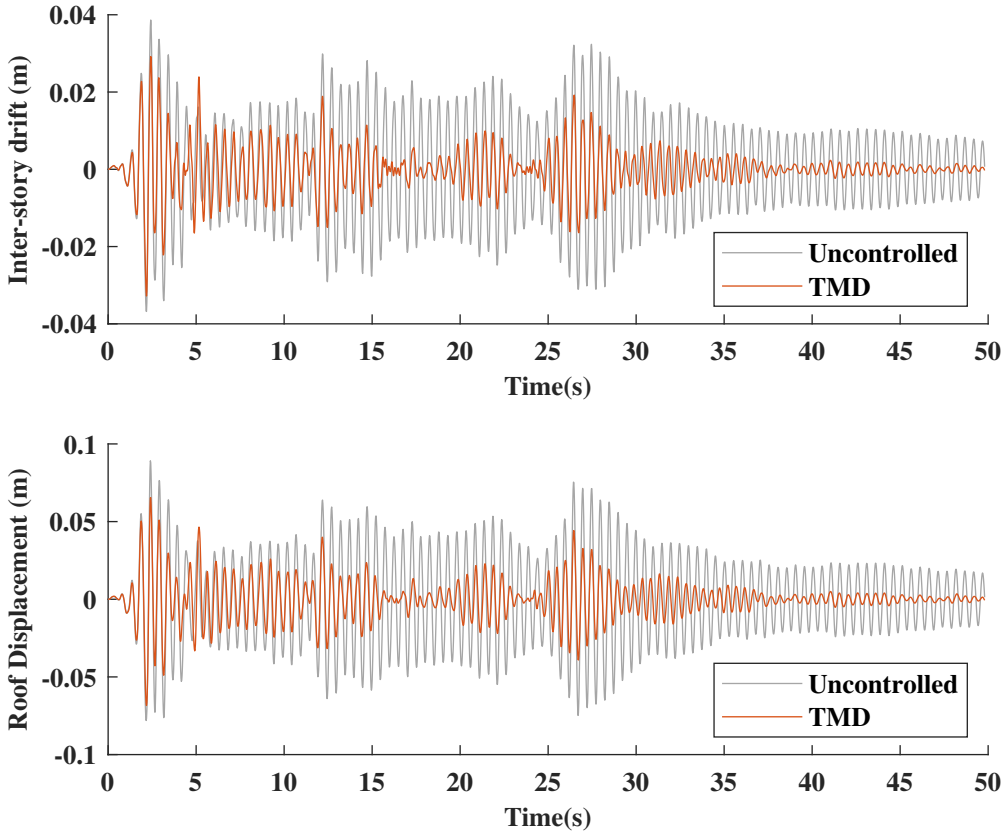

Figure 3.36. Responses of the TMD-installed structure

The performance difference can be diminished by increasing the mass ratio of the TMD. (It was taken 0.05 according to the Ormondroyd (1928) formula, and 0.15 according to the Sadek et al. (1997) formulae for the current structure.) This method does not always guarantee a better result because of the implementation issues. Contrarily, the FPBS is not a solution for the structures that already exist.

Table 3.9 confirms that the controlled structure results in better performance than the uncontrolled structure in every index. The performance values are similar to the structure with the 0V-driven MRD located at the first floor in Table 3.3.

Table 3.9. Performance indices of the TMD

	J_1	J_2	J_3	J_4	J_5	J_6	J_7	J_8
TMD	0.7674	0.7553	0.7188	0.8286	0.4545	0.4583	0.7870	0.4646

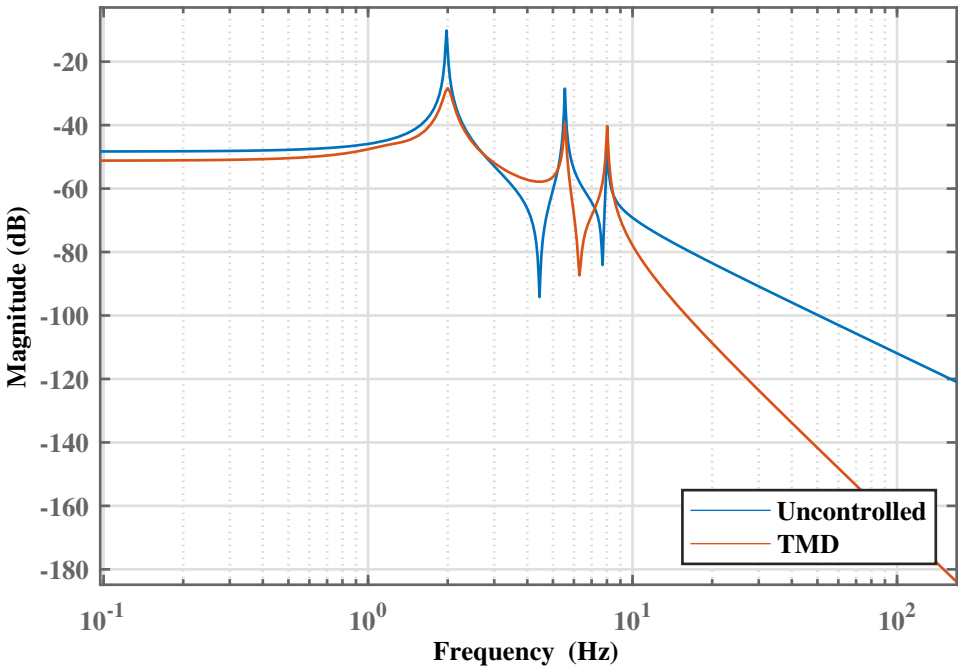

Figure 3.37. The Bode diagram of the TMD-installed structure

Fig. 3.37 depicts the frequency-domain characteristics for both structures; controlled and uncontrolled. The TMD decreases the frequency response amplitudes of the modes by more more than $10dB$. The fundamental frequency is shifted slightly to right,

and the TMD induced first mode of the total structure is hard to depict around $1.1Hz$. Due to the induced damping of the TMD, the zero point in between the first and the second modal responses is increased by a significant amount.

As a worst-case scenario, the TMD mass is considered to be stuck such that it cannot move. In this case, the top floor mass is regarded a summation of both the TMD and the top floor. Accordingly, the previous simulation is repeated and the results are shown in Fig. 3.38.

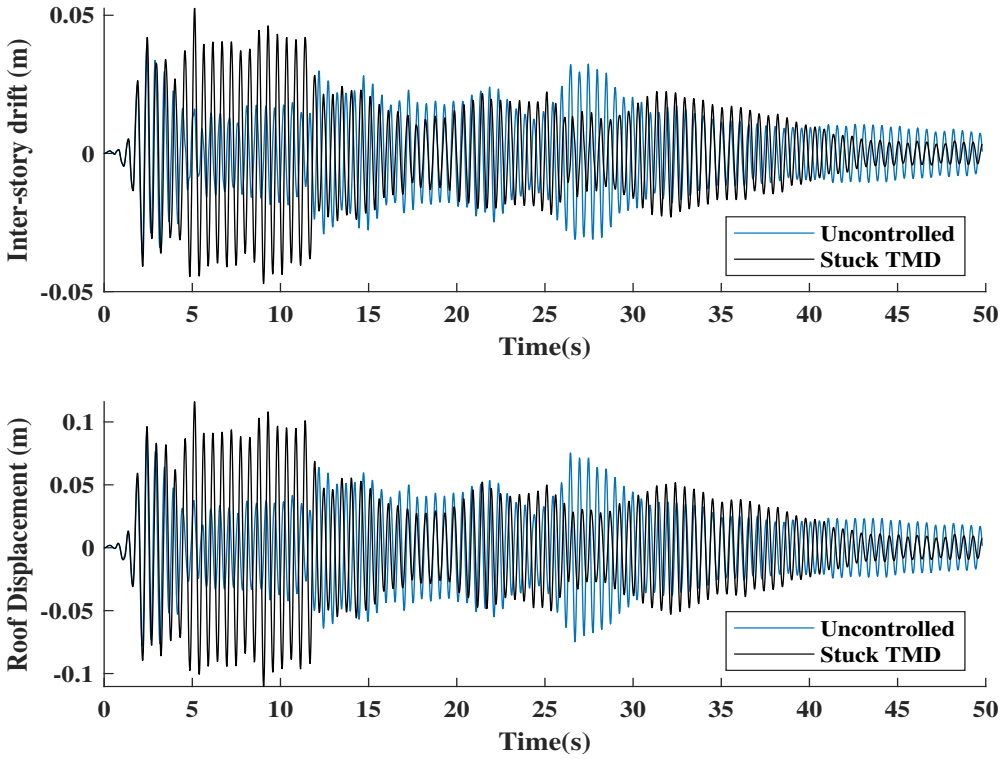

Figure 3.38. The structure equipped with a stuck TMD responses

The stuck TMD worsens the structural response and the performance indices are represented in Table 3.10. As can be seen, all performance indices are larger than 1. As a designer, the TMD mass ratio should be limited by considering this worst-case scenario.

Table 3.10. Performance indices of the stuck TMD

	J_1	J_2	J_3	J_4	J_5	J_6	J_7	J_8
Stuck-TMD	1.3021	1.3589	1.1970	1.2828	1.2803	1.2480	1.2312	1.1697

3.4. Hybrid Controllers

In this section, two-hybrid controllers, one composed of an FPBS and an MRD, and one composed of a TMD and an MRD, will be employed for the current structure. Thereafter, the results to be obtained will be compared to the uncontrolled and the single device-controlled structure responses.

3.4.1. FPBS+MRD/Actuator

In using a hybrid controller, there are many advantages, such as consuming less energy and having an occasion that satisfies the wider frequency bandwidth. In this particular controller, the FPBS decreases the structure's fundamental modal frequency, whereas the MRD/Actuator reduces the amplitudes of all modes. Consequently, both form a controller that work in union within a broader bandwidth.

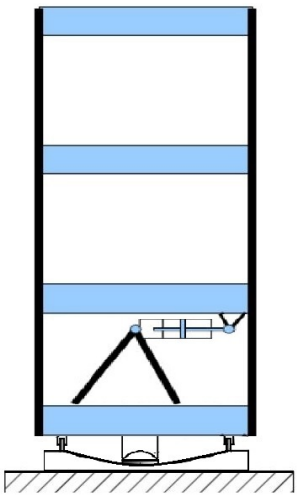

Figure 3.39. The structure equipped with both an MRD and an FPBS

As depicted in Fig. 3.39, the FPBS and the MRD are the same devices employed in the study's earlier stage. The modal parameters of the structure are already given in the FPBS part. Besides the control input location vector, Γ_c, is updated as follows:

$$\Gamma_c = \begin{bmatrix} 0 \\ 0 \\ 1 \\ -1 \end{bmatrix}. \tag{3.65}$$

The structure equipped with the H_∞-hybrid controller is simulated under the El Centro ground motion. Fig. 3.40 shows the maximum inter-story drifts and the top story displacements. Apparently, the hybrid control fades away the vibrations thanks to the active control force being part of the hybrid controller.

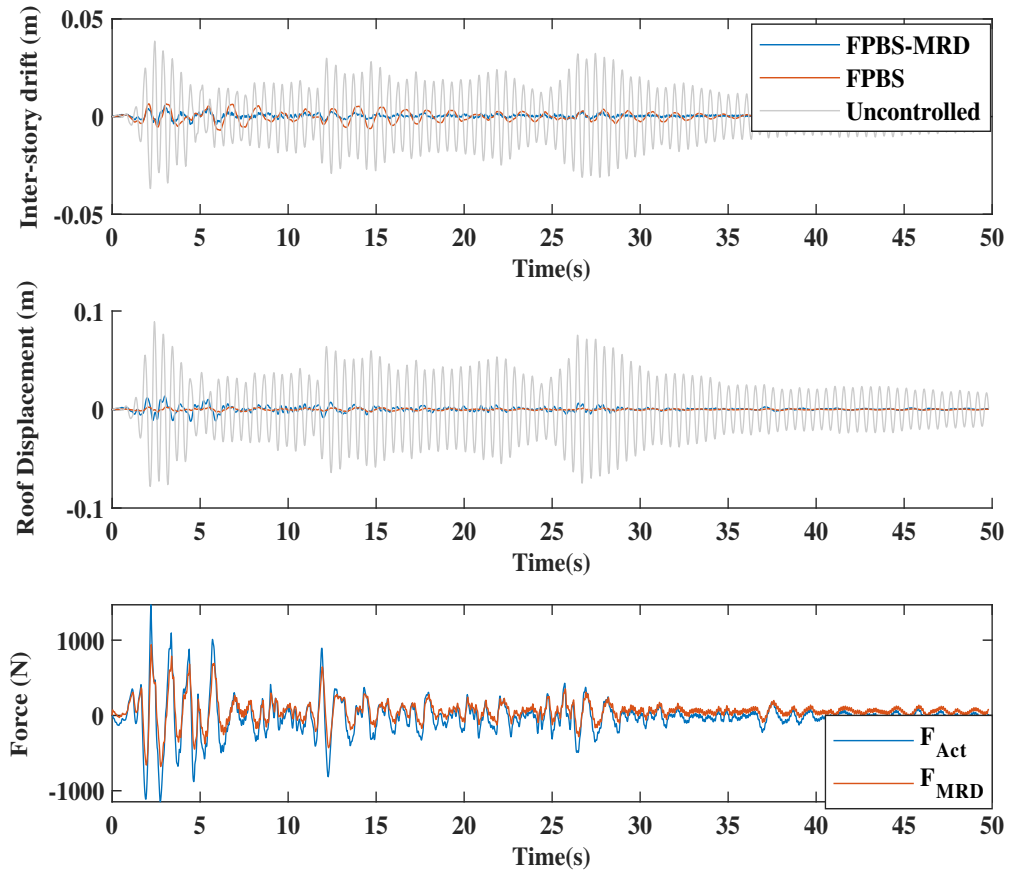

Figure 3.40. Responses of the FPBS+MRD-installed structure

Table 3.11 shows the controlled structure performance indices. These given results are akin to the structure having mere FPBS and there is a small increment in J_4 because of the additional MRD force.

Table 3.11. Performance indices of the FPBS+MRD

	J_1	J_2	J_3	J_4	J_5	J_6	J_7	J_8
FPBS	0.1622	0.1688	0.1533	0.1792	0.1593	0.1747	0.1678	0.1750
FPBS+MRD	0.1534	0.1468	0.2041	0.2000	0.0927	0.0945	0.1906	0.1267

According to Fig. 3.41, the additional MRD effect results in a $20dB$ decrement at the first mode frequency of the structure installed mere FPBS. In contrast, there are upthrusts in between the higher modes of the superstructure's frequency responses. In summary, the formed hybrid controller enhances the performance, where the passive controller is not effective.

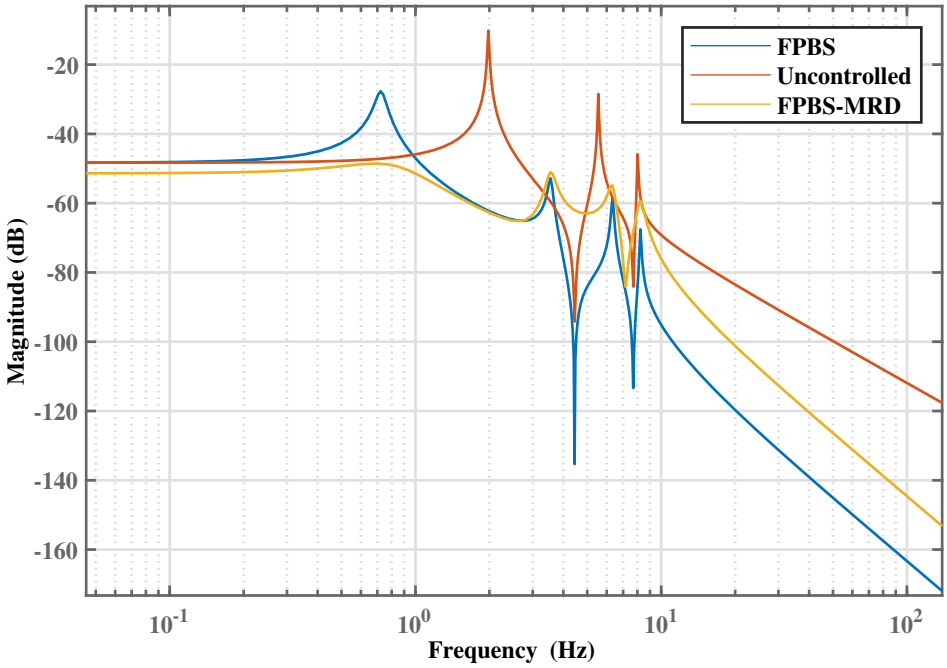

Figure 3.41. The Bode diagram of FPBS+MRD/Actuator-installed structure

3.4.2. TMD+MRD/Actuator

The performance of the TMD can be improved by an additional MRD/Actuator controller as shown in Fig. 3.42.

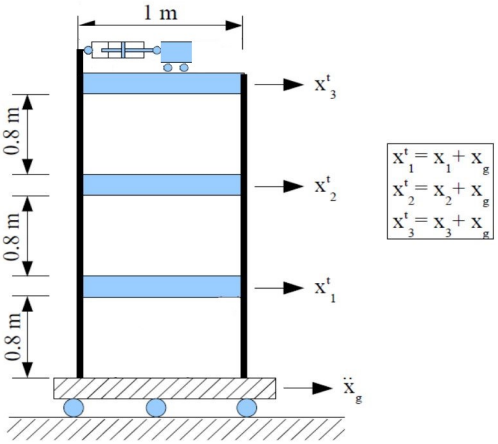

Figure 3.42. The TMD+MRD-installed structure

It is a hybrid model in which an MRD is connected serially to a TMD. The main idea of this proposal is that TMD can work as a passive damper in a specific frequency region, while MRD can tune the TMD concerning uncertainties that will be handled as the study continues.

The H_∞ control algorithm was chosen because it conduced the best results among all applied active/semi-active controllers. As a controller, it aims to regulate the dominant modes. At the same time, the less dominant modes have less contribution to the total response, and therefore, they are disregarded.

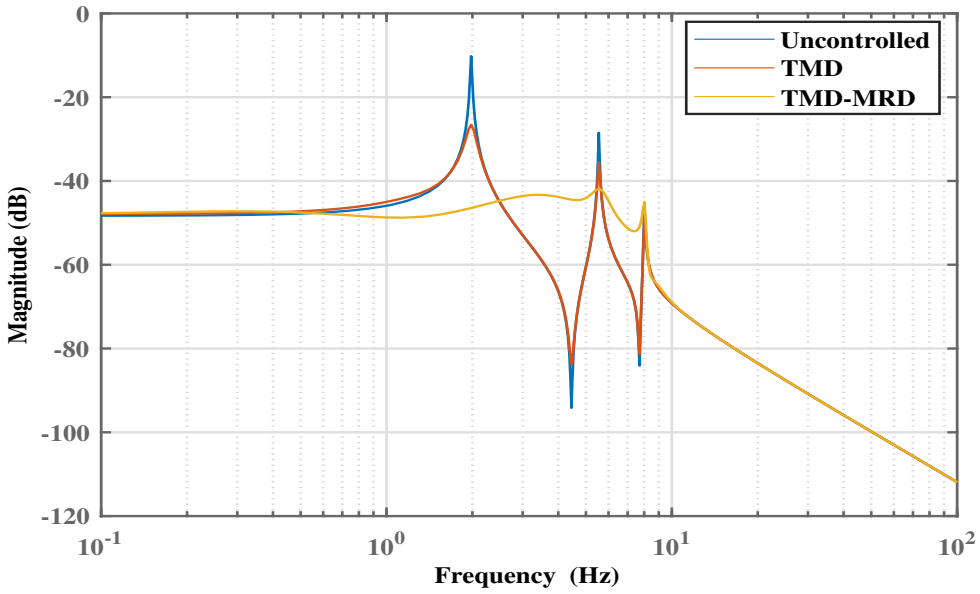

Figure 3.43. The Bode diagram of the TMD+MRD/Actuator-installed structure

In Fig. 3.43, it can be seen how MRD/Actuator installation affects the 3-story civil structure frequency response. MRD pulls down the first and the second modal peaks while it increases the bandwidth response between the modal frequency values.

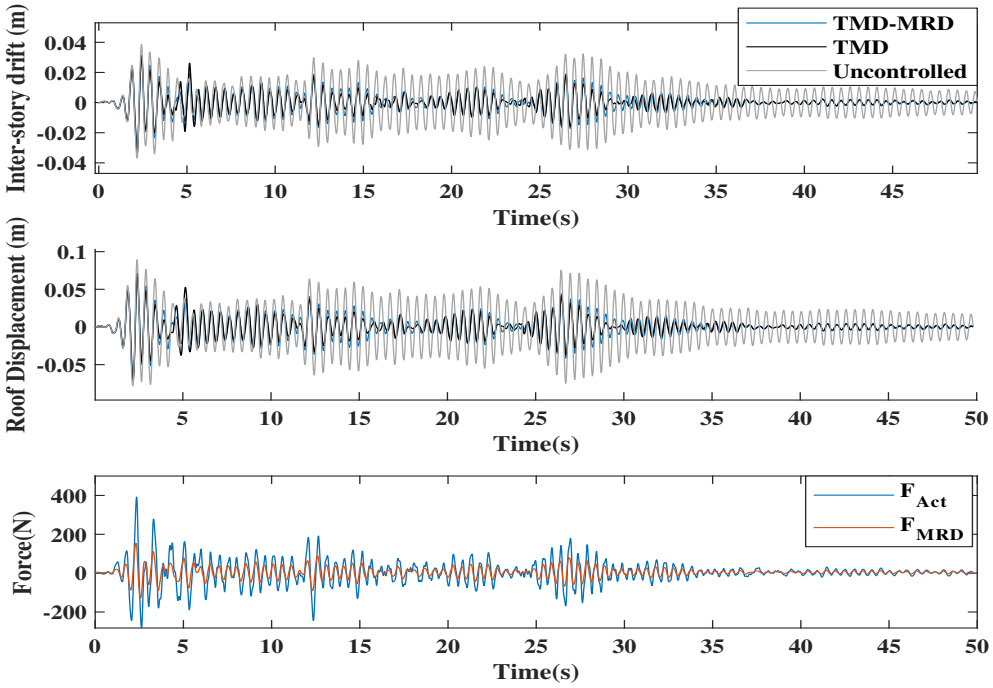

Figure 3.44. Responses of the TMD+MRD/Actuator-installed structure

The roof displacements and maximum inter-story drifts of the 3-story structure are given in Fig. 3.44. According to Table 3.12, the indices J_1 and J_5 are equivalent to 0.7543 and 0.4807, respectively. It can be said that the hybrid controller is of slightly better performance in decreasing the roof displacements than the mere TMD installed structure performance. It should be noted that since the internal dynamics have an offset force value and it is larger than the required control force, the employed MRD is scaled down to $1/10$.

Table 3.12. Performance indices of the TMD+MRD

	J_1	J_2	J_3	J_4	J_5	J_6	J_7	J_8
TMD	0.7674	0.7553	0.7188	0.8286	0.4545	0.4583	0.7870	0.4646
TMD-stuck	1.3021	1.3589	1.1970	1.2828	1.2803	1.2480	1.2312	1.1697
TMD+MRD	0.7543	0.7532	0.7358	0.7855	0.4807	0.4839	0.7806	0.4906

3.4.3. General Comments on Applied Controllers

The performance indices of all the controllers are given in Table 3.13. Among all the implemented active/semi-active controllers, we observe that H_∞ controller results in slightly better performance.

As seen in Table 3.13, the active/semi-active controllers performed well and improved the earthquake performance of the 3-story structure. The FPBS-installed structure outperformed all the controllers. However, the physical implementation of the FPBS is relatively complex, especially for the already existing structure. For an easy implementation, TMDs can be chosen. When looking at the frequency characteristics of the passive controllers (FPBS), they act like low-pass filters. Especially in some frequency bandwidths, their addition may worsen the responses. For robust performances, hybrid controllers can be employed.

Table 3.13. Performance indices of all controllers

	J_1	J_2	J_3	J_4	J_5	J_6	J_7	J_8
Uncontrolled	1.0000	1.0000	1.0000	1.0000	1.0000	1.0000	1.0000	1.0000
LQR	0.6606	0.6547	0.6707	0.7905	0.3971	0.3452	0.7594	0.4259
LQR-0V	0.7486	0.7399	0.6539	0.8096	0.4255	0.4051	0.7839	0.4378
PDD	0.7020	0.6584	0.8127	0.8127	0.4226	0.4020	0.7883	0.4417
PP	0.6944	0.7053	0.6560	0.8081	0.4162	0.4036	0.7778	0.4226
H_∞	0.6447	0.6205	0.7434	0.7550	0.3836	0.3556	0.7407	0.4053
H_2	0.6645	0.6404	0.6400	0.7552	0.3796	0.3536	0.7342	0.3953
FPBS	0.1622	0.1688	0.1533	0.1792	0.1593	0.1747	0.1678	0.1750
TMD	0.7674	0.7553	0.7188	0.8286	0.4545	0.4583	0.7870	0.4646
TMD-stuck	1.3021	1.3589	1.1970	1.2828	1.2803	1.2480	1.2312	1.1697
FPBS+MRD	0.1534	0.1468	0.2041	0.2000	0.0927	0.0945	0.1906	0.1267
TMD+MRD	0.7543	0.7532	0.7358	0.7855	0.4807	0.4839	0.7806	0.4906

Another outcome that should be considered is the uncertainties. Up to now, we assumed that the structure is nominal and linear. However, in reality, there is no such case. For instance, in the stuck-TMD application, the performance of the structure became deteriorated because of the mass change at the top floor where the TMD got stuck. It can be classified as mass uncertainty in the system. Likewise, the performances of the passive controllers are highly sensitive to model parameters of the structure. For this reason, in the next chapter, the uncertainties in the model are considered and a robust control technique is designed to solve this problem.

CHAPTER 4

LINEAR ROBUST CONTROLLER

Civil structures can be modeled as second-order differential equations. However, due to the modeling and/or nonlinearity effects, it may not fully represent the physical systems and their behaviors. Hence, uncertainties should be considered in modeling so that the simulation behaviors cover the physical responses. Kar et al. (2000) studied the topic of the robust control method with models having uncertainties in system and control input matrices. Moreover, a robust controller based on state-feedback control was designed by Wang (2003). As an observer, he equipped his controller with a modified Kalman filter. Nevertheless, the parametric uncertainties were implemented as a linear increase of state-space representation matrices. Thus, uncertainties cannot be recognized whether those exist in inertia, damping, or stiffness model matrices.

In developing a mathematical model of a real structure, the simulation results may not match the real structural response. This matter is a general problem that arises during the structure's dynamic motion, which may be modeled by means of parameter variations in the stiffness, damping, and mass matrices. These changes in parameters need to be estimated within a bandwidth, and the mathematical model is updated to obtain higher control performances and robustness.

Huo et al. (2016) modeled these uncertainties as distinguishable with reasonable percentages. Thanks to the work of Zhou and Doyle (1998), upper linear fractional transformation (LFT) can be implemented to civil structures uncertainties. In this part of the study, an MRD device is applied to stabilize the civil structure. Parametric uncertainties are used for mass, stiffness, and damping matrices.

4.1. Uncertain Structure Model

Every mathematical model is an approximation of the true system. These models have always unmodeled effects such as neglected nonlinearity, deliberately truncated number of modes and variations in system parameters owing to environmental fluctuations.

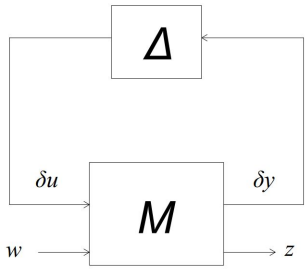

Figure 4.1. Standard M-Δ Configuration

These differences could adversely affect controller performance. In order to investigate uncertainty within the civil structure, the model is converted to state space representation. Subsequently, the relation of the uncertainty effect to the mathematical model is constructed. Fig. 4.1 shows the input-output relations of the 3-story building structure and its uncertainties. They are represented as two different systems. Here, w stands for the exogenous input which includes earthquake disturbance, measurement noise, and control input. z denotes the exogenous output to be controlled, which are selected as inter-story drifts and the control input. δu and δy are the input vector and output vector of uncertainties. The relation between δ_u and δ_y is

$$\delta_u = \Delta\delta_y. \tag{4.1}$$

The relation between the inputs and the outputs yields:

$$\begin{bmatrix} \delta_y \\ z \end{bmatrix} = \begin{bmatrix} M \end{bmatrix} \begin{bmatrix} \delta_u \\ w \end{bmatrix}, \tag{4.2}$$

where M can be represented by subsystems,

$$M = \begin{bmatrix} M_{11} & M_{12} \\ M_{21} & M_{22} \end{bmatrix}. \tag{4.3}$$

The transfer function of exogenous input to exogenous output can be written as follows,

$$z = F_U(M, \Delta)w \tag{4.4}$$

Here, $F_U(M, \Delta)$ is the Linear Fractional Transformation (LFT), which can be derived as follows

$$F_U(M, \Delta) = M_{22} + M_{21}\Delta(I - M_{11}\Delta)^{-1}M_{12}. \tag{4.5}$$

In a real civil structure, the model parameters of M_s, C_s, and K_s are not accurately known. What we can assume is that their actual values are varying with known intervals around nominal values.

$$\begin{aligned} M_s &= \bar{M}_s + P_M\delta_M\bar{M}_s = (I + P_M\delta_M)\bar{M}_s, \\ C_s &= \bar{C}_s + P_C\delta_C\bar{C}_s = (I + P_C\delta_C)\bar{C}_s, \\ K_s &= \bar{K}_s + P_K\delta_K\bar{K}_s = (I + P_K\delta_K)\bar{K}_s, \end{aligned} \tag{4.6}$$

where $\bar{M}_s$, $\bar{C}_s$, and $\bar{K}_s$ represent nominal values of M_s, C_s, and K_s. The possible perturbations are δ_M, δ_C, and δ_K on model parameters. Further, P_M, P_C, and P_K represent the maximum ratio of differences between the real structure and the mathematical model. The matrices δ_M, δ_C and δ_K typically are diagonal matrices with uncertain varying values bounded within the range of $[-1, 1]$. These types of uncertainties are named structured uncertainties since they have zero off-diagonal elements. A brief description of the structured and the unstructured uncertainties was done by Zhou and Kimura (1994). We note that M_s, C_s, and K_s could be represented as an LFT in δ_M, δ_C, and δ_K, respectively. Similar to the representation of the building model upper LFT, given in Eq. 4.6, M_M, M_C, and M_K are represented;

$$M_M = \begin{bmatrix} P_M & I \\ -\bar{M_s}^{-1}P_M & \bar{M_s}^{-1} \end{bmatrix}, \qquad M_C = \begin{bmatrix} 0 & \bar{C}_s \\ P_C & \bar{C}_s \end{bmatrix}, \quad M_K = \begin{bmatrix} 0 & \bar{K}_s \\ P_K & \bar{K}_s \end{bmatrix}. \tag{4.7}$$

These matrices can be illustrated by standard $M - \Delta$ representation as shown in Fig. 4.2. It is noteworthy that M_M is given in the inverse form of M_s since it will be employed in that scheme while constructing the overall structural dynamics.

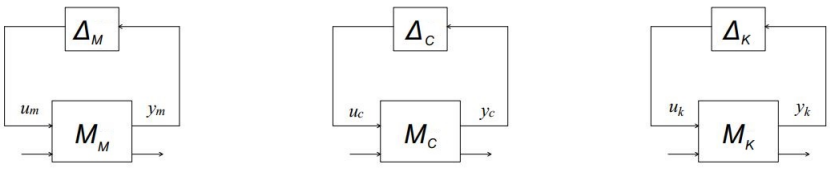

Figure 4.2. Representation of uncertainties as LFT

The uncertainties Δ_M, Δ_C and Δ_K shown in the block diagrams in Fig. 4.2 depict the inputs and outputs of δ_M, δ_C and δ_K as δu, and δy as shown in Fig. 4.3.

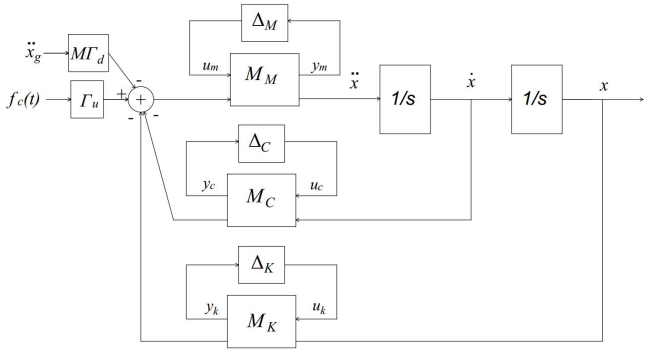

Figure 4.3. Block diagram of the controlled civil structure system with uncertainties

Let the states be $\begin{bmatrix} x \\ \dot{x} \end{bmatrix}$ and the measurement y be the story displacements of the structure and earthquake excitation $\ddot{x}_g$. The general state-space relation for Fig. 4.3 can be constructed as;

$$\begin{bmatrix} \dot{x} \\ \ddot{x} \\ \cdots \\ \delta y \\ \cdots \\ y \end{bmatrix} = \begin{bmatrix} A & \vdots & B_1 & B_2 \\ \cdots & \cdots & \cdots & \cdots \\ C_1 & \vdots & D_{11} & D_{12} \\ C_2 & \vdots & D_{21} & D_{22} \end{bmatrix} \begin{bmatrix} x \\ \dot{x} \\ \cdots \\ \delta u \\ \cdots \\ \ddot{x}_g \\ u \end{bmatrix}, \tag{4.8}$$

where

$$A = \begin{bmatrix} 0 & I \\ -\bar{M}_s^{-1}\bar{K}_s & -\bar{M}_s^{-1}\bar{C}_s \end{bmatrix},$$

$$B_1 = \begin{bmatrix} 0 & 0 & 0 \\ -\bar{M}_s^{-1}P_M & -\bar{M}_s^{-1}P_C & -\bar{M}_s^{-1}P_K \end{bmatrix},$$

$$B_2 = \begin{bmatrix} 0 & 0 \\ -\Gamma_d & \bar{M}_s^{-1}\Gamma_u \end{bmatrix}, \tag{4.9}$$

and C_1 , C_2, D_{11}, D_{12}, D_{21}, and D_{22} can be constructed according to measurements and exogenous outputs.

The input/output dynamics that take into account the uncertainty of the system parameters can be indicated by M, as shown in Fig. 4.4, housing all uncertainties and perturbations.

Figure 4.4. Input/output block diagram of the system

4.2. Generalized Structure Plant

The computation of an optimal robust controller for the structural system is transformed into a generalized control plant frame in Fig.4.5. Here, P stands for the plant(the structure) including the weights, and K is the achieved controller in the figure. In order to adjust the plant performance, weighting functions are used (Gu et al. (2005)). As it is known, there are many advantages in using weighting functions, such as eliminating measurement unit differences and/or rejecting errors which are expected to occur in certain frequency ranges.

A block diagram representation of the civil structure system is represented in Fig.4.6. The Tajimi Spectrum, W_g, and the noise input filter, W_n, are introduced in the H_∞-controller part. Similarly, the performance and control weights, W_p and W_u, are employed as given in the same part.

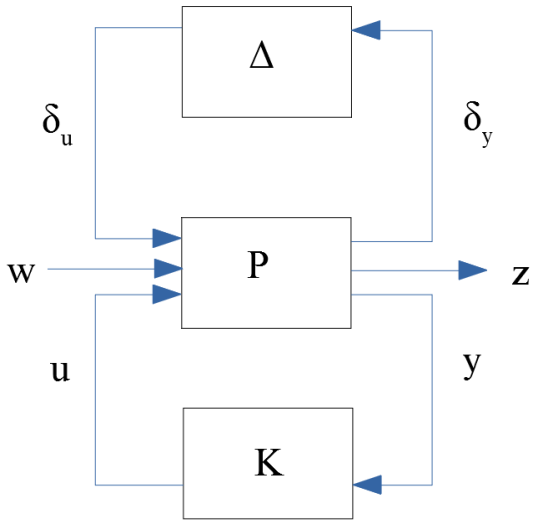

Figure 4.5. General structure plant configuration including uncertainties

Different control strategies can be utilized in order to find the control forces required for enhanced structural behavior. In the control algorithm, the stabilizing control forces that also optimize a preferred cost function are determined.

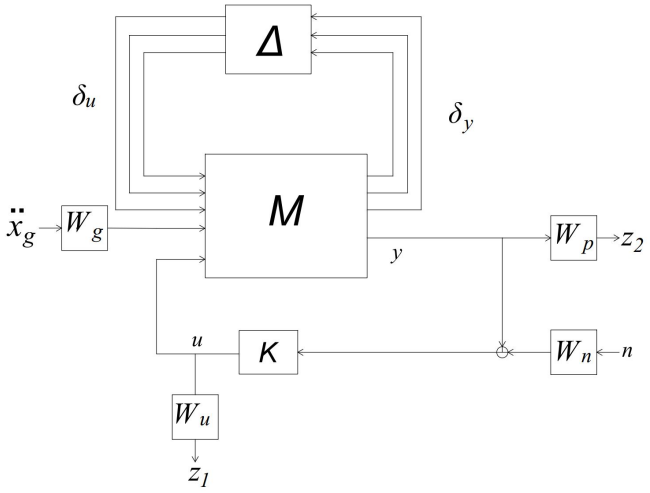

Figure 4.6. Control block diagram for a seismically excited civil structure

4.2.1. Robustness for Stability

Robust stability analysis is a tool that shows how much uncertainty exists in the system and how far the system resides from the instability limits. In other words, it shows the stability margins for the system having uncertainty.

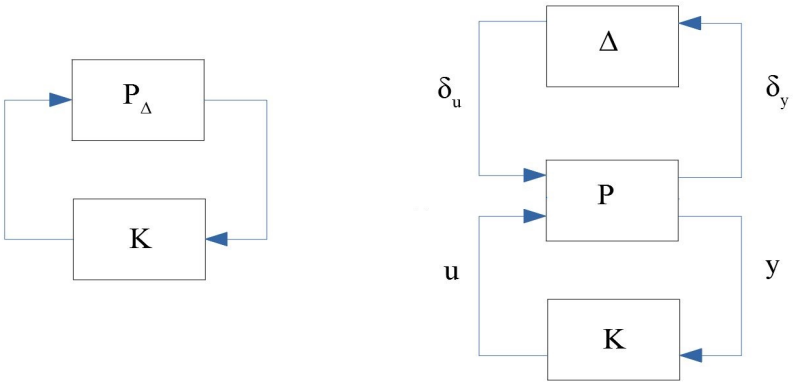

Figure 4.7. Robust stability

In Fig.4.7, the structure including uncertainties is depicted by P_Δ and the K is the controller. P_Δ can be split into the nominal plant P and the structured uncertainty block Δ.

Robustness for stability can be summarized as the stability of the $P-\Delta$ connection by the following inequality,

$$\|F_L(P,K)\|_\infty < \gamma, \quad \gamma > 0, \quad \gamma \in \mathbb{R}, \tag{4.10}$$

where K represents a controller such that satisfies the condition of Eq. 4.10. The system is stable for all $\|\Delta\|_\infty < 1/\gamma$ (Skogestad and Postlethwaite (2007)). The cost function of the study is to minimize the introduced γ value. The small gain approach is not easy to implement to achieve a proper controller since it is highly conservative and does not consider the diagonal block pattern of the uncertainties Δ. Therefore, the controller based on the small gain theorem may lose some control ability to provide stability. In the application of the control theory, structures do not have stability issues since they are fixed against rigid body motions. However, we may represent their stability margins and interpret how close to instability they are.

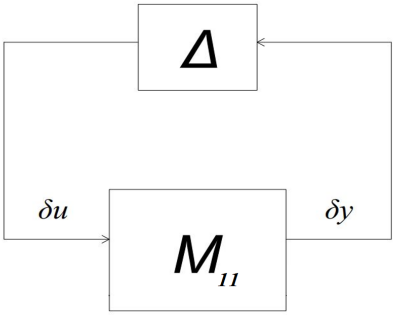

Figure 4.8. Robust stability analysis via the upper LFT

Through upper LFT, the robust stability for the civil structure is depicted in Fig.4.8, where the structure model without weights, M, is employed. After upper LFT implementation, the structure closed-loop system between the structure and uncertainties, M_{11}, is achieved, and its stability for robustness is examined.

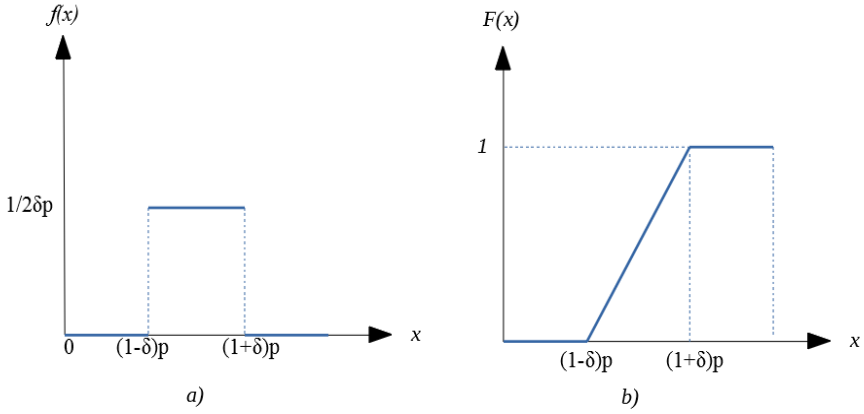

Figure 4.9. a) Probability density function of the parameters, b) Cumulative distribution function

In this study, the uncertainty ratios are assumed as 20%, for mass and stiffness (P_M, P_K) and 60% for damping matrix, P_C. These uncertainties are represented as uniform distribution as shown in Fig.4.9, where p represents the modal parameters: mass, stiffness, and damping. In the range of uncertainties, any parameter value possibility of occurrence is equal because in robust control technique, we would like determine the ranges but not how they distributed are. The uniform distribution is a common approach and validated by many scholars in robust control implementations (Calafiore et al. (2013)). Accordingly,

the uncertainty block infinity norm cannot be larger than 1, and the possible perturbed structures and the worst-case perturbation can be calculated.

The robust stability margin is the reciprocal of the singular values of the $\|F_U(M_{11}, \Delta)\|$, μ. Therefore upper bounds from the structured uncertainty matrix become lower bounds on the robust stability margin. We need to make these conversions and find the destabilizing frequency where the μ upper bound peaks. It should be noted that frequency is where the robust stability margin is smallest.

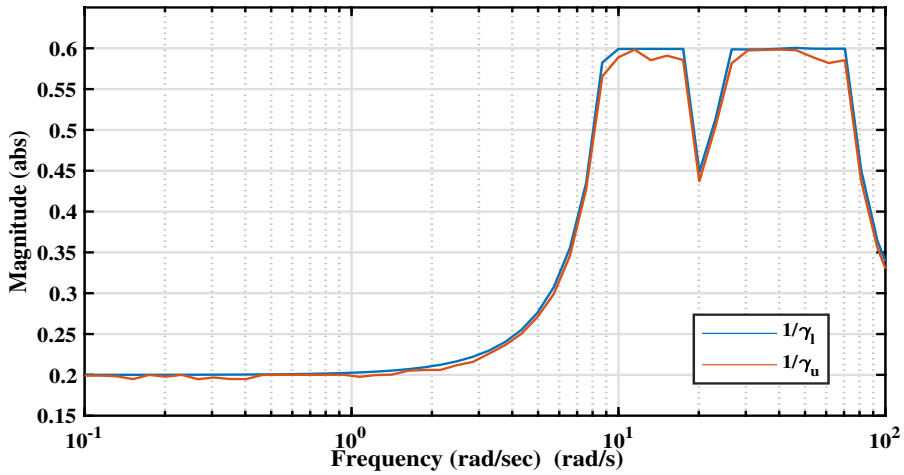

Figure 4.10. μ-values which represents the robust stability

Fig. 4.10 shows the inverse-scale upper and lower bound of structured uncertainty matrix, Δ. According to the figure, the robust stability margin can be deduced for desired frequency range. As seen, the upper and lower bounds are around 0.2 under $1 rad/sec$, which means that the stability margin is $1/0.2 = 5$ and therefore, an uncertainty ratio of 400% is expected to be manageable below $1 rad/sec$. For the bandwidth between 10 and $100 rad/sec$, these reciprocal values go down to $1,33(1/0.6)$, and the uncertainties in this region can be increased by 33%. If the uncertainties are actually larger than these values, the controller may cause the structure to become unstable.

On the contrary, if the structure closed-loop γ value is smaller than 1, we can guarantee that the proposed system is robustly stable.

4.2.2. Robust Performance

Robust performance means that the performance objective can be satisfied under all disturbances and noises for all possible civil structure systems in the uncertainty set. To achieve robust performance, a method called μ-synthesis is employed.

4.2.3. $\mu-$ synthesis & DK-iteration

As known, the infinity norm of the uncertainty matrix, Δ is always smaller than 1. However, depending on the uncertainty characteristics, the infinity norm of the remaining system that uncertainty are pulled-out, M, can be bigger than 1.

Accordingly, to achieve a better controller, the D-K iteration approach is employed. D is an artificial system matrix that is introduced into the uncertainty block. In addition, the inverse of the system D is also applied to the input uncertainty block. The norm of the overall system remains unchanged. At the same time, the norm of the system matrix is decreased. As a result, a satisfactory controller can be achieved. The method iterates between solving an upper bound μ analysis problem and control design via H_∞ optimization techniques.

$$\max \rho(M) \quad \leq \quad \mu(M) \quad \leq \quad \inf_{D} \ \bar{\sigma}(DMD^{-1}) \tag{4.11}$$

In Eq. 4.11, the lower bound is equity, but it is difficult to compute since it is not convex (difficult to find the global maximum). The upper bound is relatively easy to find (convex). For this reason, the upper bound is employed to stay on the safe side even if it means lower robustness.

An example can summarize this method. In this example, let $G_1(jw)$ and $G_2(jw)$ be the two different scaled matrices,

$$\begin{aligned} G_1(jw) &= 0.5\begin{bmatrix} 1 & 1 \\ 1 & 1 \end{bmatrix}, \qquad \|G_1\|_\infty = 1 \\ G_2(jw) &= 0.5\begin{bmatrix} 1 & 10 \\ 0.1 & 1 \end{bmatrix}, \qquad \|G_2\|_\infty = 5.5 \end{aligned} \tag{4.12}$$

These matrices become equivalent if we implement the upper LFT $\|F_U(G,\delta)\|_\infty$ as given in the following figure:

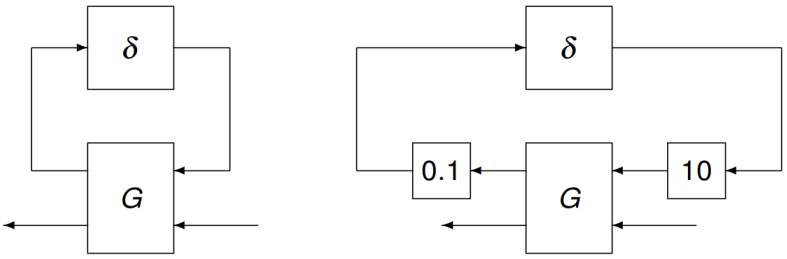

Figure 4.11. D Scaling example

$$\|F_U(G_1,\delta)\|_\infty = \|F_U(G_2,\delta)\|_\infty \tag{4.13}$$

At last, D scaling does not change the norm of the system matrices having uncertainties. It only manipulates the norm of the separated matrices in which the control performance depends on the norm of the system remitted from uncertainties.

In Fig. 4.12, the small-signal analysis was introduced. D-K iteration theory is based on this small-signal analysis. The procedure followed in the D-K algorithm is that a proper controller is calculated by H_∞ controller, which combines the DK iteration and μ-synthesis. Then, D scaling is chosen to minimize the infinity norm of the generalized M structure. This iteration is done until that the infinity norm of M becomes smaller than 1 (Skogestad and Postlethwaite (2007)).

The structured singular value μ is a powerful tool for the analysis of robust performance with a defined controller. Yet, one may also seek to find the controller that minimizes a defined μ-condition: the μ-synthesis problem (Packard (1989)).

$$\mu\Delta\left(F_L(P,K)\right) = \frac{1}{\min\left\{\bar{\sigma}\left(\Delta\right)\left|\det\left(\mathbf{I} - F_L(P,K)\Delta\right) = 0\right.\right\}}, \tag{4.14}$$

where $\bar{\sigma}\left(\Delta\right)$ corresponds to the Δ's largest singular value; *det* stands for the abbreviation of determinant. The expression of $\det\left(\mathbf{I} - F_L(P,K)\Delta\right) = 0$ means that Δ, the un-

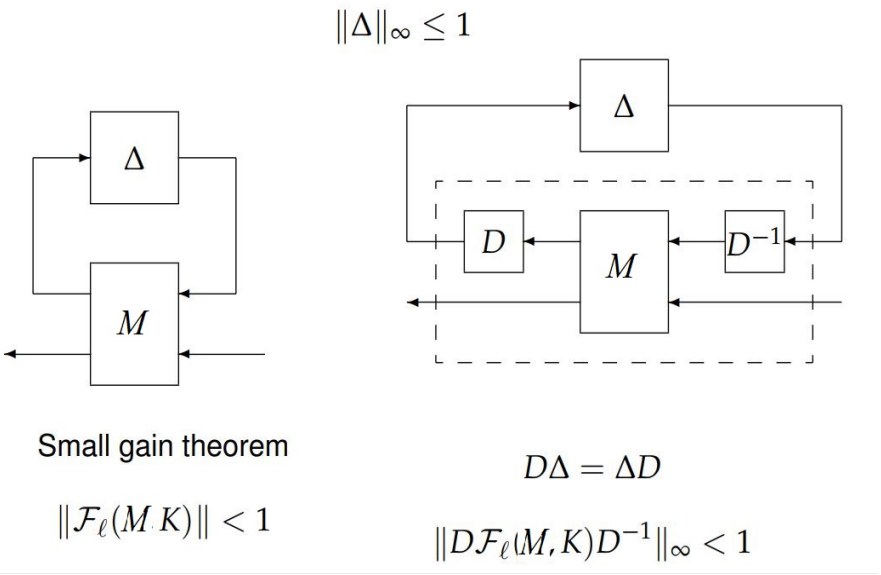

Figure 4.12. D Scaling
(Source: Helmerson (2017))

certainty matrix, destabilizes $F_L(P,K)$. Eq. 4.14 shows that the biggest singular value of $F_L(P,K)$ is the reciprocal of smallest singular value of the uncertainty matrix Δ to destabilize $F_L(P,K)$.

Apparently, $\mu\Delta\left(F_L(P,K)\right)$ is linked the closed-loop (CL) and the structured uncertainties Δ. A robust controller can be achieved by minimizing the largest $\mu\Delta\left(F_L(P,K)\right)$ value to replace $\|F_L(P,K)\|_\infty$ in Eq. 4.11. Nevertheless, there is no available method to calculate $\mu\Delta\left(F_L(P,K)\right)$. Accordingly, an iterative method studied by Mackenroth (2004) is utilized; D-K iteration.

$$\mu_\Delta\left(F_L(P,K)\left(j\omega\right)\right) \leq \inf_{\mathbf{D}\in\Xi} \bar{\sigma}\left(\mathbf{D}F_L(P,K)\mathbf{D}^{-1}\left(j\omega\right)\right), \tag{4.15}$$

where D is a scaling matrix in Ξ which is a set of diagonal scaling matrices, the entries of which are a combination of system and constant matrices. The D-K iteration can use $\inf \bar{\sigma}\left(\mathbf{D}F_L(P,K)\mathbf{D}^{-1}\right)$ to replace $\mu\Delta\left(F_L(P,K)\right)$ and aims to solve the following optimization problem:

$$\min_{\mathbf{K}(j\omega),\mathbf{D}\in\Xi} \bar{\sigma}\left(\mathbf{D}F_L(P,K)\mathbf{D}^{-1}\left(j\omega\right)\right). \tag{4.16}$$

If the D matrix is known, Eq.4.16 is a generic H_∞ optimization problem. After

solving the given optimization problem covering the interested frequency range with a known K, a series of $D(j\omega)$ at every corresponding frequency point ωi is formed by curve-fitting the rational transfer function matrix $D(j\omega)$. Thereafter, $D(j\omega)$ is kept steady to solve the controller K in the next iteration. Huo et al. (2016) formulated the D-K iteration as follows,

- Step I: Start with initial D (identity matrix usually).
- Step II: Keep D fixed and compute the optimization problem below

$$K = \min_{\mathbf{K}(j\omega),\mathbf{D}\in\Xi} \bar{\sigma}\left(\mathbf{D}F_L(P,K)\mathbf{D}^{-1}(j\omega)\right). \tag{4.17}$$

- Step III: After solving the given convex optimization problem, fix K this time and solve the following problem,

$$D(j\omega) = \min_{\mathbf{K}(j\omega),\mathbf{D}\in\Xi} \bar{\sigma}\left(\mathbf{D}F_L(P,K)\mathbf{D}^{-1}(j\omega)\right). \tag{4.18}$$

- Step IV: Curve fit the values to get a sequence of $D(j\omega)$. Then, get rid of the imaginary parts to get a new transfer function D_{new}
- Step V: Compare D_{new} with the previous one. If they are close enough to each other, stop the iteration. Otherwise, go back to Step II.

4.3. 3-Storey Robust Control Application

In this part, performances of the designed robust H_∞ controller with and without consideration of the uncertainties will be compared. A 3-storey civil structure is equipped with the MRD mounted to the first floor.

Uncertainties may change the model significantly. Fig. 4.13 shows the nominal and perturbed civil structure singular values. As can be seen in the figure, the singular values of the structures vary and deviate from the nominal value. Let us have a look at how to model the modal parameters having uncertainties.

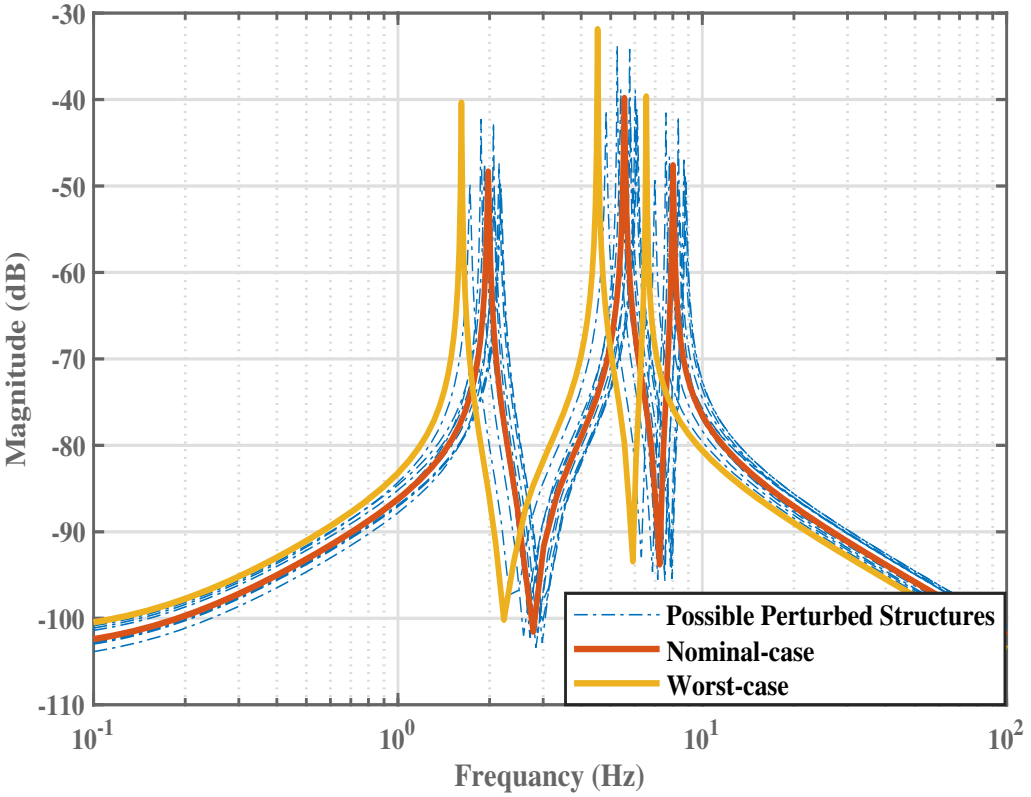

Figure 4.13. Singular values of possible perturbed structures

$$K_s = \begin{bmatrix} 2k + P_k(\delta_{k1} + \delta_{k2})k & -k - P_k\delta_{k2}k & 0 \\ -k - P_k\delta_{k2}k & 2k + P_k(\delta_{k2} + \delta_{k3})k & -k - P_k\delta_{k3}k \\ 0 & -k - P_k\delta_{k3}k & k + P_k\delta_{k3}k \end{bmatrix},$$

$$C_s = \begin{bmatrix} 2c + P_c(\delta_{c1} + \delta_{c2})c & -c - P_c\delta_{c2}c & 0 \\ -c - P_c\delta_{c2}c & 2c + P_c(\delta_{c2} + \delta_{c3})c & -c - P_c\delta_{c3}c \\ 0 & -c - P_c\delta_{c3}c & c + P_c\delta_{c3}c \end{bmatrix},$$

$$M_s = \begin{bmatrix} m + P_m\delta_{m1}m & 0 & 0 \\ 0 & m + P_m\delta_{m2}m & 0 \\ 0 & 0 & m + P_m\delta_{m3}m \end{bmatrix}. \quad (4.19)$$

All the possible perturbed structures have uncertainties in their system matrix, A, with different ratios. The worst-case scenario is achieved through the maximum gain

(the maximum singular value) computed according to the varying uncertainties. After the worst-case gain computations, the structure having worst uncertainties yields as;

$$K_s = \begin{bmatrix} 1.6k & -0.8k & 0 \\ -0.8k & 1.6k & -0.8k \\ 0 & -0.8k & 0.8k \end{bmatrix}, \; C_s = \begin{bmatrix} 0.8c & -0.4c & 0 \\ -0.4c & 0.8c & -0.4c \\ 0 & -0.4c & 0.4c \end{bmatrix}, \; M_s = \begin{bmatrix} 1.2m & 0 & 0 \\ 0 & 1.2m & 0 \\ 0 & 0 & 1.2m \end{bmatrix}.$$

$$k = k_{st} = 156250N/m, \qquad c = 42.25Ns/m, \qquad m = 200kg.$$

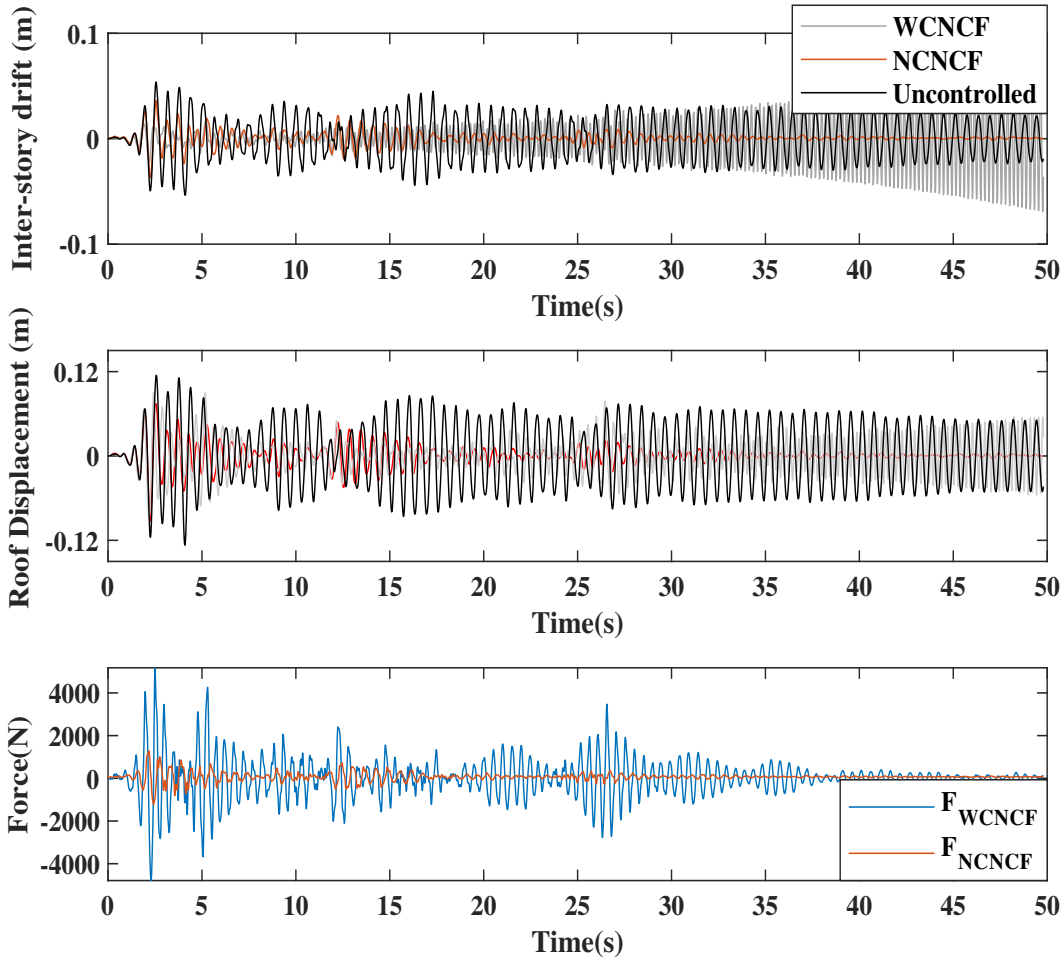

Figure 4.14. H_∞-controlled structure's responses

The structure having worst-case uncertainty has no instability issues for the structure without a controller. However, this does not mean that all structures will show small deformations under an earthquake. A controller aimed for a nominal structure may be destructive if existing uncertainties are not considered.

The roof displacements, the maximum inter-story drifts, and control forces for the worst-case nominal control feedback (WCNCF) and nominal-case nominal control feedback (NCNCF) structures are given in Fig. 4.14. The responses for the worst-case structure without a controller, which is depicted by a black line in the figure, are larger than the nominal-case responses given in the earlier chapters.

As seen in Fig. 4.14, a nominal controller may cause instability if the designer neglects uncertainties. In other words, in control implementations, the uncertainties should be taken into account seriously. The control forces increase thoroughly since the controller computes the required force considering the nominal-case structure modal parameters. As a result, instability occurs.

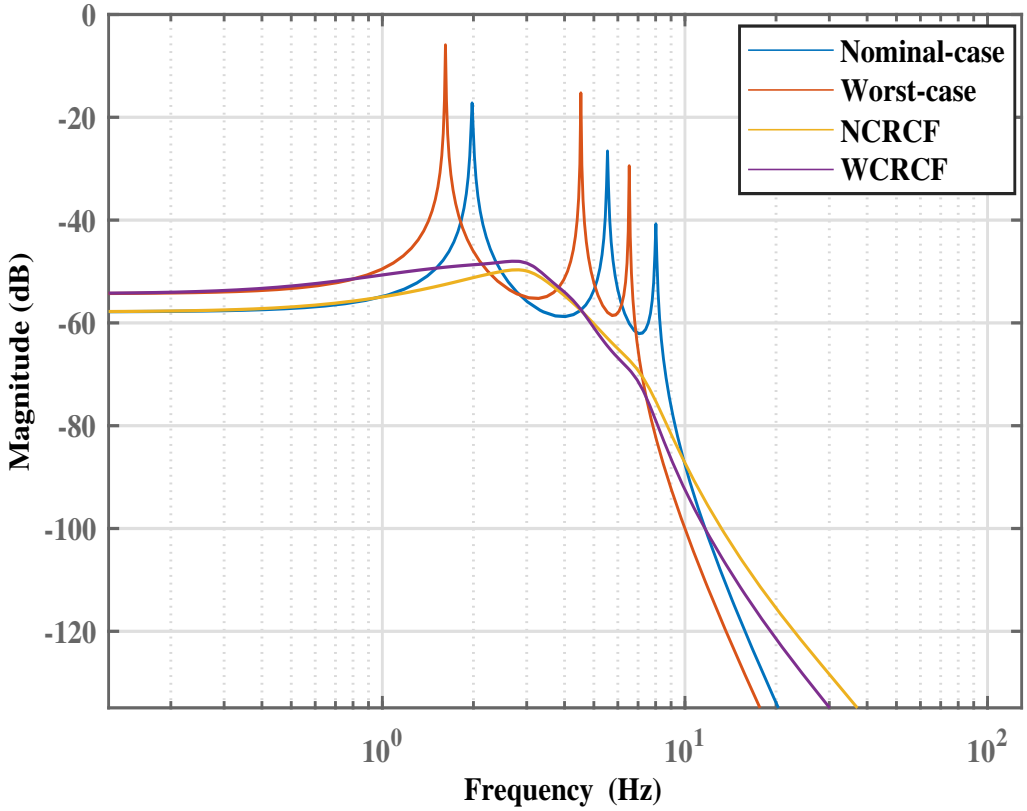

Figure 4.15. The Bode diagram of the robust-controlled structure

Fig. 4.15 shows the uncontrolled and controlled structure frequency responses. The nominal-case robust control feedback (NCRCF) frequency magnitudes are reduced by around 30dB at the first mode. Similarly, the worst-case robust control feedback (WCRCF) response magnitudes are decreased by more than 30dB. The achieved robust

controller can control both structures regardless of their modal parameters. Its stability margins are much wider than the nominal-case H_∞ controller.

The robust controller decreases the frequency amplitudes at peaks, but at the same time, it causes around 5dB upthrusts in between 2.5 and 5Hz. As a result, the closed-loop responses in the time domain increase.

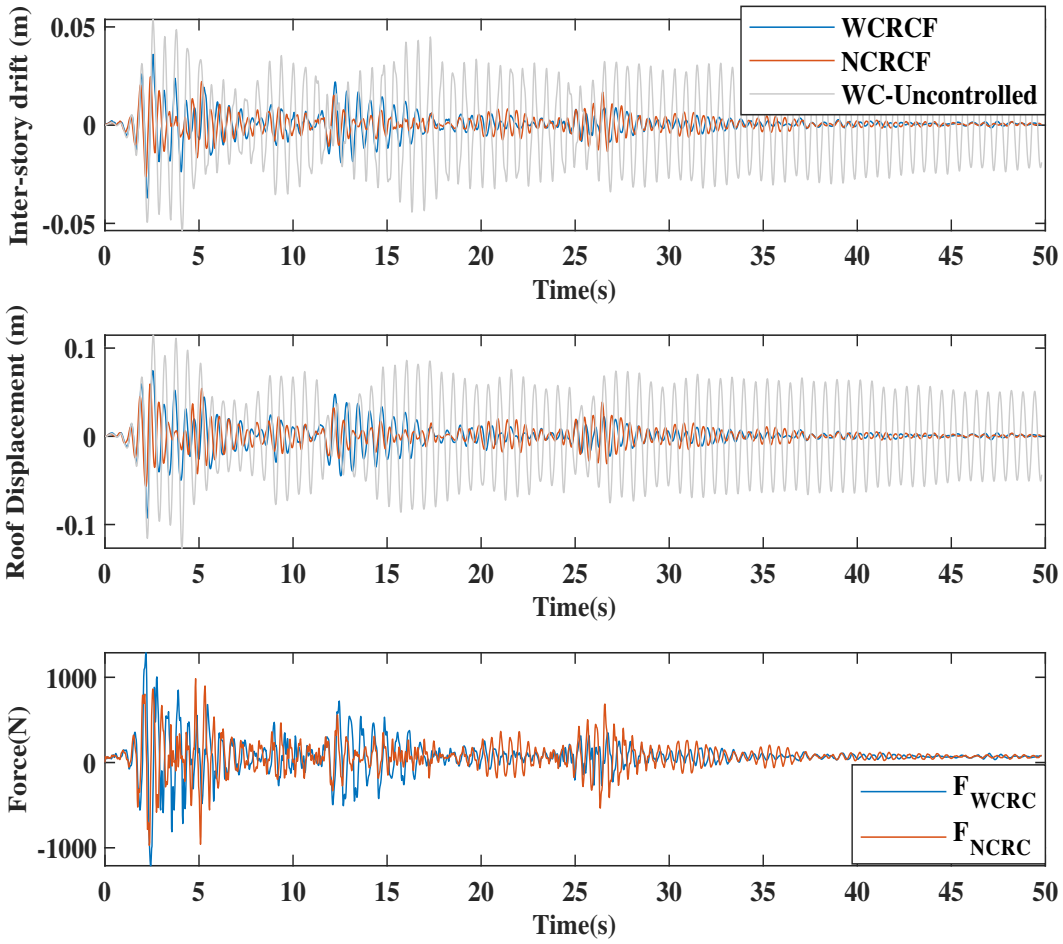

Figure 4.16. The robust controller-installed structure's responses

Simulations for the structures equipped with the robust controller are undertaken. In these simulations, the MRD is employed as the control device. The roof displacements and maximum inter-story drifts of the 3-story structure are given in Fig. 4.16. According to Table 4.1, the indices J_1 and J_5 for the nominal-case structure are equivalent to 0.7311 and 0.3137, respectively. Besides, the indices with the same robust controller are decreased to 0.4679 and 0.2436 for the worst-case structure. It can be said that the robust controller shows a satisfactory performance for the structure within given uncertainties.

Table 4.1. Performance indices of the robust controller

	J_1	J_2	J_3	J_4	J_5	J_6	J_7	J_8
Uncontrolled	1.0000	1.0000	1.0000	1.0000	1.0000	1.0000	1.0000	1.0000
NCRCF	0.7311	0.6690	0.6685	0.7720	0.3137	0.2637	0.7666	0.3156
WCRCF	0.4679	0.4578	0.3778	0.5429	0.2436	0.2280	0.5047	0.2512

In this chapter, a robust controller is put forward for a linear structure with uncertainties, and its efficiency is proven. In the following chapter, this robust controller is tested on a nonlinear structure, assuming that the nonlinearities can be treated as uncertainties.

CHAPTER 5

ROBUST CONTROLLERS FOR NONLINEAR SYSTEMS

In this chapter, a nonlinear 20-storey benchmark building will be controlled by a robust controller. In the determination process of the uncertainty ratios, changes formed by model nonlinearity is considered.

Gu and Quan (2004) reported that as the aspect ratio of buildings increases, the horizontal movements are getting large during the seismic excitation such as wind and earthquake. The resistance of tall structures against seismic loads can be tuned by changing mass, stiffness, and damping. Apart from these adjustments, passive, active, semi-active control devices, and the composition of these devices, hybrid controllers, were developed to increase tall buildings' seismic performances. Those controllers helped the structures to minimize the inter-story displacements and dissipate seismic energy.

In the literature, benchmark studies are developed to distinguish among the benefits of various controllers. Such studies are crucial for the successful improvements of both structural control devices and algorithms. Consequently, to compare which type of controllers are superior to others, benchmark studies were put forward.

Spencer Jr et al. (1998, 1997) proposed the first generation control problems. A 3-story civil structure model was used as a benchmark model to compare results. In these studies, the active mass damper (AMD) was employed as a controller device.

In the second generation of benchmark studies, a 20-Story building and a 76-story concrete tower were employed. Moreover, tuned mass dampers (TMD) were installed on the top floor of these structures. In the third generation, Yang et al. (2004) proposed a wind-excited benchmark model for a tall building. In order to perform realistic simulations, wind tunnel testing was developed. Further, the cable-stayed bridge benchmark problem was studied by several researchers (Dyke et al. (2003);Ali and Ramaswamy (2009); Wang (2004); and Yoshida and Dyke (2004)).

In vibration control of buildings, base isolators are one of the simplest devices that can be utilized in structures. However, these devices cannot be implemented in structures with low frequencies. For the control of high-rise buildings, therefore, Tuned-mass dampers (TMDs) were utilized as an alternative to base-isolators. The first TMD was pro-

posed by Ormondroyd (1928). TMD was employed by several researchers (Kareem and Kline (1995);Nagarajaiah and Sonmez (2007); Roffel and Narasimhan (2014); and Elias and Matsagar (2015)). Besides, it was reported that the buildings having TMD showed better responses than the buildings without TMD. Sadek et al. (1997) and Feng and Mita (1995) studied the optimization of TMDs. Yang et al. (2004) proposed the optimum location of passive TMDs regarding H_∞ and H_2 norms by employing the Linear Matrix Inequality method. The proposed optimal designs are capable of detecting both the optimal damper locations and the complementary optimum capacities.In their procedure, there is no need for simulations to obtain responses. Thus, the computational costs are decreased drastically compared to heuristic methods.

Yang et al. (2003, 2004) also proposed H_∞ and H_2 controllers for vibration control. They used accelerometers to measure the outputs. These outputs were not measured on all stories. The minimum number was chosen by considering the observability criteria. However, high noise issues were formed. The Kalman filter was employed to overcome this problem. (Yang et al. (1987, 1995, 1996, 2003, 2004))

Elias et al. (2016) proposed multi-mode control by utilizing distributed-TMDs instead of a single-TMD. Their aim was to distribute the heavy masses on different floors, and control higher vibrational modes besides the fundamental mode.

In the current study, we inquire how different types of TMD implementation affect the structure's behavior. Firstly, distributed-TMDs composing of 5 equal masses are implemented following the work of Elias et al. (2016). The 20-story benchmark building is nonlinearly-modeled, and simulated under seismic loads. Secondly, the benchmark building having a mere single-TMD (STMD) configuration is simulated to observe differences in responses. Compared by some pre-defined performance indices, the most improving TMD configuration, STMD, is chosen to implement on the benchmark structure. Thereafter, the study focuses on how to deal with nonlinearity-oriented uncertainties. The variation of the first five structural natural frequencies during the nonlinear simulations are utilized to determine the level of uncertainty.

In the last stage, the benchmark building with the STMD is empowered with a serially-connected actuator. The aim is to increase the performance of the STMD, where it falls out of the working frequency range. In this case, a generalized structure plant housing the control force, the disturbance, and the noise is designed. Herein, the Kanai-Tajimi filter is employed to mimic the corresponding earthquake data. The structural performances with the two different controllers: a) STMD and b) hybrid controllers are discussed at the end of this study. In this part, it is observed that the structure with hybrid

controllers outperforms the structure with mere passive dampers. Among these hybrid controllers, the robust controller considering the uncertainties, results in the best performance.

5.1. Mathematical Modeling

There are two different types of mathematical models for the structures: nominal and uncertain models. The former is modeled according to known geometry, material properties, and boundary conditions. Firstly, this nominal structure is modeled linearly and nonlinearly to observe responses such as displacement and inter-story drifts. These responses are compared for a set of selected earthquakes, and it will be shown below that the nonlinear model should be employed. The controller is based on an uncertain model of the structure system having deviations in mass, damping, and stiffness matrices from the nominal model. These uncertainties are removed from the structural model, and implemented as perturbations to the nominal structure system. As a result, the designer can model a robust controller that copes with these perturbations.

5.1.1. Nominal-Structure Models

The 20-story benchmark structure designed by Brandow & Johnston Associates for the SAC Phase II Steel Project was used for this benchmark study (Ohtori et al. (2004)). This structure was designed according to the requirements of the Los Angeles, California region. It represents a mid to high rise building.

The 20-story building is 80.77m in height and 30.48m by 36.58m in plan dimensions. Distances between the axes are 6.10m at the center, in two directions, with five axes in the north-south (N-S) direction and six axes in the east-west (E-W) direction. The lateral load resisting mechanism of the building is comprised of steel moment-resisting frames (MRFs). The following assumptions are made to represent the model: (i) The columns are hinge-connected at the base; (ii) In contrast to the benchmark study, static condensation was not utilized to decrease the degrees of freedom.

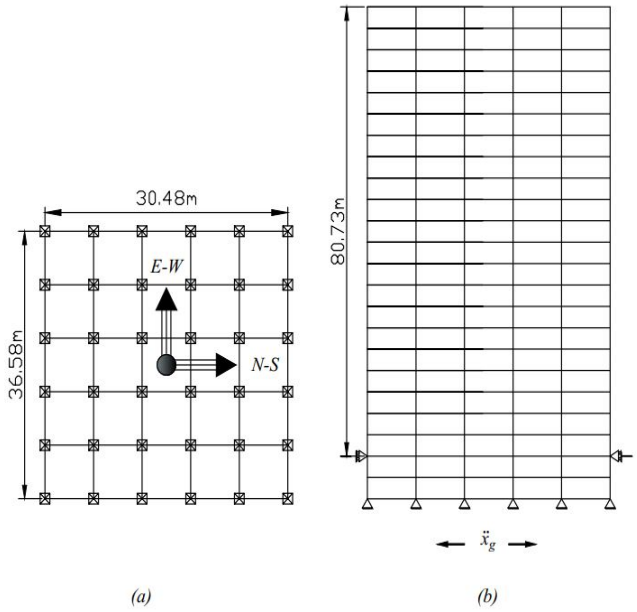

Figure 5.1. 20-storey benchmark building

- **Linear Model**

The linear model consists of 526 degrees of freedom (DOFs), including the splice locations where the column sections change. As mentioned above, all node locations and sections values are presented in the study of (Ohtori et al. (2004)).

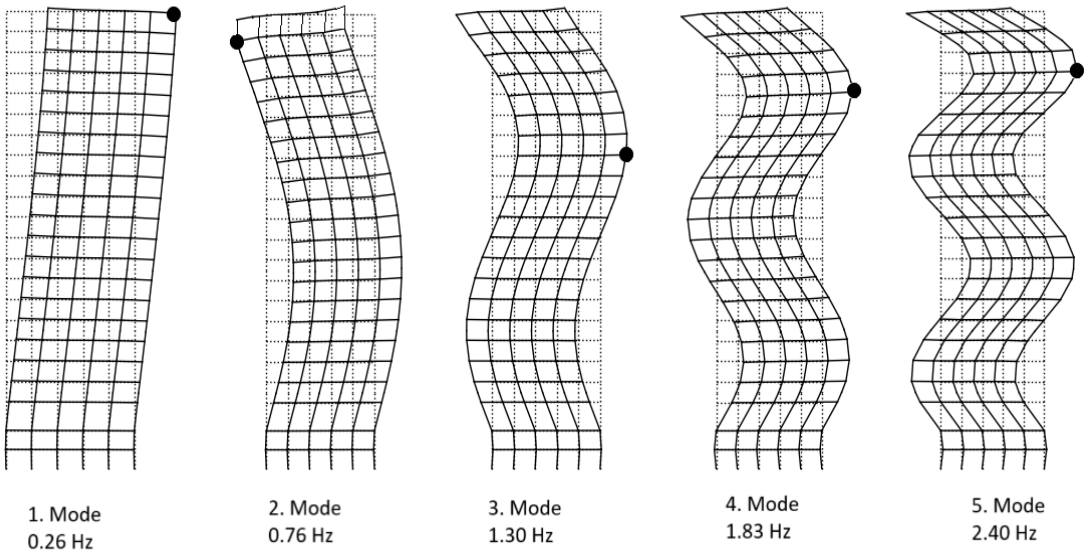

Figure 5.2. Mode shapes of the 20-storey benchmark building

The mode shapes are presented in Fig. 5.2 for the first five modes. The maximum dimensionless modal displacements are marked with black dots for the positioning of the tuned mass dampers.

- **Nonlinear Model**

The benchmark structure is modeled by implementing material and geometric nonlinearities.

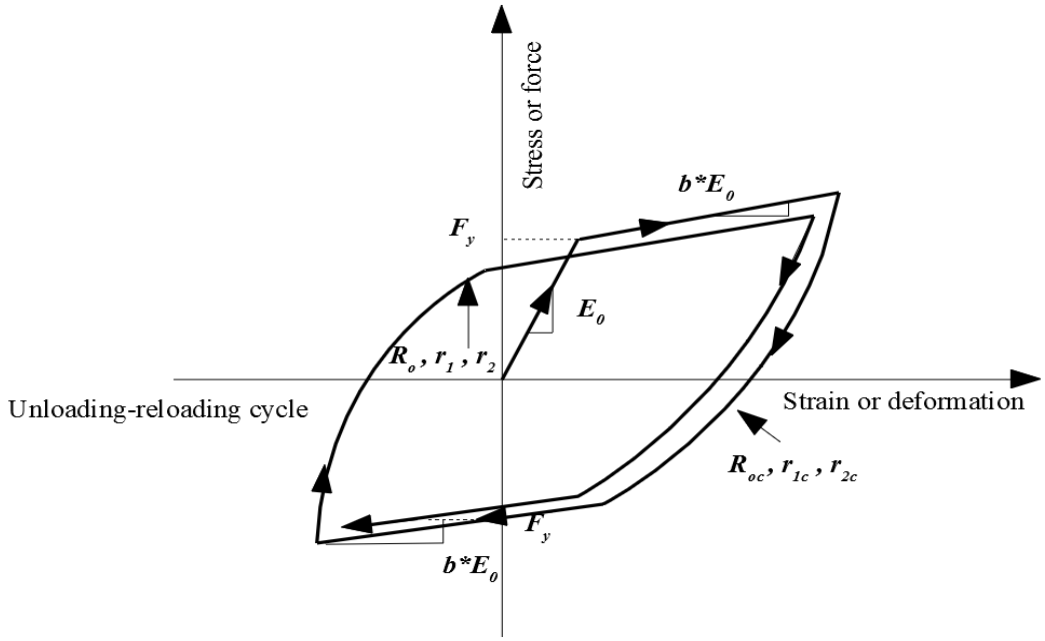

Figure 5.3. Nonlinear characteristic of the steel material

Fig. 5.3 shows a general uni-axial material with combined kinematic and isotropic hardening and optional non-symmetric behavior in the current study. F_y is the yield stress (235 MPa), and E_0 is the Young's Modulus (2.1×10^{11} N/m^2). The post-yield modulus is employed as one tenth of the initial elastic modulus value in this study ($b = 0.1$) (Yun and Gardner (2017)). $R_o = 20.9$, $r_1 = 0.91$ and $r_2 = 0.12$ are the control parameters of the exponential transition from linear elastic to the hardening asymptote. For a more realistic material characteristics, R_{oc}, r_{1c} and r_{2c} are chosen as 18.9, 0.91 and 0.12 a non-symmetric behavior is achieved (Zsarnóczay and Baker (2020)).

The maximum inter-story drifts can be shown as an example of why the nonlinear model is employed. Fig. 5.4 shows that the nonlinear benchmark model shows larger

inter-story drifts at the lower stories than the linear model under the Northridge earthquake.

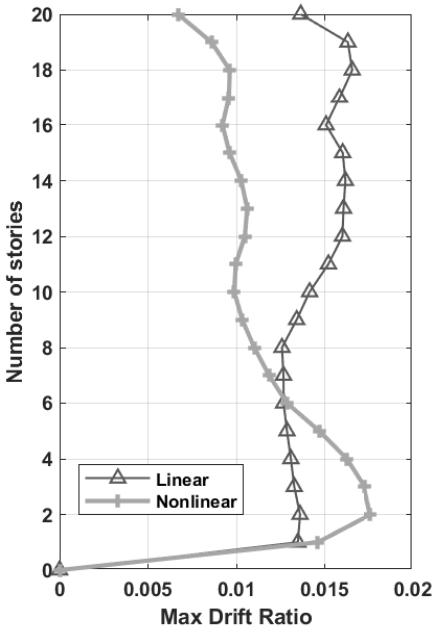

Figure 5.4. Responses of the benchmark building subjected to Northridge EQ

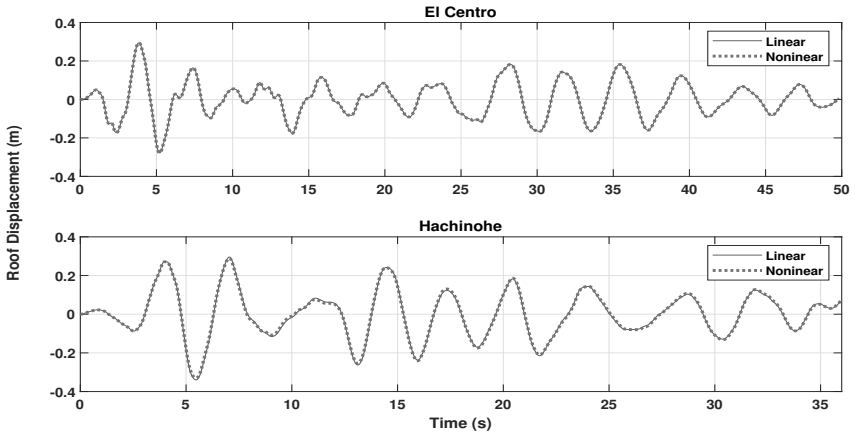

Figure 5.5. Responses of the benchmark building subjected to El Centro and Hachinohe EQs

Fig. 5.5 shows the differences between the roof displacements of the linear and the nonlinear models subjected to El Centro and Hachinohe earthquakes relative to the ground. Since the exerted earthquakes do not cause the structure to yield, these responses are similar in the linear and nonlinear cases.

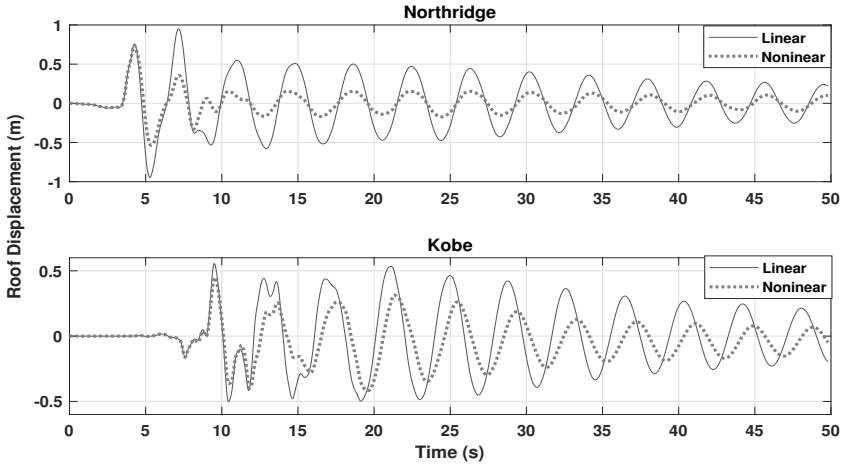

Figure 5.6. Responses of the benchmark building subjected to Northridge and Kobe EQs

Apparently, these two earthquakes are rather destructive. This outcome can be explained by the fact that these earthquakes have more frequency contents matching the structure's first two frequencies with higher amplitude. As expected, the nonlinear model shows unrestored displacement after the linear force capacity is exceeded.

Fig. 5.7 shows the frequency values of the structures during earthquakes. The damage that occurred in the structure subjected to the Northridge EQ is beyond the reversible limits. As a result, it is concluded that the nonlinear effects should be taken into account to achieve more realistic results in the simulation of the benchmark model.

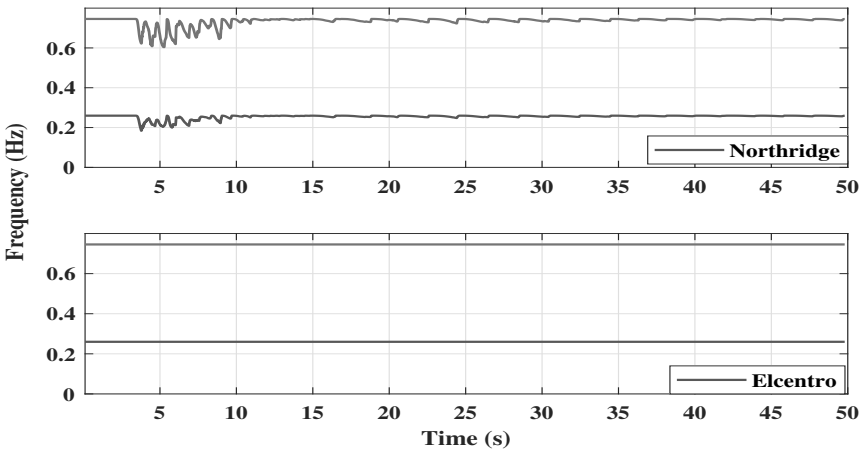

Figure 5.7. Natural frequencies of the benchmark building subjected to Northridge and El Centro EQs

5.1.2. TMD Design & Location

A comparison of the TMDs designs for the linear benchmark model is presented by Elias et al. (2017). Accordingly, the proposed TMDs by Sadek et al. (1997) et al outperformed the remaining designs. Therefore, in this study, the TMD design by Sadek et al. (1997) is employed for the simulation of the nonlinear benchmark model.

The following equations were proposed by Sadek et al. (1997) presented as equations between Eq. 5.1-Eq. 5.3 and here they are repeated.

$$\mu = \frac{m}{{\Phi_i}^T[M]\Phi_i} \quad f = \frac{1}{1+\mu\Phi}\left[1-\beta\sqrt{\frac{\mu\Phi}{(1+\mu\Phi)}}\right] \quad and \quad \zeta = \Phi\left[\frac{\beta}{1+\mu}+\sqrt{\frac{\mu}{(1+\mu)}}\right], \tag{5.1}$$

where Φ_i and β are the modal displacement of the corresponding mode and the structure damping. Apart from this, there is also another optimum damping ratio formulation which was proposed by Feng and Mita (1995). The formulation is given as

$$\zeta = \frac{1}{2}\sqrt{\frac{\mu(1-\mu/4)}{(1+\mu)(\mu/2)}}, \tag{5.2}$$

and the damping coefficients for all the proposed TMD models above are calculated by

$$c_i = 2\zeta m_i \omega_i. \tag{5.3}$$

Fig. 5.8.d and Fig. 5.8.e show the configuration of the distributed multi-TMDs (MTMD) and the STMD, respectively. In the structure with the MTMD, the locations of the TMDs are chosen by regarding the largest amplitudes of mode shape likewise Elias et al. (2017) did, whereas STMD is located at the top of the structure. The MTMD number is limited by 5 since 5 modes cover more than %90 of the total response. All of the TMD parameters were calculated by regarding Sadek et al. (1997). The mass ratio, μ, is taken as 0.05 to make results comparable with the previous studies (Elias et al. (2017); Gill et al. (2017)). This study's main focus is to understand the role of the nonlinearity-based uncertainties, to make use of it, and to have better vibration control by employing a hybrid controller composed of TMDs and actuators.

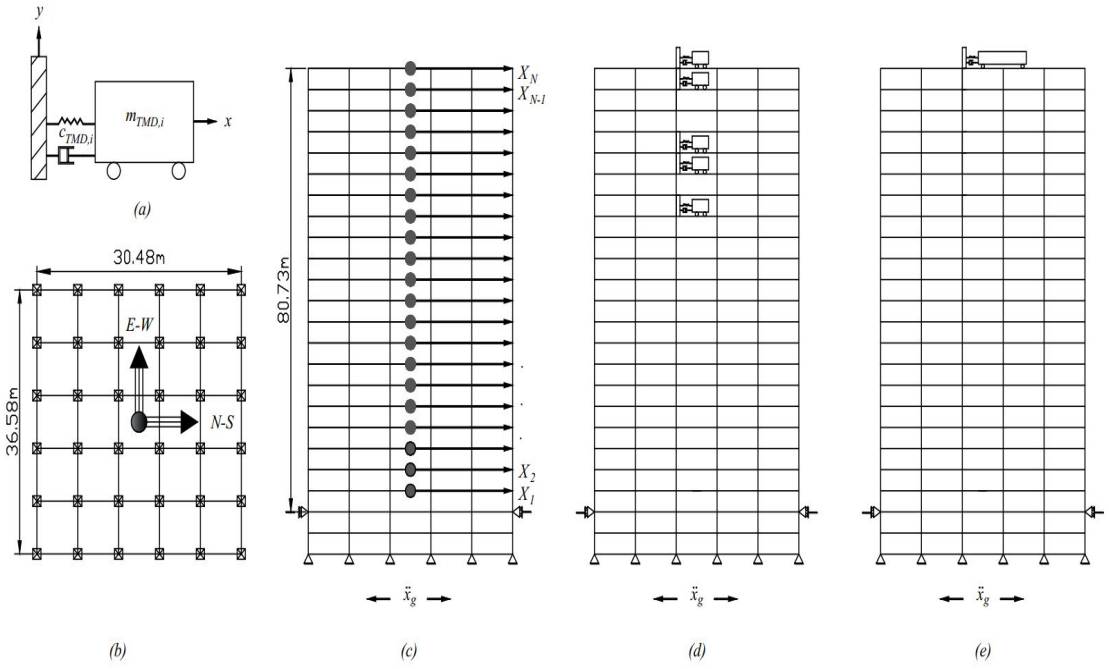

Figure 5.8. 20-storey benchmark building having MTMDs

The equation of motion is modified as the TMD system is attached to the benchmark model. Eq.(5.4) represents system dynamics of the nonlinear benchmark building model, where uncertainties in mass, stiffness, and damping exist.

$$K_{tmd}\ x(t) + C_{tmd}\dot{x}(t) + M_{tmd}\ddot{x}(t) = \Gamma_{c_{tmd}} f_c(t) - M_{tmd}\Gamma_{d_{tmd}}\ddot{x}_g(t), \tag{5.4}$$

where M_{tmd}, C_{tmd} and K_{tmd} are the $(N+n)\times(N+n)$ mass, damping and stiffness matrices of the structure installed with TMDs, $\Gamma_{d_{tmd}}$ is the $(N+n)\times 1$ identity vector, $f_c(t)$ is the active control force applied to the structure, and $\Gamma_{c_{tmd}}$ is the $(N+n)\times 1$ actuator location vector.

$$M_{tmd} = \begin{bmatrix} [M_s]_{N\times N} & 0 \\ 0 & [M_n]_{n\times n} \end{bmatrix},$$

$$K_{tmd} = \begin{bmatrix} [K_s]_{N\times N} - [K_n]_{N\times N} & -[K_n]_{N\times n} \\ -[K_n]_{n\times N} & [K_n]_{n\times n} \end{bmatrix},$$

$$C_{tmd} = \begin{bmatrix} [C_s]_{N\times N} - [C_n]_{N\times N} & -[C_n]_{N\times n} \\ -[C_n]_{n\times N} & [C_n]_{n\times n} \end{bmatrix} \tag{5.5}$$

where n is the number of the installed TMDs. N is the number of the degrees of freedom of the building without TMDs. In order to decide where to place TMDs, modal analysis is conducted by considering the nominal model only. Subsequently, n number of TMDs are placed at the building's stories, where modal displacements are maximum in first n dominant modes(Elias et al. (2016)).

5.1.3. TMD Selection

Herein, our goal is to see which passive TMD configuration results in a better response. This is considered to be important for the ultimate control design since a control failure will result in the pure structure with TMD only.

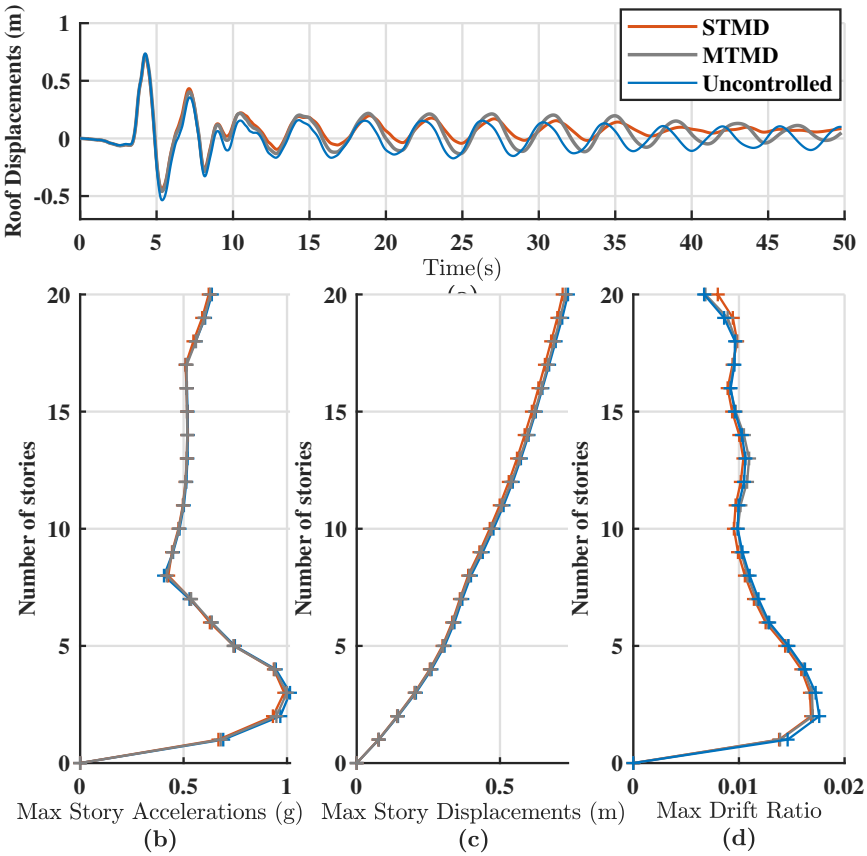

Figure 5.9. TMDs performances comparison

To make a fair comparison, the two different TMD-setups, STMD and MTMD, are simulated by using the Northridge Earthquake. This record is one of the earthquakes

employed in the benchmark studies, and it is selected in this study because it results in the largest structural response compared to the remaining benchmark EQ records.

Fig. 5.9.a shows the roof displacements of the nonlinear structure model. It can be seen that the maximum displacement during the earthquake pulses do not show major differences for the three structural configurations. The main pulses fade after approximately 12 seconds, resulting in structural free-vibrations. Here it can be seen that the STMD is more efficient than the MTMD setup. In fact, the MTMD setup and the uncontrolled structure shows the same free-oscillation magnitudes.

In contrast, Fig. 5.9.b shows that there is not much difference in the absolute story accelerations, which can be interpreted as no significant difference in the lateral forces acting on the stories.

The maximum story displacements and max drift ratios are given in Fig. 5.9.c-d, respectively. These maximum values occur at $t = 4s$ at which the TMD is not satisfactory. It can be concluded that the STMD leads to a relatively better performance, and therefore, the hybrid controller design is setup for the nonlinear benchmark building with the STMD.

5.2. Controller Design

The considered control device consists of a TMD that can be fine-tuned by using active control. Here, the STMD is considered to provide passive-control to the building, and the active control force will be designed to fine-tune the system response.

5.2.1. Configuration

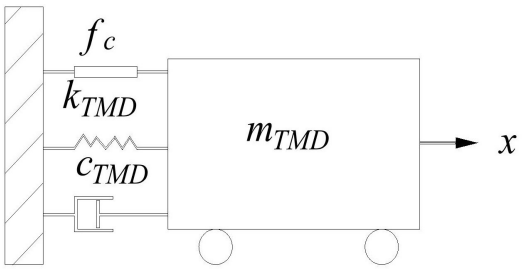

Figure 5.10. Hybrid controller setup

The conceptual design of an active tuned mass damper (ATMD) is shown in Fig. 5.10. The hybrid control is based on a setup consisting of a STMD. The required control force, f_c, is provided through an actuator, and a H_∞ controller is designed in order to mitigate vibrations of the 20-story benchmark building.

5.2.2. Generalized Plant Construction

The computation of an optimal controller for the structure system is transformed into a generalized control plant frame. To adjust the plant (the structure) performance (the building earthquake performance), weighting functions are used (Gu et al. (2005)).

5.2.3. Controller Design for Case I: Nominal Model

A block diagram representation of the civil structure system is presented in Fig. 5.11.

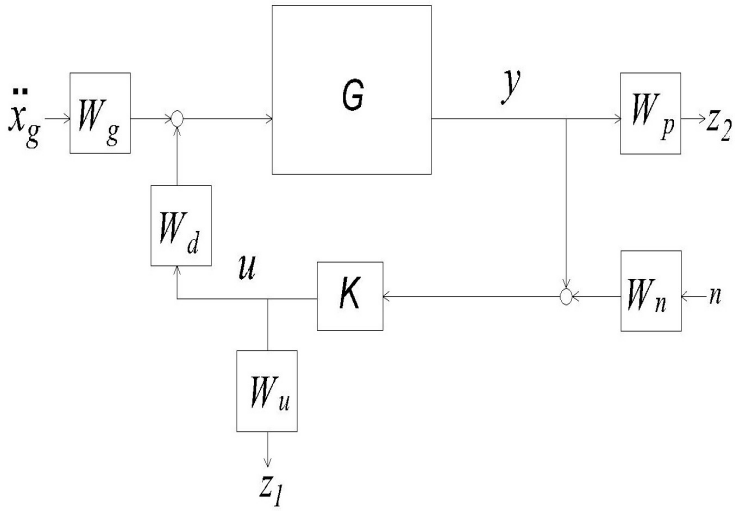

Figure 5.11. The generalized plant for a seismically excited nominal civil structure

In Fig. 5.11, K represents the controller, which to be designed. The frequency-domain weighting function W_g shapes the spectral content of the disturbance, $\ddot{x}_g$, modeling the earthquake excitation. W_g is designed as a second-order system that mimics the frequency content of the implemented earthquakes.

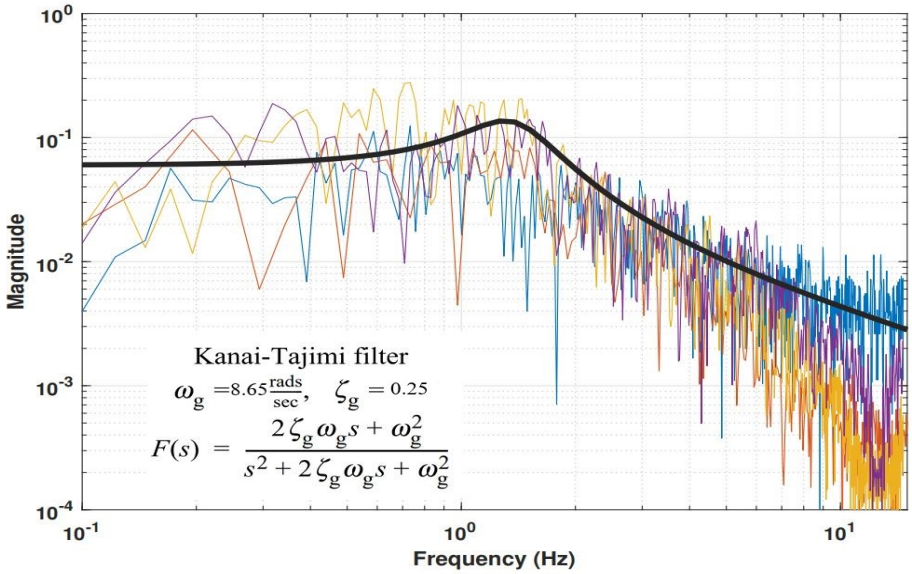

Figure 5.12. The designed Kanai-Tajimi filter

Fig. 5.12 shows the Kanai-Tajimi spectrum implementation to obtain $F(s)$, which is the transfer function of W_g, Lin and Yong (1987). A higher degree model for $F(s)$ may be used as well, but this penalizes the controller by a higher number of states.

The matrix $W_p = 5\ diag(\ [\ ones(1, N)\ 0\ ]\ )$ is weighting the regulated response, which is assumed to be the inter-story drift for each story, $W_u = 10e-6$ is weighting the control signal, and W_n is weighting the measurement noise n. The signal to noise ratio (SNR) and cut-off frequency was set as 10 and 100 Hz, respectively. The 0.06 s delay in the actuator is modeled by W_d.

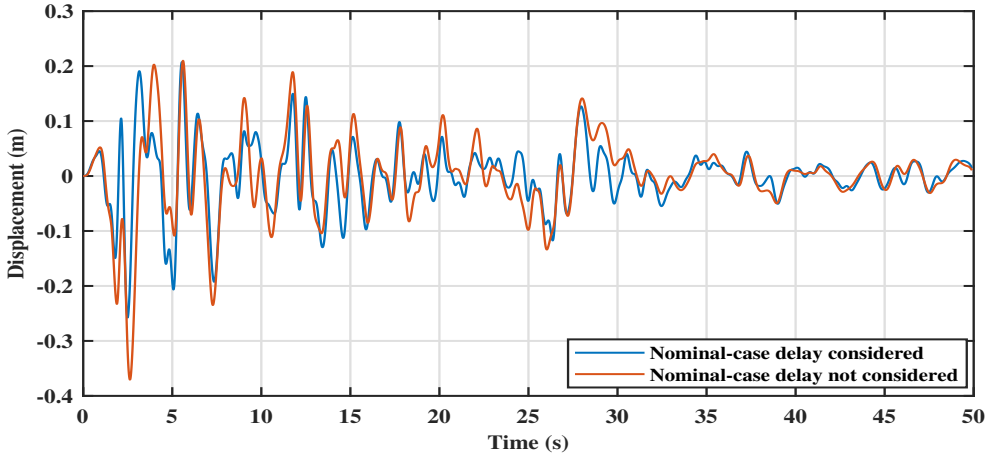

Figure 5.13. Delay effects

The negligence of the delay in the modeling for the current model can be well perceived through Fig. 5.13. As seen, the required control forces are always almost larger since the delay causes instability.

The input excitation, w, consists of the earthquake excitation $\ddot{x}_g$ and the measurement noise n. The output z is composed of the frequency weighted-regulated response and the control force. This control system which is based on the nominal benchmark model has a comparatively low computational cost compared to the uncertain structural model. Consequently, to keep modeling relatively simple and make both cases comparable, N is chosen as 20. On the controller design part, to achieve the required controller size, Guyan reduction is employed. While doing so, only the lateral displacements are considered. Thus, the reduced-order nominal model diverges from the real one on the controller side as shown in Fig. 5.14. However, this variance is compensated by the H_∞ controller, thanks to its stability margins.

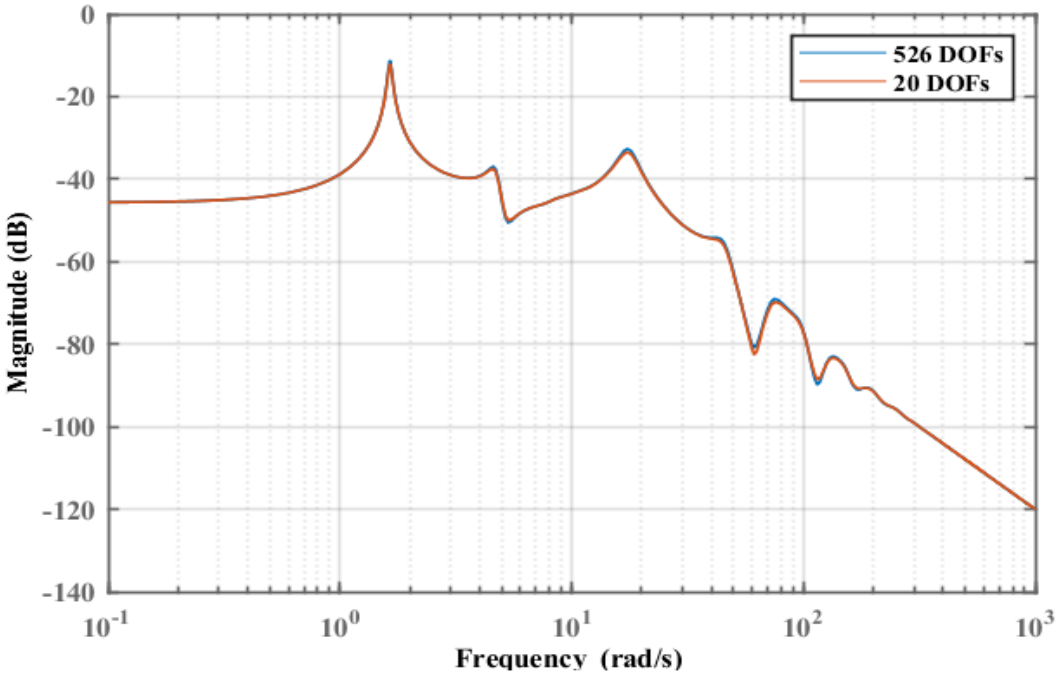

Figure 5.14. Full vs Truncated Models

In the control algorithm, control forces that will cause the system to satisfy the desired exogenous output, and at the same time, maximize or minimize a chosen cost function are determined. The study's cost function is to minimize the infinity-norm of the ratio between exogenous inputs and outputs, γ value.

5.2.4. Controller Design for Case II: Uncertain Model

The uncertain model can be represented as shown in Fig. 5.15. The robust controller can be designed through small gain theorem, Zhou and Doyle (1998). According to the small gain theorem, the generalized civil structure plant is internally stable for all Δ with

$$\begin{aligned} \|\Delta\|_\infty \leq 1/\gamma \quad &\Longleftrightarrow \quad \|F_L(P,K)\|_\infty < \gamma, \\ \|\Delta\|_\infty < 1/\gamma \quad &\Longleftrightarrow \quad \|F_L(P,K)\|_\infty \leq \gamma, \end{aligned} \tag{5.6}$$

where P represents the generalized civil structure plant. The value γ has the sense of energy ratio between exogenous output vector z and exogenous input vector w.

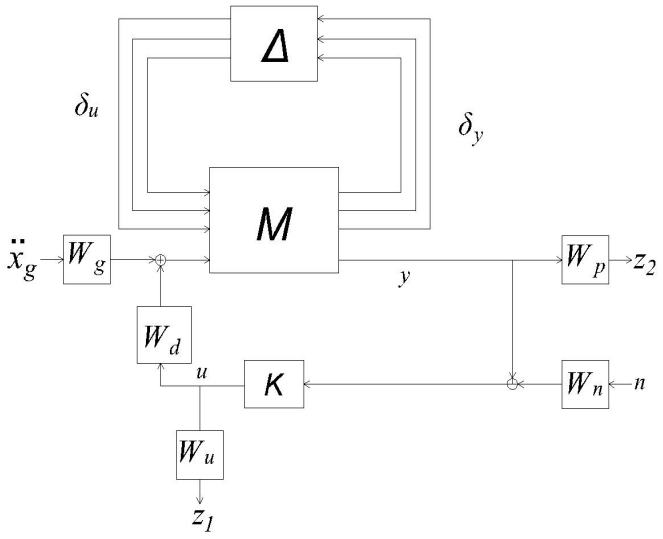

Figure 5.15. The generalized plant for a seismically excited uncertain civil structure

As γ tends to its minimal value, the above formulation can also be named as an optimal H_∞ control problem according to Skogestad and Postlethwaite (2007) as given in Chapter 4. The structured singular value μ is a powerful tool for analyzing robust performance with a defined controller. Nevertheless, one may also seek to find the controller that minimizes a defined μ-condition: the μ-synthesis problem, (Packard (1989)). As a result, it becomes possible to minimize the peak γ value by penalizing the controller by a

higher number of states. In other words, the less the peak value the controller achieves, the higher number of states the controller has. For this reason, the designed robust controller that satisfies the criteria given in *Eq*.5.6 results in 127 states, whereas the H_∞ controller has only 65 states.

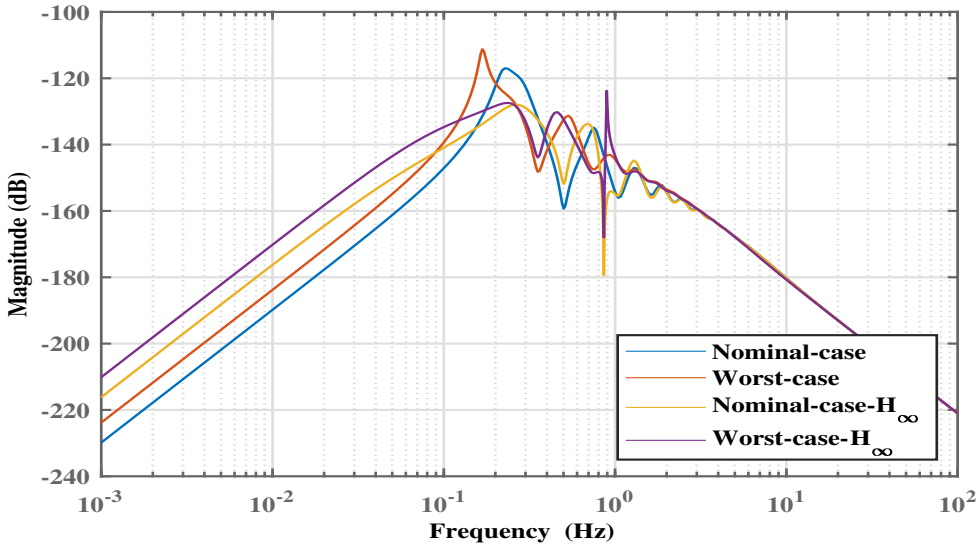

Figure 5.16. Bode responses of the structure with and without uncertainties

Fig. 5.16 shows the linear structure with and without H_∞ controllers for both the nominal-case and worst-case uncertainties. The nominal controller amplifies the worst-case structure frequency responses at around 1 Hz.

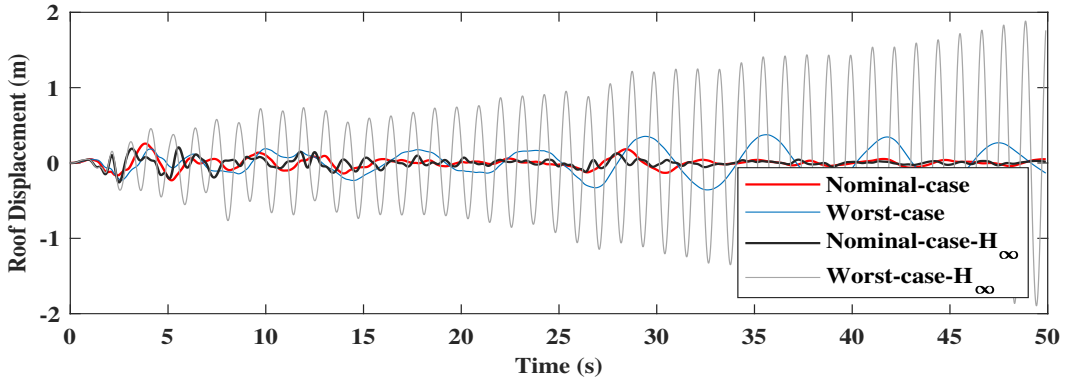

Figure 5.17. The responses of the structures subjected to the El Centro

These frequency responses were tested by the El Centro earthquake, and the results are given in Fig. 5.17. It is seen that the nominal-case uncertainty considered controller might drive the structure to instability depending on its uncertainty ratio.

5.2.5. Nonlinearity-Based Uncertainty Ratio Definition

Herein, a new approach will be put forward to cope with the nonlinearities in the structures in a robust manner. As known, during an earthquake, if the structure does not remain in the linear region, some of its parameters change, such as stiffness and related modal frequencies, and modal shapes. These stiffness shifts can be classified as uncertainty. It is possible to develop a new approach covering these uncertainties based on nonlinearities to robustly stabilize the structure.

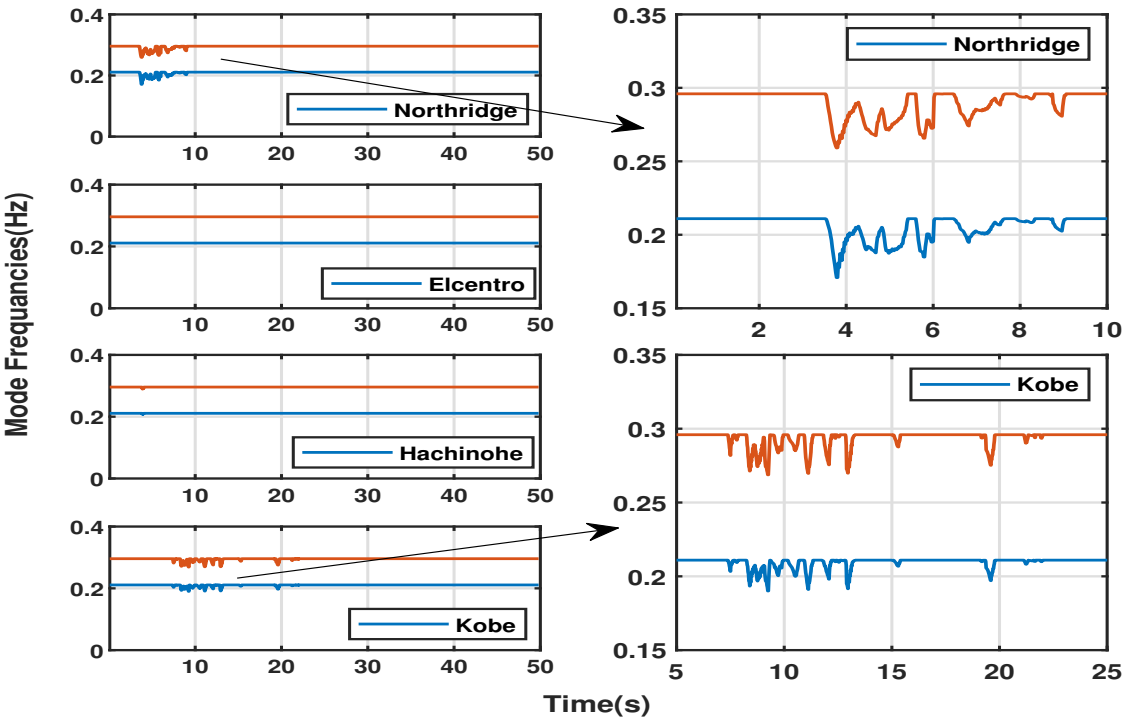

Figure 5.18. The first two modes of the structure having STMD during the earthquakes

In Fig. 5.18, the first two modal frequencies of the benchmark building are given under the corresponding earthquakes. The results are achieved via eigenvalue analysis undertaken at every time interval.

Fig. 5.18 clearly shows that some earthquakes put the structure in the nonlinear region, while others do not. It can be because of the peak ground acceleration and/or the earthquake frequency content matching the structure's lower modes. (See Fig. 2.2)

It is observed that, the frequency values face a reduction up to 20 percent (from 0.21Hz to 0.17 Hz). This corresponds roughly to a %30-35 stiffness degradation, assuming that the mass of inertia remains unchanged.

$$\frac{\omega}{\omega_o} \cong \%80 \longrightarrow \frac{k}{k_o} \cong \%65. \tag{5.7}$$

Hence, we treat these variations as uncertainty and insert them into the uncertainty block. Accordingly, these nonlinearity-based uncertainties are taken into account to design a robust controller, which is satisfactory for nonlinear cases. In addition, %10 uncertainty is considered for the control input. Apart from all, the uncertainties in damping values are neglected since it increase computational-cost drastically. To compensate it, the uncertainty ratio of the stiffness are increased to %40 in the current study.

In robust controller design, the truncated linear model is employed. Thereafter, this robust controller is installed on the nonlinearly-modeled structure.

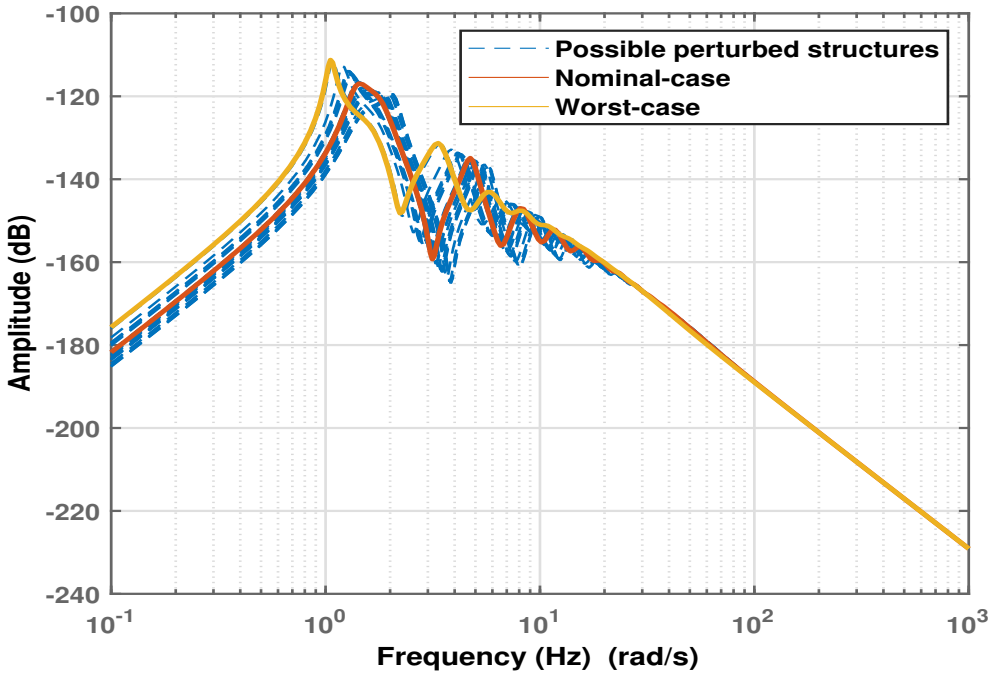

Figure 5.19. Frequency response of possible perturbed structures

Fig. 5.19 shows how the uncertainties inserted into the linear structure change its frequency characteristics. It is obviously seen that the worst-case structural model frequencies are matching the nonlinear model's lowest frequency values. The possible perturbed structures, which are the structures with uncertainties in different proportions, represent the benchmark building modeled nonlinearly during the earthquakes. What we assume is that these possible perturbed structures can be interpreted as the different phases of the structure at different time steps during the earthquakes are exerted. In other words, the nonlinearly modeled structure is varying within the range between the nominal and the worst-case model representations. However, it does not mean that all these possible perturbed represent the model at the varying nonlinear model at different time intervals. In contrast, they only cover all the yielded structure characteristics. The gap between these two models is relatively much and should be taken into account seriously. Our approach is to test whether the designed robust controller based on linear uncertain model can control the nonlinearly modeled benchmark structure.

5.3. Simulation Setup & Analysis

In the current study, the benchmark structure is nonlinearly modeled in the OpenSees framework (Welch et al. (2003)). The controller is designed in the Matlab environment.

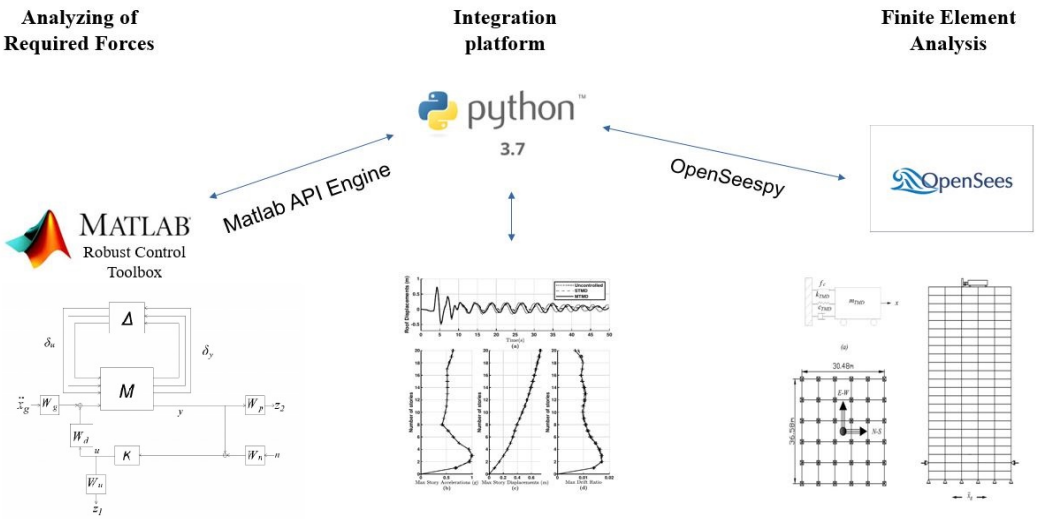

Figure 5.20. Hybrid Simulation Setup

These two different environments create a coupling problem that requires both controller and time history analysis simulations to await each other's results to finish. This problem mainly occurs in such systems containing structural control, wind-structure, and soil-structure interactions, in which Finite Element Analysis is used for simulating the structural responses.

An efficient integration of a FEA program into various other software platforms is eminent for the development of coupling systems. The complexity of the existing integration methods makes this process burdensome. OpenSees is a TCL-based framework in which an API engine was not found. Such an engine is strongly needed to undertake nested simulations. Vice-versa, a similar engine within Matlab could not be established to revoke OpenSees. These conditions forces us to use a method that integrates both the controller (Matlab) and the FEA framework (OpenSees) into another software environment. Subsequently, the OpenSees.py library is employed in the Python 3.7 environment to establish a direct link between OpenSees and Python. Similarly, the Matlab API engine is implemented to use Matlab functions directly within Python. As a result, a hybrid simulation method is developed to integrate Matlab and Opensees into each other to realize nonlinear structural response simulations together with optimal and robust control force implementations.

5.4. Results & Discussions

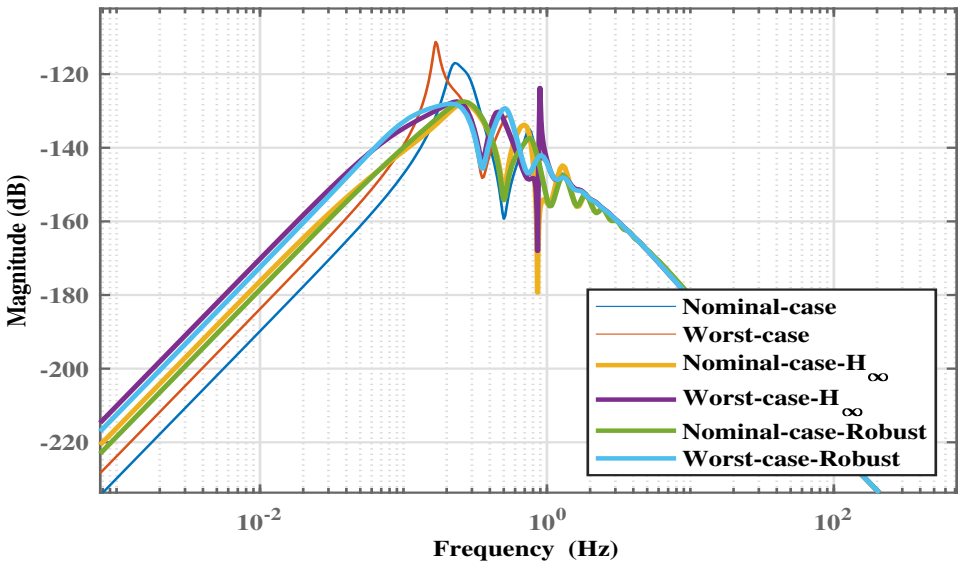

Figure 5.21. Bode responses of the structure

The benchmark building model is controlled by four different control strategies; STMD, MTMD, ATMD-H_∞, and ATMD-Robust. The performance of these controllers is investigated by using earthquake simulations. The uncontrolled mere structure results are shown in the response figures as a reference.

Fig. 5.21 shows the Bode response of the robust- and nominal-controlled benchmark building with and without uncertainties. The robust controller outperforms the nominal controller for the worst-case uncertainty structure.

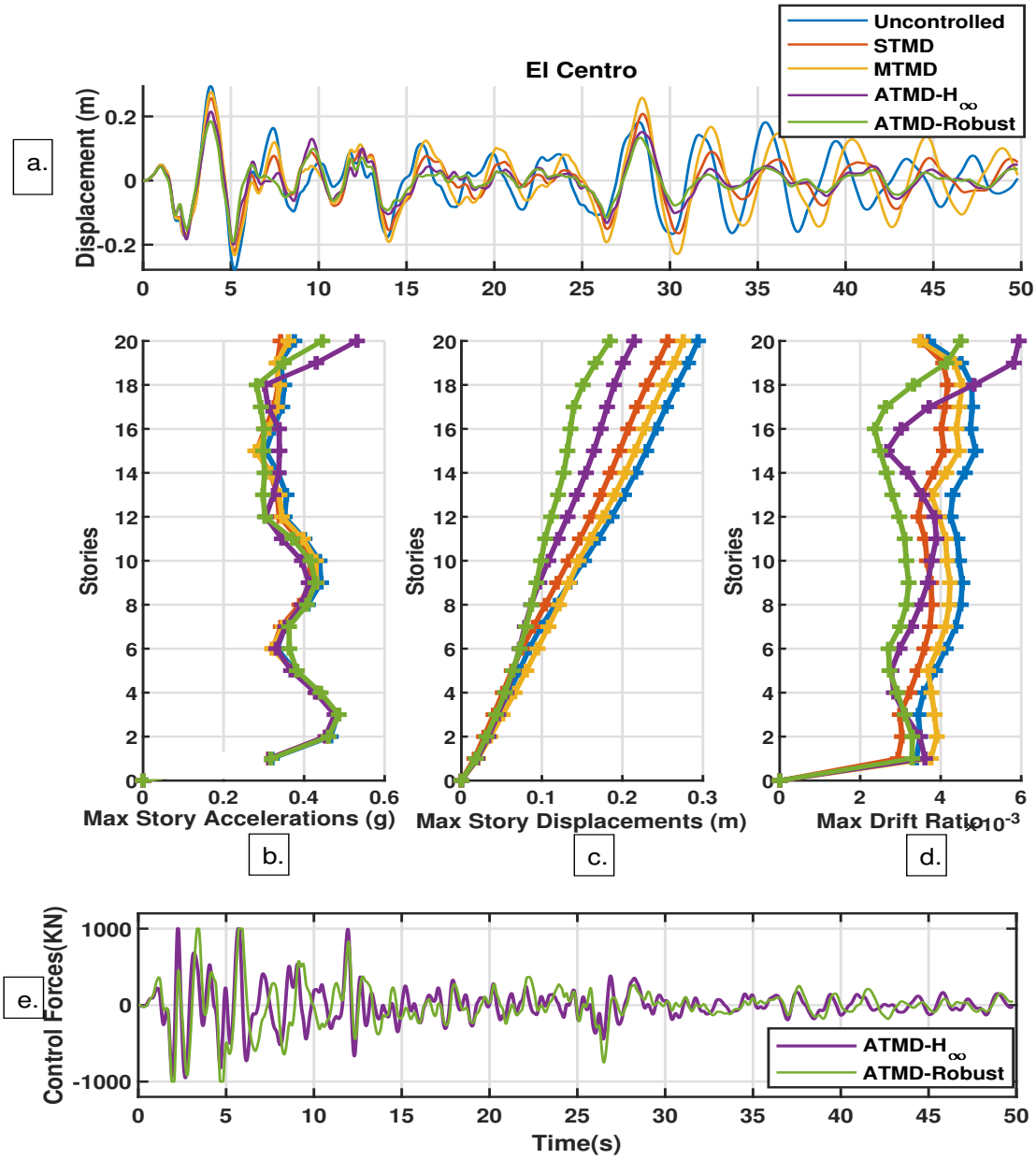

Figure 5.22. Structural responses under the El Centro earthquake

Fig. 5.22 shows the results of the structure with different control strategies subjected to the El Centro earthquake. Recall that the structure remains in the linear region (See Fig. 5.18) and the responses reflect the control performances on the nominal model. Admittedly, the structures with hybrid controllers show higher maximum acceleration values on the top floors due to the actuator forces. It can be concluded that these values are still lower than the top floors' elastic shear capacity, because the structure remains in its elastic region.

All controllers yield better responses than the uncontrolled structure according to the maximum story displacements relative to the ground. The applied hybrid controllers minimize the peak displacement values better at the higher stories, especially after the sixth floor. However, the same is not valid for the maximum inter-story drifts. For the uncontrolled and the TMD-cases, there is relatively an unvarying trend all the way up to the 20th floor. On the other hand, the structure with the ATMD-H_∞ hybrid controller shows a bigger variance, whereas the ATMD-robust hybrid controller case shows a uniform response between the first and the 16th stories. According to Fig. 5.22.a, the free vibration amplitudes are lowest for the ATMD-robust controller. The STMD leads to lower stored energy than the uncontrolled structure. The MTMD, however, increases the stored energy. The ratios of the controlled energies with respect to the uncontrolled stored energies can be depicted in Table. 5.1 as index J_5.

The actuator force is limited by 1000 KN to eliminate the possibility of shear failure at the top floor's columns.

Table 5.1. El Centro earthquake performance indices

	Uncontrolled	**STMD**	**MTMD**	**ATMD - H_∞**	**ATMD-Robust**
J_1	1.00	0.87	0.94	0.73	0.65
J_2	1.00	0.86	0.93	1.22	0.92
J_3	1.00	0.99	0.99	1.10	1.00
J_4	1.00	1.00	1.01	1.02	0.98
J_5	1.00	0.80	1.08	0.62	0.53
J_6	1.00	0.75	1.04	0.76	0.64
J_7	1.00	0.91	0.94	1.03	0.92
J_8	1.00	0.97	0.99	0.97	0.97

In Table. 5.1, the performance indices are given for all control strategies. According to these values, it can be claimed that the MTMD shows the worst performance in terms of minimization of the peak displacement, J_1, whereas the robust controller results

in the best performance. In all performance indices, the robust controller outperforms any other controller strategy for the El Centro earthquake.

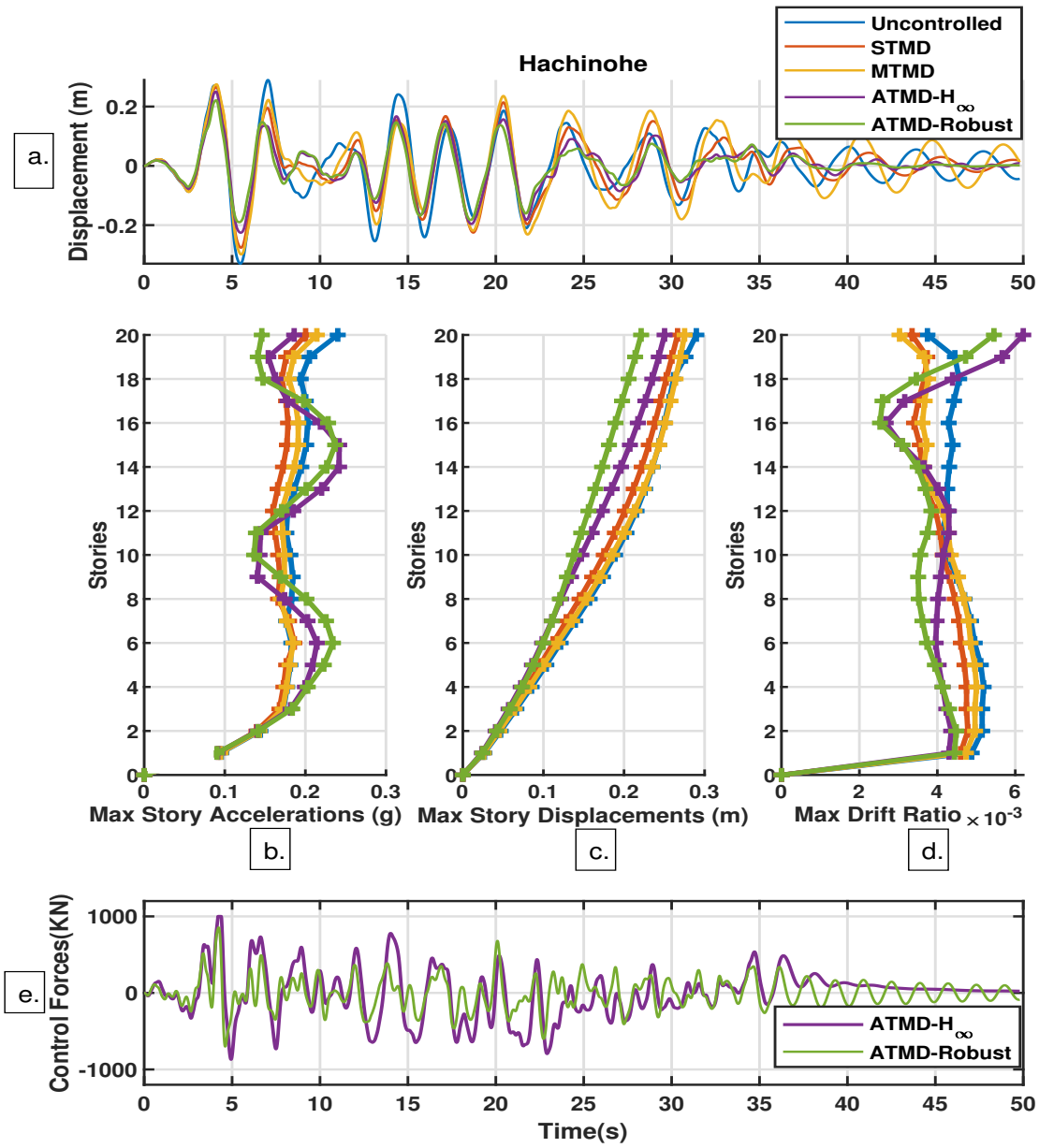

Figure 5.23. Structural responses under the Hachinohe earthquake

Similar comments can be made for the Hachinohe earthquake. In Fig. 5.23.a, the top floor responses are shown. Since the earthquake excitation ends at the 36th second, oscillatory behavior prevails. It is seen that the amplitudes decrease in all control strategies, with the robust controller outperforming the remaining controllers. Here, the vibrational response of the top-floor is almost equal to zero. When the control force di-

agram in Fig. 5.23.e is observed, it can be seen that an oscillatory control force is still applied. From here, it can be deduced that the top-floor has no displacement but the lower floors should undergo oscillatory responses.

According to Fig. 5.23.b, the structures with hybrid controllers show varying maximum acceleration values over the height of the structure. This behavior is different from the remaining control responses in which the maximum story accelerations do not show important variations over the height. Additionally, by the consideration of the maximum drift ratios in Fig. 5.23.d, in which sharp variations are present around the 16th story, it can be concluded that the hybrid controllers activate the structures' higher modes.

In Fig. 5.23.e, a biased response of the ATMD-H_∞ controlled actuator force is noted in the last seconds of simulations where it does not vary. This can be accounted for the fact that the structure yields for less than 0.1 seconds at the 4th second of the simulation according to Fig. 5.18. Although the ATMD-H_∞ control force does not oscillate in the last seconds, this is not true for the structural response. The robust ATMD controller's performance (Table. 5.2) superiority to the ATMD-H_∞ is larger than the performances with respect to the El Centro earthquake. In addition, the STMD is of better performance than the MTMD in every aspect.

Table 5.2. Hachinohe earthquake performance indices

	Uncontrolled	**STMD**	**MTMD**	**ATMD - H_∞**	**ATMD-Robust**
J_1	1.00	0.84	0.91	0.76	0.67
J_2	1.00	0.92	0.96	1.20	1.05
J_3	1.00	0.83	0.89	1.01	0.99
J_4	1.00	0.97	0.98	0.95	0.94
J_5	1.00	0.88	1.05	0.71	0.63
J_6	1.00	0.82	1.04	0.75	0.76
J_7	1.00	0.89	0.94	0.89	0.85
J_8	1.00	0.95	0.97	0.92	0.92

Fig. 5.24 shows the results for the Kobe Earthquake. Nonlinear behaviors can be noticed at the top floor displacement responses in Fig. 5.24.a because of the existing offsets. As the earthquake progresses, the structure with MTMD shows oscillatory behavior with the highest amplitudes. In contrast, the STMD results in a rather better performance among the passive controllers. The hybrid controllers drastically reduce the inter-story drifts with higher percentages compared to the TMDs for almost all stories. They also result in better responses in decreasing the peak displacements.

Fig. 5.24.e shows the control force responses. It is seen that both actuators became saturated between the 7th and 13th seconds. In addition, the ATMD-H_∞ controller is biased after the 20th second.To tackle the formed bias, a 3rd order Butter-worth high-pass filter employed. Structural yielding leads to this offset, since the H_∞ control stability margins are not capable of compensating structural nonlinear behavior.

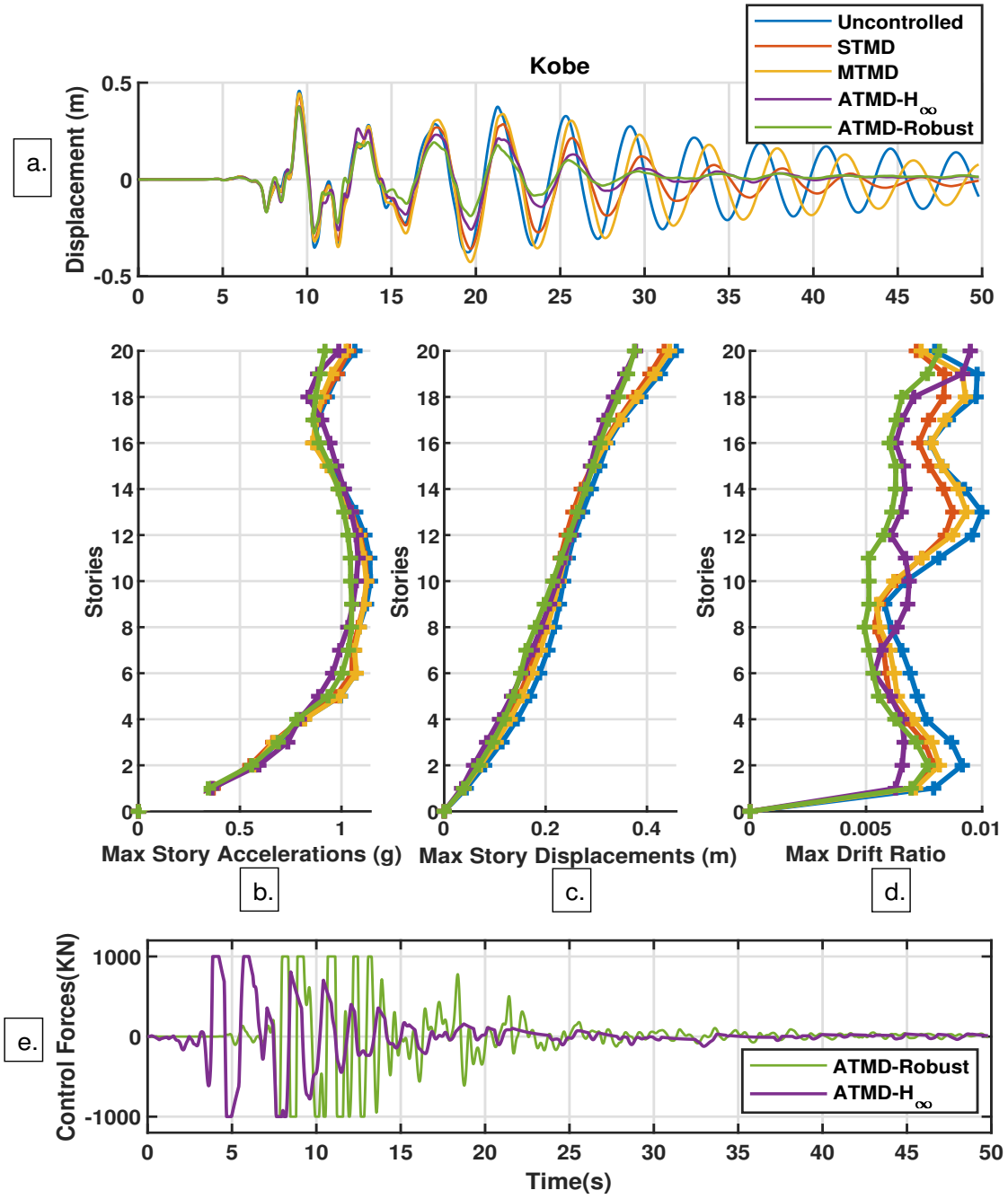

Figure 5.24. Structural responses under the Kobe earthquake

According to Table. 5.3, the hybrid controllers showed similar results in reduction of the peak displacements, while the ATMD-robust controller is of slightly better performance than the ATMD-H_∞. Besides, the lowest improvement regarding the indices was realized in the MTMD system.

Table 5.3. Kobe earthquake performance indices

	Uncontrolled	**STMD**	**MTMD**	**ATMD - H_∞**	**ATMD-Robust**
J_1	1.00	0.95	0.97	0.82	0.82
J_2	1.00	0.88	0.94	0.95	0.82
J_3	1.00	0.98	0.98	0.95	0.92
J_4	1.00	1.00	1.00	1.01	1.00
J_5	1.00	0.76	0.99	0.57	0.46
J_6	1.00	0.75	0.96	0.63	0.58
J_7	1.00	0.96	0.98	0.98	0.96
J_8	1.00	0.98	1.00	0.99	0.98

According to Table. 5.4, the ATMD-Robust controller does not put forward any superiority in the minimization of the peak displacement. However, it does show a contribution in the reduction of the energy input in the structure based on performance index, J_5.

Table 5.4. Northridge earthquake performance indices

	Uncontrolled	**STMD**	**MTMD**	**ATMD - H_∞**	**ATMD-Robust**
J_1	1.00	0.97	0.99	0.89	0.86
J_2	1.00	0.98	0.99	0.98	0.98
J_3	1.00	0.97	0.98	0.97	0.97
J_4	1.00	1.00	0.99	1.01	1.01
J_5	1.00	0.91	0.97	0.83	0.75
J_6	1.00	1.03	0.97	0.96	0.77
J_7	1.00	0.91	0.95	0.88	0.88
J_8	1.00	0.98	0.99	1.01	1.00

For the Northridge earthquake, the results and the performance indices are given in Fig. 5.25 and Table. 5.4, respectively. For this earthquake, the highest peak displacements (around 0.7m) are observed as seen in Fig. 5.25.c.

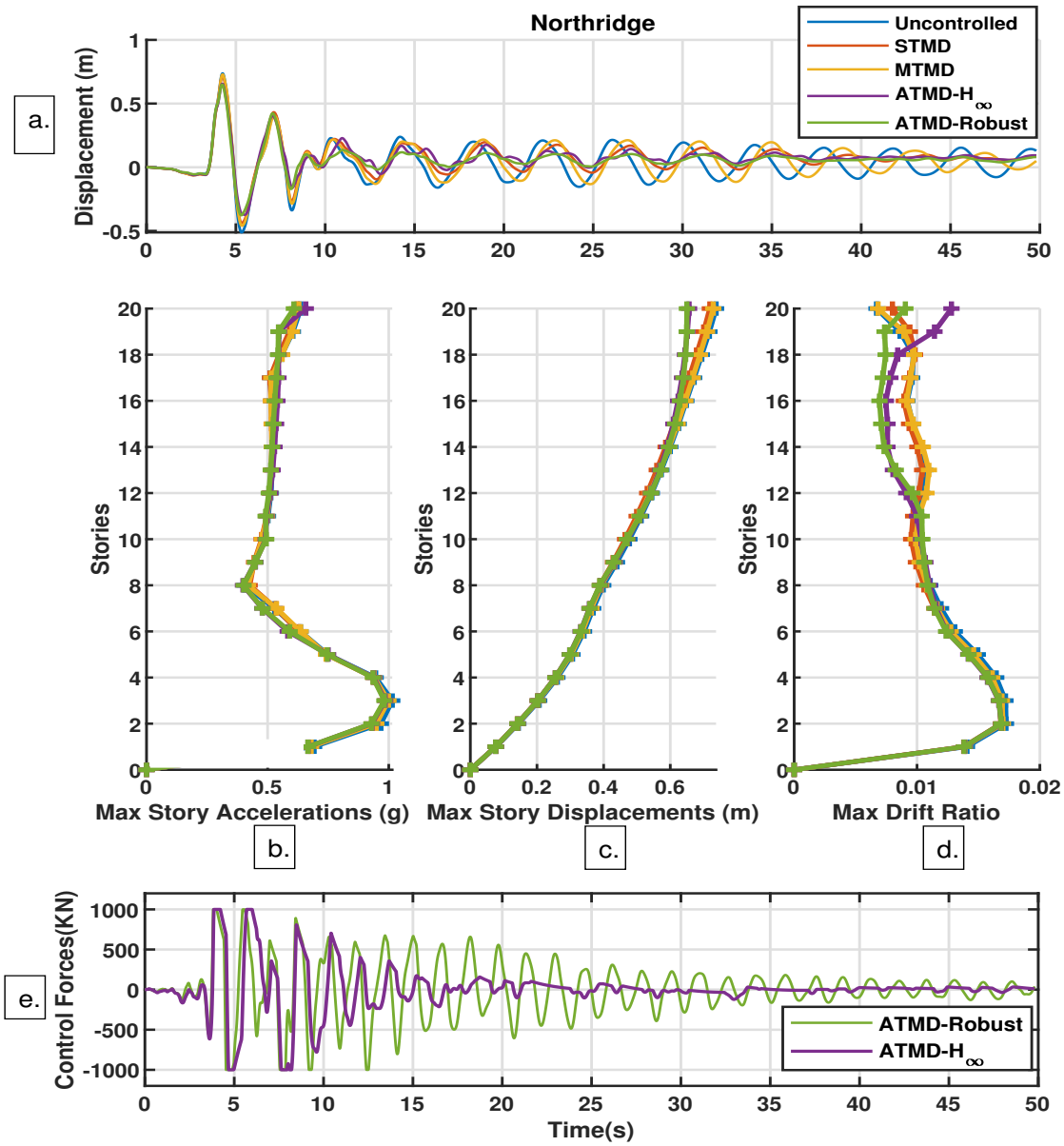

Figure 5.25. Structural responses under the Northridge earthquake

The maximum story accelerations and maximum displacements are about the same for all controller strategies. According to Fig. 5.25.a, the top story responses are quickly attenuated by the hybrid controllers.

In Fig. 5.25.d, it can be seen that the hybrid controllers result in smaller inter-story drifts above mid-height. It is also noteworthy that the hybrid controllers increase the drift ratios at the top two floors because of the existing control forces. Further, the controllers do not seem to have a significant contribution below the 12th story. The ATMD-Robust controller algorithm introduces a force offset caused by the irreversible displacements of

the structure. Such an offset was not seen in the prior earthquakes, which may indicate that the nonlinearity structural response is larger in this earthquake compared to the previous ones. The offset may have been reduced by increasing the current uncertainty range. However, when this is executed, a satisfactory achievable controller could not be reached.

CHAPTER 6

CONCLUSION

The results of each chapter were already presented. In the current section, the results will be mentioned briefly, and some concluding remarks will be drawn.

A Kalman estimator/observer design was introduced in Chapter 3. The observer was proven to be successful by the implementation of the observer-dependent controllers: LQR, PDD, PP controller algorithms. Seismic response attenuations by various control strategies were also performed in the same chapter. For a linear and nominal structural system, all applied strategies showed satisfactory results. As a passive control strategy, the FPBS resulted in the best performance among the mere control strategies. In every control implementation, the employed MRD forces went along with the actuator forces. It was also observed that the MRD could not produce the peak value of the actuator because of the low-velocity values. Besides, the hybrid controllers could not outperform the single controllers by huge differences and showed small improvements in the performances. The designed passive controllers were already optimum and it is not applicable in theory to improve their performance by large differences.

In Chapter 4, the 3-story shear frame with model parameter uncertainties was aimed to control. For this purpose, the civil structure was modeled as uncertain in reasonable ranges regarding mass, stiffness, and damping. The nominal and worst-case uncertainty models were chosen to verify the designed controllers, based on H_∞ norm. It was observed that the controller reduces the response of the structure. However, the mere H_∞ controller's performances were not as satisfactory as expected. Besides, it amplified the oscillating responses and led the structure to fail.

A robust controller was designed by μ synthesis for selected possible perturbations, and it covers all perturbations. It was observed that the proposed μ controller could be a solution to stabilize the structure that has parametric uncertainties.

In Chapter 5, two different tuned mass dampers (TMDs), single-, and multi-TMDs, for a nonlinearly modeled benchmark structure were presented. The effectiveness of these two TMDs was investigated. Accordingly, a hybrid controller device, composed of a passive TMD and an active controller, was introduced. The conclusions below are drawn under the light of the performed numerical study in this part of the thesis;

a) The current benchmark building undergoes yielding during simulations with

the selected earthquake records. Therefore, the nonlinear model must be employed.

b) The MTMD installed nonlinear benchmark model has not been found to exhibit robust performance under the corresponding earthquakes.

c) The ATMD-H_∞ controller operates well even if the structure does enter the nonlinear region since it has relatively wide stability margins. The actuator, however, may become saturated and therefore consuming large amounts of energy.

d) The ATMD-Robust controller outperforms other presented controllers and pushes the STMD back to the optimum performance zone.

e) Installing either an STMD or ATMD always results in better responses than the uncontrolled structure.

f) The installed ATMDs provide limited performance since the maximum control force is limited by the story shear force capacity of the structure.

CHAPTER 7

NOVELTIES

In this study, the following novelties are put forward:

-A new approach to cope with structural nonlinearities in the control design is developed. Accordingly, the uncertainty ranges can be determined so that the designer models the controller for more likely hazards in practice.

-A new hybrid robust control technique for TMDs is developed to replace passive robust control approaches composed of several TMDs having different optimum characteristics. All MTMDs can be modeled according to linear system model parameters to get highest decrement in the frequency response, and the robust controller can tune them during the earthquake. This method can be used to enhance any passive control device performance.

CHAPTER 8

FUTURE WORK

Different possible ways exist as future work for the current study. First of all, an MRD that can produce higher forces in amplitude can be employed, or such a system can be aimed. These required forces can be achieved through higher voltage values, but this should be tested first experimentally.

Among the passive controllers, the TMDs are very sensitive to the structure modal parameters. Any change during an earthquake may diverge its efficiency drastically. For this reason, a robust implementation that depends on a bandwidth frequency, not a single frequency value, can be put forward.

The robust control computational cost is too large because of the uncertainties in the model parameters. It can be improved in a way that the designer checks the nonlinear performance of the civil structure and locates the members where yielding occurs. Accordingly, uncertainties can exist in those members instead of all of the members.

A large-scale MRD can be substituted for the employed actuator since actuators require large external power supplies. Besides, the number of control devices might be increased so that the neighboring floor shear forces occurred by the control devices are decreased.

APPENDICES

APPENDIX A

KALMAN OBSERVER

```
%%%%%%%%%%%%%%%%%%%%%%%%%%%%%%%%%%%%%%%%%%%%%%%%%%%%%%%%%%%%%%%%%%%%%%%%%%%%%%%%
%%%%% Kalman Observer for 3-Story Mockup structure %%%%%
%%%%%%%%%%%%%%%%%%%%%%%%%%%%%%%%%%%%%%%%%%%%%%%%%%%%%%%%%%%%%%%%%%%%%%%%%%%%%%%%
%Author: Senol, Vedat
%created: 4.2018, updated: 12.2020
close all; clearvars; clc
%%MODAL PARAMETERS
3_model_story.m
gama  = [1 0 0]'; % Control Input Location Vector
gama_d= [1 1 1]'; % Disturbance Excitation Vector
n=length(gama);
%State Space Matrices
% dotx = Ax  + B1w + B2u
%    z = C1x + D12u      exegenous outputs
%   ym = C2x + D21w      measured outputs
A=[zeros(3,3) eye(3,3)
        -M\K      -M\C];
B1=[zeros(3,1)
    M\gama];
B2=[zeros(3,1)
    -gama_d ];
C1=[ 1  0  0  0 0 0; 0  1  0  0 0 0; 0  0  1  0 0 0];
D =  [0 0;0 0;0 0];
%% Kalman Observer
Plant = ss(A,[B1 B2],C1,0,0.02,'inputname',{'u' 'w'},'outputname','y');
Q = 1e1*eye(3,3); R = 1e5; N = zeros(3,6);
[kalmf,L,~,Mo] = kalman(Plant,Q,R,N);
Mo; % Updating matrix (Deshpande,2017)
%% Parallel modeling
a = A; b = [B1 B2 0*B1]; c = [C1;C1];
d = [0 0 0; 0 0 0; 0 0 0; 0 0 1; 0 0 1; 0 0 1];
P = ss(a,b,c,d,-1,'inputname',{'u' 'w' 'v'},'outputname',{'y(1)' 'y(2)'
    'y(3)' 'yv(1)' 'yv(2)' 'yv(3)'});
```

```
sys = parallel(P,kalmf,1,1,[],[]); feedin=[4 5 6]; feedout=[4 5 6];
SimModel = feedback(sys,eye(3,3),feedin,feedout,1);    % Close loop
    around input #4 and output #2
SimModel = SimModel([1 2 3 7:15],[1 2 3]);
SimModel.InputName
SimModel.OutputName
%% Loading Disturbances
dt=0.02;
load elcentro
w = eq(2,:)';          % Earthquake Disturbances
t = eq(1,:)';          % Time Array 50Hz 50sn
lg=length(w);
u=zeros(1,lg)';
v = sqrt(R)*randn(lg,1);% additive white gaussian noise
v = 1e-4*radn(1,lg)';
inp=[u,w];
%% Simulate the responses.
[out,~] = lsim(SimModel,[w,v,u]);

y = out(:,1:3);    % true response
ye = out(:,4:6);  % filtered response
yv = y + v*[5 3 2];       % measured response

Pu=ss(A,B2,C1,D(:,1));          % Uncontrolled System State Space Matrix
[y,~,x]=lsim(Pu,w,t);         % Uncontrolled System Accelaritons
%% Controlled Structure Linear Simulations
Acl= A-B1*Kcc;                % Lqr Controlled Closed Loop System
Pc=ss(Acl,B2,C1,D(:,2));          % Controlled System State Space Matrix
[yc,t,xc]=lsim(Pc,w,t);      % Controlled System Accelaritons
Fc=(-Kcc*xc')';
%% MRD Inputs
Vmax=3;                       %Max Voltage
%% MRD Controlled Plant Linear Simulations
% Acl= A-B2*Kcc;              % Lqr Controlled Closed Loop System
% Pc=ss(Acl,B1,C1,D);         % Controlled System State Space Matrix
% [yc,t,xc]=lsim(Pc,w,t); % Controlled System Responses
V=zeros(lg,1);              % Pre-allocated Voltage Values
F_mrd=zeros(lg,1);          % Pre-allocated MRD Force Values (Obtained form
    MRD)
```

```
x0=zeros(size(A,1),1);
B3=[B1 B2];
D2=[D zeros(3,1)];
Pcmrd=ss(A,B3,C1,D);      % MRD Controlled System State Space Matrix
xcf=zeros(lg,6);          % Pre-allocated MRD Controlled States
xk=zeros(lg,6);           % Pre-allocated MRD Observer States
Fcmrd=zeros(lg,1);        % Pre-allocated MRD Controlled Optimum Forces (
    Required)
ycf=zeros(lg,3);          % MR Damper-controlled system outputs
yk=zeros(lg,9);           % Kalman observer system outputs
yv=zeros(lg,3);           % Noise
warning('OFF','ALL')
for i=2:lg
      F_mrd(i)=0; % Using as a keyboard
      Wfmrd=[F_mrd((i-1):i),w((i-1):i)];
      [ycf(i-1:i,:),~,xcf(i-1:i,:)]=lsim(Pcmrd,Wfmrd,t((i-1):i),xcf(i
          -1,:));
      ... Controlled System Inter-story Drifts
      %Kalman Filter
      yv(i-1:i,:)=ycf(i-1:i,:)+v(i-1:i,:);
      Wkalm=[F_mrd((i-1):i),yv(i-1:i,:)]';
      [yk(i-1:i,:),~,xk(i-1:i,:)]=lsim(kalmf,Wkalm,t((i-1):i),xk(i-1,:))
          ;
      % Observer outputs given to the controller
      Fcmrd(i)=-Kcc*yk(i,4:9)';
end
warning('ON','ALL')
yt = xcf(:,3);   % true response
ye = yk(:,3);  % filtered response
yv;      % measured response
MeasErr = ycf(:,3)-yv(:,3);
MeasErrCov = sum(MeasErr.*MeasErr)/length(MeasErr);
% The error covariance after filtering (estimation error) is reduced:
EstErr = yt-ye;
EstErrCov = sum(EstErr.*EstErr)/length(EstErr);
```

APPENDIX B

LINEAR QUADRATIC REGULATOR (LQR)

```
%%%%%%%%%%%%%%%%%%%%%%%%%%%%%%%%%%%%%%%%%%%%%%%%%%
%%%%% LQR Displacement  Controller for Lab Model  %%%%%
%%%%%%%%%%%%%%%%%%%%%%%%%%%%%%%%%%%%%%%%%%%%%%%%%%
%Author: Senol, Vedat
%created: 12.2017, updated: 12.2020
close all; clearvars; clc
Kalman_observer.m
%% Optimum Controller Gains
Qlqr = 1e0*[5e1*eye(n,n) zeros(n,n)
            zeros(n,n) eye(n,n)];
Nlqr = zeros(2*n,1);
Rlqr = 1e-8;
[Kcc,~,~] = lqr(A,B1,Qlqr,Rlqr,Nlqr);

%% Uncontrolled Structure Linear Simulations
Pu=ss(A,B2,C1,D(:,1));          % Uncontrolled System State Space Matrix
[y,~,x]=lsim(Pu,w,t);           % Uncontrolled System Displacements
%% Controlled Structure Linear Simulations
Acl= A-B1*Kcc;                  % Lqr Controlled Closed Loop System
Pc=ss(Acl,B2,C1,D(:,2));        % Controlled System State Space Matrix
[yc,t,xc]=lsim(Pc,w,t);         % Controlled System Displacements
Fc=(-Kcc*xc')';
%% MRD Inputs
Vmax=3;                         %Max Voltage
Fmax=3000;                      % Max Force N
%% MRD Controlled Plant Linear Simulations
% Acl= A-B2*Kcc;                % Lqr Controlled Closed Loop System
% Pc=ss(Acl,B1,C1,D);           % Controlled System State Space Matrix
% [yc,t,xc]=lsim(Pc,w,t);       % Controlled System Displacements
V=zeros(lg,1);                  % Pre-allocated Voltage Values
F_mrd=zeros(lg,1);              % Pre-allocated MRD Force Values (Obtained from
    MRD)
B3=[B1 B2];
```

```
D2=[D zeros(3,1)];
Pcmrd=ss(A,B3,C1,D);      % MRD Controlled System State Space Matrix
xcf=zeros(lg,6);          % Pre-allocated MRD Controlled States
xk=zeros(lg,6);           % Pre-allocated Kalman States
Fcmrd=zeros(lg,1);        % Pre-allocated MRD Controlled Optimum Forces (
    Required)
ycf=zeros(lg,3);          % MR Damper-controlled system outputs
yk=zeros(lg,9);           % Kalman observer system outputs
yv=zeros(lg,3);           % Kalman observer system noise
warning('OFF','ALL')
for i=2:lg
      F_mrd(i) = ...
      -Mr_fluid_Damper_hysteresis_function(0.0002,xcf(i-1,1),xcf(i-1,4),
          V(i-1));
      Wfmrd=[F_mrd((i-1):i),w((i-1):i)];
      [ycf(i-1:i,:),~,xcf(i-1:i,:)]=lsim(Pcmrd,Wfmrd,t((i-1):i),xcf(i
          -1,:));
      ... Controlled System Inter-story Drifts
      %Kalman Filter
      yv(i-1:i,:)=ycf(i-1:i,:)+v(i-1:i,:); % Measurements
      Wkalm=[F_mrd((i-1):i),yv(i-1:i,:)]';
      [yk(i-1:i,:),~,xk(i-1:i,:)]=lsim(kalmf,Wkalm,t((i-1):i),xk(i-1,:))
          ;
      % Observer outputs given to the controller
      Fcmrd(i)=-Kcc*yk(i,4:9)';
      if Fcmrd(i)>=Fmax
          Fcmrd(i)=Fmax;
      elseif Fcmrd(i)<=-Fmax
          Fcmrd(i)=-Fmax;
      end
      % MRD Voltage
      V(i) = Mr_fluid_Damper_voltage_function( F_mrd(i),Fcmrd(i),Vmax );
%       V(i) = 0;
end
warning('ON','ALL')
```

APPENDIX C

H_2 & H_∞ CONTROLLER

```
%%%%%%%%%%%%%%%%%%%%%%%%%%%%%%%%%%%%%%%%%%%%%%%%%%%%%%%%%%%%%%
%%%%     Hinf Controller for 3-story Lab Model     %%%%%
%%%%%%%%%%%%%%%%%%%%%%%%%%%%%%%%%%%%%%%%%%%%%%%%%%%%%%%%%%%%%%
%Author: Senol, Vedat
%created: 10.2018, updated: 12.2020
close all; clearvars; clc
%% This script includes weights and Generalized Delta-P-K like plant
Weights_and_Generalized_Plant
%% Loading Disturbances
dt=0.02;
load elcentro
w = eq(2,:)';          % Earthquake Disturbances
t = eq(1,:)';          % Time Array 50Hz 50sn
lg=length(w);
u=zeros(1,lg)';
v = sqrt(R)*randn(lg,1);% AWGN
v = 1e-4*radn(1,lg)';
inp=[u,w];
% Uncontrolled Nominal Structure Linear Simulations
Pu=CSP.Nominal;          % Uncontrolled System State Space Matrix
[yn,~,x]=lsim(Pu,inp,t);     % Uncontrolled System Accelaritons
%% Hinf synthesis
nmeas=3;
ncon=1;
gamTry=0.1;
% gamRange=[gmin gmax];
opts = hinfsynOptions('Display','on');
% % system control gains
[Knsinf,CLnsinf,ginfns] = hinfsyn(CSPns,nmeas,ncon,gamTry,opts) ;
hinfnorm(Knsinf)
%% General Plant Simulations without Wg
% Input Channels
xgdd = icsignal(1);    % EQ acceleration disturbance
```

```
v = icsignal(4);        % Noise disturbance
u = icsignal(1);        % Control input
% Output Channels
y =  icsignal(4);         % Measurement channel
% Assembling of Nominal Generalized Plant
Pns = iconnect;
Pns.Input = [xgdd; v; u];
ug=xgdd;
Pns.Equation{1} = equate(y,CSP.Nominal*[u;ug]);
n=Wn*v;
Pns.Output = [Wp*y(2:4); Wu*u; y+n];
CSPns1=(Pns.System);
%% MRD Inputs
Vmax=3;                    %Max Voltage
Fmax=3000;                 % Max Force N
%% MRD Controlled Plant Linear Simulations
V=zeros(lg,1);             % Pre-allocated Voltage Values
F_mrd=zeros(lg,1);         % Pre-allocated MRD Force Values (Obtained form
    MRD)
Pcmrd=CSPns1;              % MRD Controlled System State Space Matrix
xcf=zeros(lg,length(Pcmrd.A));          % Pre-allocated MRD Controlled
    States
x0=zeros(size(Pcmrd.A,1),1);
Fcmrd=zeros(lg,1);         % Pre-allocated MRD Controlled Optimum Forces (
    Required)
ycf=zeros(lg,length(Pcmrd));
yk=zeros(lg,10);
xk=zeros(lg,length(kalmf.A));
Fx=zeros(lg,length(Knsinf.A));
for i=2:lg
    F_mrd(i) = ...
        -Mr_fluid_Damper_hysteresis_function( 0.00002, ycf(i-1,6), ycf(
            i-1,5), V(i-1));
    Wfmrd=[w((i-1):i),v((i-1):i,:),F_mrd((i-1):i)];
    [ycf(i-1:i,:),~,xcf(i-1:i,:)]=lsim(Pcmrd,Wfmrd',t(i-1:i),xcf(i-1,:)
        );
    % Kalman Filter
    Wkalm=[F_mrd((i-1):i),ycf(i-1:i,5:8)]';
    [yk(i-1:i,:),~,xk(i-1:i,:)]=lsim(kalmf,Wkalm,t((i-1):i),xk(i-1,:));
```

```
    % Observer outputs given to the controller
    [ Fcmrd(i-1:i),~,Fx(i-1:i,:)]=lsim(Knsinf,ycf(i-1:i,6:8),t(i-1:i),
        Fx(i-1,:));
    if Fcmrd(i-1)>= Fmax
        Fcmrd(i-1)= Fmax;
    elseif Fcmrd(i-1)<=-Fmax
        Fcmrd(i-1)=-Fmax;
    end
    % MRD Voltage
    V(i) = Mr_fluid_Damper_voltage_function( F_mrd(i),Fcmrd(i),Vmax );
     if V(i)>= 3
        V(i)= 3;
    end
end
```

APPENDIX D

UNCERTAIN MODELING

```
%% MODEL PARAMETERS
%Author: Senol, Vedat %created: 10.2018, updated: 12.2020
% Uncertainity ratios
Pm = 0.2; Pc = 0.6; Pk = 0.2; Pu = 0;
%Uncertainties
delta_m1 = Pm*ureal('delta_m1',0);
delta_m2= Pm*ureal('delta_m2',0);
delta_m3 = Pm*ureal('delta_m3',0);
delta_c1 = Pc*ureal('delta_c1',0);
delta_c2 = Pc*ureal('delta_c2',0);
delta_c3 = Pc*ureal('delta_c3',0);
delta_k1 = Pk*ureal('delta_k1',0);
delta_k2 = Pk*ureal('delta_k2',0);
delta_k3 = Pk*ureal('delta_k3',0);
m=200; %kg
 Ms=[m*(1+delta_m1) 0 0
      0 m*(1+delta_m2) 0
      0 0 m*(1+delta_m3)];
k = 156250;%N/m
Ks = [ k*(2+delta_k1+delta_k2)      -k*(1+delta_k2)                  0   %
    Stiffness
          -k*(1+delta_k2)  k*(2+delta_k2+delta_k3)     -k*(1+delta_k3)
                    0     -k*(1+delta_k3)          k*(1+delta_k3)   ];
Cs =      [ 61.76+0.5*61.76*(delta_c1+delta_c2)     -18.20*(1+delta_c2)
                    0
             -18.20*(1+delta_c2)      61.02+0.5*61.02*(+delta_c2+delta_c3)
                      -18.20*(1+delta_c3)
                           0       -18.20*(1+delta_c3)       42.70*(1+
                                delta_c3)]; %Ns/m
gama  = [1 0 0]'; % Control Input Location Vector
gama_d= [1 1 1]'; % Disturbance Excitation Vector
n=length(gama);
%% State Space Represantation
```

```
% dotx =  Apx   +     B1pu  +   B2pw
%     y =  Cpx   +     D1pu  +   D2pw
%% State-Space Matrices
Ap=[zeros(n,n) eye(n,n)
        -Ms\Ks      -Ms\Cs];
B1p=[zeros(n,1)
        Ms\gama   ];
B2p=[zeros(n,1)
         -gama_d   ];
Bp=[B1p B2p];
Cp = [   0   0  0  1  0  0
         1   0  0  0  0  0
        -1   1  0  0  0  0
         0  -1  1  0  0  0];
D1p = zeros(1,4)'; D2p = zeros(1,4)'; Dp=[D1p D2p];
CSP = ss(Ap,Bp,Cp,Dp);
```

APPENDIX E

WEIGHTS

```
%%%%%%%%%%%%%%%%%%%%%%%%%%%%%%%%%%%%%%%%%%
%%%%%%%%% Weights for 3-story Lab Model%%%%%%%%%%
%%%%%%%%%%%%%%%%%%%%%%%%%%%%%%%%%%%%%%%%%%
%% This scripts includes weights and Generalized Delta-P-K like plant
%% LFT
 %Author: Senol, Vedat
%created: 10.2018, updated: 12.2020
 % The outputs which are aimed;
 % M          : System matrix which was freed from uncertainty
 % Delta      : Pulled out uncertainty block matrix
 % BlkStruct  : Structured block of uncertainty matrix
 Model
 [M,Delta,BlkStruct] = lftdata(CSP);
 [wcg,wcug] = wcgain(CSP);
 CSPwst = usubs(CSP,wcug);
%% Weights
% Output performance weight
Wp=1e2*diag([5 1 1]);
% Control input weight
Wu=5e-4;
% Excitation weight Tajimi Spectrum
So=0.09; wg=8.65; zetag=0.25; Wg=1;
Wg=tf(So^(0.5)*[2*zetag*wg wg^2],[1 2*zetag*wg wg^2]);
% Noise Weight
Wn=makeweight(10,1000,0.01);
Wnk=1e-6; Wn=Wn*Wnk;
% Wn= ellipfilt(1, 1.1 ,20, 100*2*pi);
%% General Plant Assembly
%    dotx = Apx   +  B1pw  +  B2pu
% deltay = C1px  +  D11pw +  D12pu
%       z = C2px  +  D21pw +  D22pu
%       y = C3px  +  D31pw +  D32pu
% where z = [Wp*y; Wp*u],
```

```
%        w = [xgdd;v]
% Input Channels
pertu = icsignal(9); % Uncertinty perturbations
xgdd = icsignal(1);    % EQ acceleration disturbance
v = icsignal(4);       % Noise disturbance
u = icsignal(1);       % Control input
% Output Channels
deltay = icsignal(9);  % Uncertainties
y =  icsignal(4);        % Measurement channel
% Assemblying
P = iconnect;
P.Input = [pertu; xgdd; v; u];
ug=Wg*xgdd;
P.Equation{1} = equate([deltay;y],M*[pertu;u;ug]);
n=Wn*v;
P.Output = [deltay; Wp*y(2:4); Wu*u; y+n];
GP=(P.System); %Generalized Plant
%% General Plant Simulations
% Assembling of Generalized Plant
GP = iconnect;
GP.Input = [xgdd; v; u];
ug=Wg*xgdd;
GP.Equation{1} = equate(y,CSP*[u;ug]);
n=Wn*v;
GP.Output = [Wp*y(2:4); Wu*u; y+n];
GP=(GP.System);
% Assembling of WC Generalized Plant
Pwc = iconnect;
Pwc.Input = [xgdd; v; u];
ug=Wg*xgdd;
Pwc.Equation{1} = equate(y,CSPwst*[u;ug]);
n=Wn*v;
Pwc.Output = [Wp*y(2:4); Wu*u; y+n];
CSPwc=(Pwc.System);
% Assembling of Nominal Generalized Plant
Pns = iconnect;
Pns.Input = [xgdd; v; u];
ug=Wg*xgdd;
Pns.Equation{1} = equate(y,CSP.Nominal*[u;ug]);
```

```
n=Wn*v;
Pns.Output = [Wp*y(2:4); Wu*u; y+n];
CSPns=(Pns.System);
hinfnorm(CSPns); hinfnorm(Wg)
```

APPENDIX F

ROBUST CONTROLLER

```
%% Robust controller for 3-storey Lab model
%Author: Senol, Vedat
%created: 4.2019, updated: 12.2020
close all; clearvars; clc
%% This scripts includes weights and Generalized Delta-P-K like plant
Weights_and_Generalized_Plant
%% Mu-synthesis
nmeas=3;
ncon=1;
% opt=dksynOptions('FrequencyVector',logspace(-2,3,80),'
    AutoIterSmartTerminate','on','AutoIterSmartTerminateTol',0.01)
% [Kdk,CLdk,CLPERF] = musyn(GP,nmeas,ncon,opt);
[Kdk,CLdk,CLPERF] = musyn(GP,nmeas,ncon);
%% General Plants Simulations without Wg
% Nominal System
% Input Channels
xgdd = icsignal(1);    % EQ acceleration disturbance
v = icsignal(4);       % Noise disturbance
u = icsignal(1);       % Control input
% Output Channels
y =  icsignal(4);        % Measurement channel
% Assembling of Nominal Generalized Plant
Pns = iconnect;
Pns.Input = [xgdd; v; u];
ug=xgdd;
Pns.Equation{1} = equate(y,CSP.Nominal*[u;ug]);
n=Wn*v;
Pns.Output = [Wp*y(2:4); Wu*u; y+n];
CSPns1=(Pns.System);
% Worst-Case System
% Input Channels
xgdd = icsignal(1);    % EQ acceleration disturbance
v = icsignal(4);       % Noise disturbance
```

```
u = icsignal(1);        % Control input
% Output Channels
y =  icsignal(4);        % Measurement channel
% Assembling of Worst-Case Generalized Plant
Pns = iconnect;
Pns.Input = [xgdd; v; u];
ug=xgdd;
Pns.Equation{1} = equate(y,CSPwst*[u;ug]);
n=Wn*v;
Pns.Output = [Wp*y(2:4); Wu*u; y+n];
CSPwc1=(Pns.System);

% Robust Stability Analysis with M-Delta structure
N=star(GP,Knsinf);
szDelta = size(Delta);
M_g = N(1:szDelta(2),1:szDelta(1));
M_g = N(1:szDelta(2),1:szDelta(1));
omega = logspace(-3,3,100);
M_g = frd(N(1:5,1:5),omega);
mubnds = mussv(M_g,BlkStruct,'s');
figure()
LinMagopt = bodeoptions;
LinMagopt.PhaseVisible = 'off';
LinMagopt.XLim = [1e-1 1e2];
LinMagopt.MagUnits = 'abs';
bodeplot(mubnds(1,1),mubnds(1,2),LinMagopt);
xlabel('Frequency (rad/sec)');
ylabel('Mu upper/lower bounds');
title('Mu plot of robust stability margins (inverted scale)');
[pkl,wPeakLow] = getPeakGain(mubnds(1,2));
[pku] = getPeakGain(mubnds(1,1));
SMfromMU.LowerBound = 1/pku;
SMfromMU.UpperBound = 1/pkl;
SMfromMU.CriticalFrequency = wPeakLow;
```

APPENDIX G

VOLTAGE FUNCTION (MODIFIED CLIPPED ALGORITHM)

```
%MR Fluid Dampers Hysteresis Loop Cycle Modified Bouc-Wen Model

function [ V ] = Mr_fluid_Damper_voltage_function( F_mrd,u,Vmax)

maxF_mrd=4448;
if abs(u)<= maxF_mrd
    Vref=u*Vmax/maxF_mrd;
elseif abs(u)> maxF_mrd
    Vref=Vmax;
end

V=Vref*heaviside((u-F_mrd)*F_mrd);
V=abs(V);
end
```

APPENDIX H

BOUC-WEN HYSTERESIS FUNCTION

```
%MR Fluid Dampers Hysteresis Loop Cycle Modified Bouc-Wen Model
function [ F_mrd ] = Mr_fluid_Damper_hysteresis_function( dt,x,xd,V )
close all
clc
%% Defining the constant coefficients

c0a=2100;                   % Ns/m
c0b=350;                    % Ns/mV
c1a=28300;                  % Ns/m
c1b=295;                    % Ns/mV
k0 =4690;                   % N/m
k1 =500;                    % N/m
x00=0.143;                  % m
% x00=0;                      % m
alfa_a=14000;               % N/m
alfa_b=69500;               % N/mV
gama=3630000;               % m^-2
beta=3630000;               % m^-2
A=301;                      %
n=2;                        % Modal parameter
nu=190;                  % s^-1 (Hz)
% fo=0;                       % Offset force
Fmax=3000;
%% Defining of the displacement and velocity as a functions
%Construction of loop
eps_=0.0000000001;              %error
nx=length(x);
y=zeros(1,nx);
yd=zeros(1,nx);
F_mrd=zeros(1,nx);
Va=zeros(1,nx);
% keyboard
```

```
for j=1:nx
    s=0;                    %initial s for using at loop
    nn=1000;
    ds_=zeros(1,nn);
    for i=1:nn
        ds_(i)= -gama*abs(xd(j)-yd(j))*s*abs(s)^(n-1)...
            - beta*(xd(j)-yd(j))*abs(s)^(n)+A*(xd(j)-yd(j));
        s=s+ds_(i)*dt/nn;
        dVa=zeros(1,nn);
        for k=1:nn
            dVa(k)=-nu*(Va(j)-V);
            Va(j)=Va(j)+dVa(k)*dt/nn;
            if((k>1) && (abs(dVa(k)-dVa(k-1)) < abs(eps_)))
                break;
            end
        end

        alfa=alfa_a + alfa_b*Va(j);
        c0= c0a+c0b*Va(j);
        c1= c1a+c1b*Va(j);
        yd(j)= (alfa*s+c0*xd(j)+k0*(x(j)-y(j)))/(c0+c1);
        y(j)=y(j)+yd(j)*dt/nn;

        if((i>1) && (abs(ds_(i)-ds_(i-1)) < abs(eps_)))
            break;
        end
    end
    % Calculating of desired force
    F_mrd(j)=alfa*s+c0*(xd(j)-yd(j))+k0*(x(j)-y(j))+k1*(x(j)-x00);
end
end
```

APPENDIX I

ROBUST CONTROL OF THE 20-STORY NONLINEAR MODEL

```
#####################################################################
## 2D steel frame.
## 20 story steel building with rigid beam-column connections.
## This script uses W-section command in Opensees to create steel..
## .. beam-column fiber sections.
##
## By - Vedat SENOL, PhD Candidate, Iztech.
## Date - 21/09/2020
#####################################################################
#import sys
#sys.modules[__name__].__dict__.clear()

print("============================================================")
print("Loading 20-storey Benchmark Model")
from openseespy.opensees import *
import matlab.engine
eng = matlab.engine.start_matlab()
import numpy as np
import matplotlib.pyplot as plt
import os
import math

#os.chdir("C:\Users..")
runfile('20storeybenchmarkNonlinear_TMD.py')
########################################
#####          DAMPING             #####
########################################
# calculate eigenvalues & print results
freq2 = eigen('-fullGenLapack', 10)
freq=np.float_power(freq2[0], 0.5)
freq=float(freq)/2/pi
omega=math.pow(freq2[0], 0.5)
```

```
dampRatio = 0.02
rayleigh(0, 0, 0, float(2*dampRatio/omega))
print("eigen values at start of transient:",freq)

########################################
#####        EARTHQUAKE SETUP       #####
########################################

# Set some parameters
record = 'Northridge'
dt=0.02
# Set time series to be passed to uniform excitation
timeSeries('Path', 1, '-filePath', record+'.txt', '-dt', dt, '-factor',
    1)
# Create UniformExcitation load pattern
pattern('UniformExcitation', 1, 1, '-accel', 1)
# EQ data load
wnn = np.loadtxt("Northridge.txt", delimiter=',')

########################################
#####           ANALIZ SETUP        #####
########################################
# Delete the old analysis and all it's component objects
wipeAnalysis()

# Create the system of equation, a banded general storage scheme
system('␣FullGeneral')

# Create the constraint handler, a plain handler as homogeneous
    boundary
constraints('Plain')

# Create the convergence test, the norm of the residual with a
    tolerance of
# 1e-12 and a max number of iterations of 10
test('NormDispIncr', 1.0e-8, 10 )

# Create the solution algorithm, a Newton-Raphson algorithm
algorithm('Newton')
```

```
# Create the DOF numberer, the reverse Cuthill-McKee algorithm
#numberer('Plain')
numberer('Plain')

# Create the integration scheme, the Newmark with alpha =0.5 and beta
    =.25
integrator('Newmark', 0.5, 0.25 )

# Create the analysis object
analysis('Transient')

######################################
####          RECORDERS           #####
######################################
story_nodes = np.linspace(1,180, 180)
tmd_node=301
obsv_nds = [21, 33, 39, 45, 57, 63, 69, 81, 87, 93, 105, 111, 117, 129,
     135, 141, 153, 159, 171, 177, 301];

######################################
#####             ANALYZE          #####
######################################
# set some variables
nPts=len(wnn)
x = np.zeros((nPts,3*len(story_nodes)))
v = np.zeros((nPts,3*len(story_nodes)))
a = np.zeros((nPts,3*len(story_nodes)))

xo = np.zeros((nPts,len(obsv_nds)))
vo = np.zeros((nPts,len(obsv_nds)))
ao = np.zeros((nPts,len(obsv_nds)))

h = np.zeros(3*len(story_nodes))
xdr = np.zeros((nPts,3*len(story_nodes)))
Fdy = np.zeros((nPts,3*len(story_nodes)))
FREQQ = np.zeros((nPts,5))
FREQ = np.zeros((nPts,5))
Fx = np.zeros((nPts,127))
```

```
Fc = np.zeros((nPts,))
Vc = np.zeros((nPts,))
ycf = np.zeros((nPts,len(obsv_nds))) # prefilled array
tFinal = nPts*dt
ok = 0
tCurrent = getTime()
time = [tCurrent]



# Perform the transient analysis
for i in range(1,int(nPts)):

 # Fc
    tCurrent = getTime()
    time.append(tCurrent)
    if i>4:
        valuesF = Fc[i-4] # 0.06 sec delay added
        time0 = time[i]
        time0 = float(time0)
        time1 = time[i]+dt
        time1 = float(time1)
        timeSeries('Rectangular', i, time0, time1, '-factor', 1)
#
        loadvalues1 = [-valuesF, 0, 0]
        loadvalues2 = [valuesF, 0, 0]
        pattern('Plain', i, i)
        load(178, *loadvalues1)
        load(301, *loadvalues2)
    ok = analyze(1, dt)
    if i>3:
         remove('loadPattern', i-2)
         remove('timeSeries', i-2)
    # if the analysis fails try initial tangent iteration
    if ok != 0:
        print("regular newton failed .. lets try an initail stiffness
           for this step")
        test('NormDispIncr', 1.0e-8,  10)
        algorithm('ModifiedNewton', '-initial')
```

```
        ok =analyze(1, dt)
        if ok == 0:
            print("that worked .. back to regular newton")
        test('NormDispIncr', 1.0e-8, 10 )
        algorithm('Newton')

#         Outputs
    for k in range(1,181):
        x[i,3*(k-1)] = nodeDisp(story_nodes[k-1],1)
        v[i,3*(k-1)] = nodeVel(story_nodes[k-1],1)
        a[i,3*(k-1)] = nodeAccel(story_nodes[k-1],1)

    for k in range(0,len(obsv_nds)):
        xo[i,(k)] = nodeDisp(obsv_nds[(k)],1)
        vo[i,(k)] = nodeVel(obsv_nds[(k)],1)
        ao[i,(k)] = nodeAccel(obsv_nds[(k)],1)

    # output to be given to controller as input
    ycf[i,:] = xo[i,:]
    yc= ycf[i-1:i+1, :]
    yc= matlab.double(yc.tolist())

    # Contoller states Fxi
    Fxi= Fx[i-1,:]
    Fxi= matlab.double(Fxi.tolist())

    # Controller time to go to lsim
    timei = [time[i]-0.02, time[i]]
    timei = matlab.double(timei)

    # Output Active control force and controller states comes from
       matlab
#    Fci,Fxi1 = eng.Stmd_hinf_controller_fnc( yc,timei, Fxi,nargout=2)
    Fci,Fxi1 = eng.Stmd_robust_controller_fnc( yc,timei, Fxi,nargout=2)

    Fc[i] = np.asarray(Fci[1])
    Fx[i,:] = np.asarray(Fxi1[1])
    Fmax=1000000
    if Fc[i]>Fmax:
```

```
            Fc[i]=Fmax
        elif Fc[i]<-Fmax:
            Fc[i]=-Fmax
        else:
            Fc[i]=Fc[i]

        #Frequency data
        FREQQ[i,:] = eigen('-fullGenLapack', 5)
        freq=np.float_power(FREQQ[i,:], 0.5)
        FREQ[i,:]= freq/2/pi

# Northridge Robust
np.savetxt('NonlinearNrt_xTMDrob.dat', xo)
np.savetxt('NonlinearNrt_FREQTMDrob.dat', FREQ)
np.savetxt('NonlinearNrt_FcATMDhinf.dat', Fc)
np.savetxt('NonlinearNrt_aTMDrob.dat', ao)
np.savetxt('NonlinearNrt_vTMDrob.dat', vo)
```

REFERENCES

Ackermann, W. (1928). Zum hilbertschen aufbau der reellen zahlen. *Mathematische Annalen 99*(1), 118–133.

Ahmadi, G. (1995). Overview of base isolation, passive and active vibration control strategies for aseismic design of structures. *Scientia Iranica 2*(2), 99–116.

Ali, S. F. and A. Ramaswamy (2009, apr). Hybrid structural control using magnetorheological dampers for base isolated structures. *Smart Materials and Structures 18*(5), 055011.

Almazán, J. L., J. C. De La Llera, and J. A. Inaudi (1998). Modelling aspects of structures isolated with the frictional pendulum system. *Earthquake engineering & structural dynamics 27*(8), 845–867.

Boyd, S., L. E. Ghaoui, E. Feron, and V. Balakrishnan (1994). Linear matrix inequalities in system and control theory.

Calafiore, G., F. Dabbene, and R. Tempo (2013). Randomized algorithms in robust control. pp. 41–57.

Christenson, R. E. (2001). *Semiactive Control Of Civil Structures For Natural Hazard Mitigation: Analytical And Experimental Studies*. Ph. D. thesis, University of Notre Dame.

Connor, J. J. (2003). *Structural Motion Control*. Pearson Education, Inc.

Deshpande, A. S. (2017). Bridging a gap in applied kalman filtering: Estimating outputs when measurements are correlated with the process noise [focus on education]. *IEEE Control Systems Magazine 37*(3), 87–93.

Doyle, J., K. Glover, P. Khargonekar, and B. Francis (1989). State-space solutions to standard h/sub 2/ and h/sub infinity / control problems. *IEEE Transactions on Automatic Control 34*(8), 831–847.

Dyke, S., B. Spencer Jr, P. Quast, M. Sain, D. Kaspari Jr, and T. Soong (1996). Acceleration feedback control of mdof structures. *Journal of Engineering Mechanics 122*(9), 907–918.

Dyke, S. J., J. M. Caicedo, G. Turan, L. A. Bergman, and S. Hague (2003). Phase i benchmark control problem for seismic response of cable-stayed bridges. *Journal of Structural Engineering 129*(7), 857–872.

Elias, S. and V. Matsagar (2015). Optimum tuned mass damper for wind and earthquake response control of high-rise building.

Elias, S., V. Matsagar, and T. Datta (2016). Effectiveness of distributed tuned mass dampers for multi-mode control of chimney under earthquakes. *Engineering Structures 124*, 1 – 16.

Elias, S., V. Matsagar, and T. Datta (2017). Distributed tuned mass dampers for multi-mode control of benchmark building under seismic excitations. *Journal of Earthquake Engineering 23*, 1–36.

Feng, M. Q. and A. Mita (1995). Vibration control of tall buildings using mega subconfiguration. *Journal of engineering mechanics 121*(10), 1082–1088.

Franklin, G. F., J. D. Powell, M. L. Workman, et al. (1998). *Digital control of dynamic systems*, Volume 3. Addison-wesley Reading, MA.

Gill, D., S. Elias, A. Steinbrecher, C. Schröder, and V. Matsagar (2017). Robustness of multi-mode control using tuned mass dampers for seismically excited structures. *Bulletin of Earthquake Engineering 15*(12), 5579–5603.

Glover, K. and J. C. Doyle (1988, sep). State-space formulae for all stabilizing controllers that satisfy an h∞-norm bound and relations to relations to risk sensitivity. *Systems & Control Letters 11*(3), 167–172.

Gu, D., P. Petkov, and M. Konstantinov (2005). Robust control design with matlab, ser. advanced textbooks in control and signal processing.

Gu, M. and Y. Quan (2004). Across-wind loads of typical tall buildings. *Journal of Wind*

Engineering and Industrial Aerodynamics 92(13), 1147–1165.

Helmerson, A. (2017, dec). *Multivariable analytic interpolation with complexity constraints: A modified Riccati approach*, Volume Chapter 9. IEEE.

Huo, L., C. Qu, and H. Li (2016). Robust control of civil structures with parametric uncertainties through d-k iteration. *The Structural Design of Tall and Special Buildings 25*(3), 158–176.

Jansen, L. M. and S. J. Dyke (2000). Semiactive control strategies for mr dampers: comparative study. *Journal of engineering mechanics 126*(8), 795–803.

Jolly Mark R., J. D. C. and B. C. Munoz (1996, October). A model of the behaviour of magnetorheological materials. *Smart Material Structures 5*(5), 607–614.

Kalman, R. E. (1960, mar). A new approach to linear filtering and prediction problems. *Journal of Basic Engineering 82*(1), 35–45.

Kar, I. N., T. Miyakura, and K. Seto (2000, May). Bending and torsional vibration control of a flexible plate structure using h_∞-based robust control law. *IEEE Transactions on Control Systems Technology 8*(3), 545–553.

Kareem, A. and S. Kline (1995). Performance of multiple mass dampers under random loading. *Journal of Structural Engineering 121*(2), 348–361.

Kınay, G. (2013, feb). Control of dynamics system behaviour by magnetorheological and varible orifice dampers. *PhD Thesıs 1*(2), 55–55.

Kobori, T. (1991). Active vibration control for architectural structure. *Journal of the Acoustical Society of Japan (E) 12*(6), 273–281.

Kucera, V. and J. V. Outrata (1988). Optimal control : Frank l. lewis. *Autom. 24*(1), 109–110.

Lee, C., K. Goda, and H. Hong (2008, 10). Cost-effectiveness of tuned mass dampers and base isolation. *Structure and Infrastructure Engineering 8*(2), 141–156. Name and Venue of Event: Beijing, China.

Lewis, F. L. (1986). Optimal estimation, a wiley-interscience publication.

Lin, Y. and Y. Yong (1987). Evolutionary kanai-tajimi earthquake models. *Journal of engineering mechanics 113*(8), 1119–1137.

Mackenroth, U. (2004). Robust control systems: theory and case studies. *Springer*, 429–485.

Mokha, A., M. Constantinou, A. Reinhorn, and V. A. Zayas (1991). Experimental study of friction-pendulum isolation system. *Journal of Structural Engineering 117*(4), 1201–1217.

Nagarajaiah, S. and E. Sonmez (2007). Structures with semiactive variable stiffness single/multiple tuned mass dampers. *Journal of Structural Engineering 133*(1), 67–77.

Ohtori, Y., R. Christenson, B. Spencer Jr, and S. Dyke (2004). Benchmark control problems for seismically excited nonlinear buildings. *Journal of Engineering Mechanics 130*(4), 366–385.

Ormondroyd, J. (1928). The theory of the dynamic vibration absorber. *Trans., ASME, Applied Mechanics 50*, 9–22.

Packard, A. K. (1989). What's new with mu: Structured uncertainty in multivariable control. pp. 1377–1382.

Pall, A., S. Vezina, P. Proulx, and R. Pall (1993). Friction-dampers for seismic control of canadian space agency headquarters. *Earthquake Spectra 9*(3), 547–557.

Pan, G., H. Matsuhisa, and Y. Honda (2000). Analytical model of a magnetorheological damper and its application to the vibration control. *TRANSACTIONS OF THE JAPAN SOCIETY OF MECHANICAL ENGINEERS Series C 3*(656), 1850–1855.

Ribakov, Y. and A. M. Reinhorn (2003). Design of amplified structural damping using optimal considerations. *Journal of Structural Engineering 129*(10), 1422–1427.

Roffel, A. and S. Narasimhan (2014). Extended kalman filter for modal identification of structures equipped with a pendulum tuned mass damper. *Journal of Sound and*

Vibration 333(23), 6038 – 6056.

Rubio, J. E. (1971). The theory of linear systems. Description based upon print version of record.

Saaed, T. E., G. Nikolakopoulos, J.-E. Jonasson, and H. Hedlund (2015). A state-of-the-art review of structural control systems. *Journal of Vibration and Control 21*(5), 919–937.

Sadek, F., B. Mohraz, A. W. Taylor, and R. M. Chung (1997). A method of estimating the parameters of tuned mass dampers for seismic applications. *Earthquake Engineering & Structural Dynamics 26*(6), 617–635.

Skogestad, S. and I. Postlethwaite (2007, jul). *Multivariable feedback control: analysis and design*, Volume 2. Wiley New York.

Soong, T. and A. Reinhorn (1993). An overview of active and hybrid structural control research in the us. *The structural design of tall buildings 2*(3), 193–209.

Spencer Jr, B., S. Dyke, M. Sain, and J. Carlson (1997). Phenomenological model for magnetorheological dampers. *Journal of engineering mechanics 123*(3), 230–238.

Spencer Jr, B. and S. Nagarajaiah (2003). State of the art of structural control. *Journal of structural engineering 129*(7), 845–856.

Spencer Jr, B. F., G. Yang, J. D. Carlson, and M. K. Sain (1998, oct). Smart dampers for seismic protection of structures: a full-scale study. *Smart Materials and Structures 7*(5), 417–426.

Tse, K.-T., K. C. Kwok, and Y. Tamura (2012). Performance and cost evaluation of a smart tuned mass damper for suppressing wind-induced lateral-torsional motion of tall structures. *Journal of Structural Engineering 138*(4), 514–525.

Tsopelas, P. C., P. Roussis, M. Constantinou, R. Buchanan, and A. Reinhorn (2005, mar). 3d-basis-me-mb: computer program for nonlinear dynamic analysis of seismically isolated structures. *Earthquake Engineering and Engineering Vibration 9*(1), 83–91.

Turan, G. (2014, mar). Hybrid control of a 3-d structure by using semi-active dampers. *Journal of Sound and Vibration 469*, 329–340.

Wang, D., T. K. Tse, Y. Zhou, and Q. Li (2015). Structural performance and cost analysis of wind-induced vibration control schemes for a real super-tall building. *Structure and Infrastructure Engineering 11*(8), 990–1011.

Wang, S.-G. (2003). Robust active control for uncertain structural systems with acceleration sensors. *Journal of Structural Control 10*(1), 59–76.

Wang, S.-G. (2004). Linear quadratic gaussian-alpha control with relative stability and gain parameter for the structural benchmark problems. *Journal of Engineering Mechanics 130*(4), 511–517.

Wang, Y. and S. J. Dyke (2006, oct). A comparative study of the base isolation benchmark problem using h2/lqg and smart dampers. pp. 1–16.

Welch, B. B., K. Jones, and J. Hobbs (2003). *Practical Programming in Tcl/Tk*. Prentice Hall Professional.

Yang, G., B. F. Spencer Jr, H.-J. Jung, and J. D. Carlson (2004). Dynamic modeling of large-scale magnetorheological damper systems for civil engineering applications. *Journal of Engineering Mechanics 130*(9), 1107–1114.

Yang, J., J. Wu, and A. Agrawal (1995). Sliding mode control for nonlinear and hysteretic structures. *Journal of Engineering Mechanics 121*(12), 1330–1339.

Yang, J., J. Wu, and Z. Li (1996). Control of seismic-excited buildings using active variable stiffness systems. *Engineering structures 18*(8), 589–596.

Yang, J. N., A. K. Agrawal, B. Samali, and J.-C. Wu (2004). Benchmark problem for response control of wind-excited tall buildings. *Journal of Engineering Mechanics 130*(4), 437–446.

Yang, J. N., A. Akbarpour, and P. Ghaemmaghami (1987). New optimal control algorithms for structural control. *Journal of Engineering Mechanics 113*(9), 1369–1386.

Yang, J. N., Y. Lei, S. Lin, and N. Huang (2004). Hilbert-huang based approach for structural damage detection. *Journal of engineering mechanics 130*(1), 85–95.

Yang, J. N., Y. Lei, S. Pan, and N. Huang (2003). System identification of linear structures based on hilbert–huang spectral analysis. part 1: normal modes. *Earthquake engineering & structural dynamics 32*(9), 1443–1467.

Yang Jr, G. S. and C. BF (2002). Jd and sain, mk, large-scale mr fluid damper: Modeling and dynamic structure. *Engineering Structures 24*(3), 309–323.

Yao, J. (1972). Concept of structural control. *Journal of the Structural Division 98*(st 7), 167–178.

Yoshida, O. and S. J. Dyke (2004). Seismic control of a nonlinear benchmark building using smart dampers. *Journal of engineering mechanics 130*(4), 386–392.

Yun, X. and L. Gardner (2017). Stress-strain curves for hot-rolled steels. *Journal of Constructional Steel Research 133*, 36–46.

Zayas, V. A., S. A. Low, L. Bozzo, and S. A. Mahin (1989). *Feasibility and performance studies on improving the earthquake resistance of new and existing buildings using the friction pendulum system*, Volume 6. Earthquake Engineering Research Center.

Zemp, R., J. C. de la Llera, H. Saldias, and F. Weber (2016). Development of a long-stroke mr damper for a building with tuned masses. *Smart Materials and Structures 25*(10), 105006.

Zhou, K. and J. C. Doyle (1998, jul). *Essentials of robust control*, Volume 104. Prentice hall Upper Saddle River, NJ.

Zhou, T. and H. Kimura (1994). Simultaneous identification of nominal model, parametric uncertainty and unstructured uncertainty for robust control. *Automatica 30*(3), 391–402.

Ziegler, J. G. and N. B. Nichols (1993). Optimum settings for automatic controllers. *trans. ASME 115*(11), 220–222.

Zinober, A. S. (1994). *Variable structure and Lyapunov control*, Volume 193. Springer.

Zsarnóczay, A. and J. W. Baker (2020). Using model error in response history analysis to evaluate component calibration methods. *49*, 175–193.

VITA

Vedat Şenol graduated from Ortaklar Anatolian Teacher Training High School, Aydın, Turkey, in 2009, he entered Ege University.

He received his B.Sc. degree in Civil Engineering and double major in Mechanical Engineering at Ege University, Turkey, in 2014 and 2015, respectively. In 2016, he started his direct Ph.D. education in Structural Control at Izmir Institute of Technology with a bachelor's degree. He started working as a research and teaching assistant in 2016. During his employment, he assisted the courses of Fluid Dynamics, Engineering Mechanics, Steel Structures, Reinforced-Concrete Structures, Advanced Numerical Methods in Engineering, Hydraulic in the Department of Civil Engineering at IZTECH.

He received the degree of Doctor of Philosophy of Civil Engineering in October 2021. He studies the topic of nonlinear robust control theory and applications. His current affiliation is at Wolfram MathCore AB as an applications engineer.